

AD-A100 399

DAYTON UNIV OHIO DEPT OF PHYSICS  
CHARACTERIZATION OF III-V SEMICONDUCTORS.(U)  
APR 81 D C LOOK, M M KREITMAN, P WON YU

F/G 20/12

F33615-76-C-1207

UNCLASSIFIED

AFWL-TR-81-1036

NL

1 of 2  
AD A  
10-0399



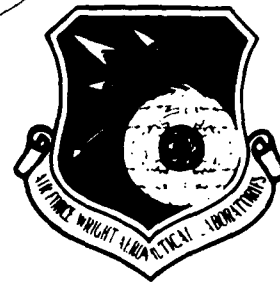
6/8/81

AFWAL-TR-81-1036

LEVEL

2

CHARACTERIZATION OF III-V SEMICONDUCTORS



UNIVERSITY OF DAYTON  
PHYSICS DEPARTMENT  
300 COLLEGE PARK  
DAYTON, OHIO 45469

AD A100399

APRIL 1981

TECHNICAL REPORT AFWAL-TR-81-1036  
FINAL REPORT FOR PERIOD: June 1976 - November 1980

APPROVED FOR PUBLIC RELEASE; DISTRIBUTION UNLIMITED

AVIONICS LABORATORY  
AIR FORCE WRIGHT AERONAUTICAL LABORATORIES  
AIR FORCE SYSTEMS COMMAND  
WRIGHT-PATTERSON AIR FORCE BASE, OHIO 45433

DTIC  
UNCLASSIFIED

JUN 19 1981

DTIC FILE COPY


81 6 19 041

NOTICE

When Government drawings, specifications, or other data are used for any purpose other than in connection with a definitely related Government procurement operation, the United States Government thereby incurs no responsibility nor any obligation whatsoever; and the fact that the government may have formulated, furnished, or in any way supplied the said drawings, specifications, or other data, is not to be regarded by implication or otherwise as in any manner licensing the holder or any other person or corporation, or conveying any rights or permission to manufacture use, or sell any patented invention that may in any way be related thereto.

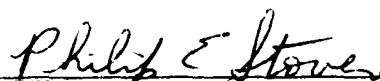
This report has been reviewed by the Office of Public Affairs (ASD/PA) and is releasable to the National Technical Information Service (NTIS). At NTIS, it will be available to the general public, including foreign nations.

This technical report has been reviewed and is approved for publication.



DAVID L. KINGSTON  
Program Manager  
Electronic Research Branch

FOR THE COMMANDER



PHILIP E. STOVER, Chief  
Electronic Research Branch  
Avionics Laboratory

If your address has changed, if you wish to be removed from our mailing list, or if the addressee is no longer employed by your organization please notify AFWAL/AADR W-PAFB, OH 45433 to help us maintain a current mailing list.

Copies of this report should not be returned unless return is required by security considerations, contractual obligations, or notice on a specific document.

14. REPORT DOCUMENTATION PAGE		READ INSTRUCTIONS BEFORE COMPLETING FORM																
1. REPORT NUMBER AFWAL-TR-81-1036	2. GOVT ACCESSION NO. AD-A200399	3. RECIPIENT'S CATALOG NUMBER																
4. TITLE (and Subtitle) CHARACTERIZATION OF III-V SEMICONDUCTORS.		5. TYPE OF REPORT & PERIOD COVERED Final Report. June 1976 - November 1980																
7. AUTHOR(s) David C./Look, Marshall M./Kreitman, Phil Won Yu, Sang Boo Nam, John W./Farmer, Dennis C. Walters		6. PERFORMING ORG. REPORT NUMBER																
9. PERFORMING ORGANIZATION NAME AND ADDRESS Physics Department University of Dayton 300 College Park Dayton, Ohio 45469		8. CONTRACT OR GRANT NUMBER(s) F33615-76-C-1207																
11. CONTROLLING OFFICE NAME AND ADDRESS Avionics Laboratory (AFWAL/AADR) Air Force Wright Aeronautical Laboratories Wright-Patterson AFB, OH 45433		10. PROGRAM ELEMENT, PROJECT, TASK AREA & WORK UNIT NUMBERS 61102F 2306R161																
14. MONITORING AGENCY NAME & ADDRESS (if different from Controlling Office)		12. REPORT DATE April 1981																
		13. NUMBER OF PAGES 116																
		15. SECURITY CLASS. (of this report) Unclassified																
		15a. DECLASSIFICATION/DOWNGRADING SCHEDULE																
16. DISTRIBUTION STATEMENT (of this Report)  Approved for public release; distribution unlimited.																		
17. DISTRIBUTION STATEMENT (of the abstract entered in Block 20, if different from Report)																		
18. SUPPLEMENTARY NOTES																		
19. KEY WORDS (Continue on reverse side if necessary and identify by block number) <table border="0"> <tr> <td>III-V Compounds</td> <td>Electron Irradiation</td> <td>Photo-Hall</td> </tr> <tr> <td>Semi-insulating</td> <td>Native Defects</td> <td>Photomagnetolectric</td> </tr> <tr> <td>GaAs</td> <td>Type Conversion</td> <td>Photoluminescence</td> </tr> <tr> <td>InP</td> <td>Hall Effect</td> <td>Mass Spectroscopy</td> </tr> <tr> <td>Ion Implantation</td> <td>Photoconductivity</td> <td>Donor-Acceptor</td> </tr> </table>				III-V Compounds	Electron Irradiation	Photo-Hall	Semi-insulating	Native Defects	Photomagnetolectric	GaAs	Type Conversion	Photoluminescence	InP	Hall Effect	Mass Spectroscopy	Ion Implantation	Photoconductivity	Donor-Acceptor
III-V Compounds	Electron Irradiation	Photo-Hall																
Semi-insulating	Native Defects	Photomagnetolectric																
GaAs	Type Conversion	Photoluminescence																
InP	Hall Effect	Mass Spectroscopy																
Ion Implantation	Photoconductivity	Donor-Acceptor																
20. ABSTRACT (Continue on reverse side if necessary and identify by block number) <p>Impurities and defects in semiconducting and semi-insulating GaAs and InP have been investigated by electrical, optical, and mass spectroscopic techniques.</p>																		

## FOREWORD

The work described in this report covers the period 1 June 1976 - 30 November 1980 and approximately 22 man-years of effort, mainly directed toward the establishment of viable characterization techniques for III-V semiconducting compounds, especially GaAs. We have both developed new techniques and revitalized old ones, attempting to judge the merits of each during the course of analyzing many hundreds of samples. Not all of our goals were accomplished but we feel that a positive contribution was made toward the solution of some of the problems plaguing GaAs device development. The professional personnel who worked full-time during at least a part of the contract include: Dr. David C. Look, Mr. Marshall M. Kreitman, Dr. Phil Won Yu, Dr. Sang Boo Nam, Dr. John W. Farmer and Mr. Dennis C. Walters. In addition, Dr. James R. Schneider capably served as Contract Supervisor, Mrs. Jeannette Cancila efficiently typed our manuscripts and reports, and several student assistants contributed technical skills which greatly increased the work output.

We also wish to thank our many colleagues at the Air Force Avionics Laboratory who provided the good working conditions and relationships so vital to a productive effort. Special appreciation goes to Maj. Robert J. Almasy and Mr. David L. Kingston who each monitored our contract at different times. Without their help, and that of many others, our task would have been nearly impossible.

This work was performed by the University of Dayton Physics Department, 300 College Park, Dayton, Ohio, 45469, under Contract F33615-76-C-1207. The project, task, and work unit number was 2306R101, and the project engineer was David L. Kingston, AFWAL/AADR, Wright-Patterson AFB, Ohio, 45433. The report was submitted on 2 January 1980.

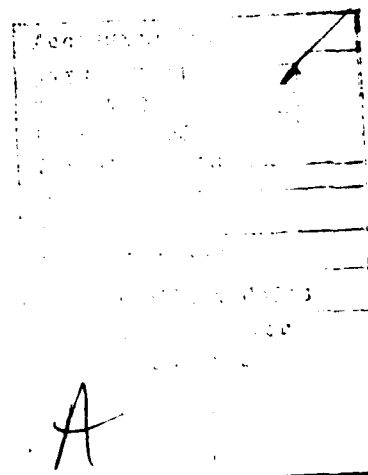


# TABLE OF CONTENTS

	Page
1.0 SUMMARY OF WORK . . . . .	1
1.1 Introduction . . . . .	1
1.2 Semi-insulating GaAs . . . . .	1
1.3 GaAs Buffer Layers . . . . .	3
1.4 Native Defects in GaAs . . . . .	4
1.5 Impurities in GaAs . . . . .	4
1.6 InP . . . . .	5
2.0 ELECTRICAL AND PHOTOELECTRONIC PROPERTIES OF SEMI-INSULATING GaAs . .	6
2.1 Introduction . . . . .	6
2.2 Apparatus Improvements . . . . .	6
2.3 A Comparison of Mass Spectrographic and Electrical Data. . . . .	7
2.4 The Interpretation of Photoconductivity and Photo-Hall Data. . .	13
2.5 The Impurity Photomagnetolectric Effect . . . . .	19
2.6 Infrared Spectral Detectivity of GaAs:Cr . . . . .	20
2.7 Energy Levels. . . . .	21
3.0 ELECTRICAL MESUREMENTS IN SEMICONDUCTING GaAs . . . . .	26
3.1 Introduction . . . . .	26
3.2 Donor and Acceptor Concentrations. . . . .	26
3.3 Energy Levels. . . . .	27
4.0 ELECTRICAL AND PHOTOELECTRONIC PROPERTIES OF SEMI-INSULATING InP. . .	33
4.1 Introduction . . . . .	33
4.2 Resonance Photoconductivity. . . . .	34
5.0 PHOTOLUMINESCENCE IN HEAT-TREATED GaAs . . . . .	37
5.1 Introduction . . . . .	37
5.2 Mn-Implanted GaAs. . . . .	37
5.3 Discussion of Mn-Related Emissions . . . . .	41
5.4 Conclusions. . . . .	42
6.0 ION IMPLANTED LAYERS IN GaAs. . . . .	43
6.1 Introduction . . . . .	43
6.2 Excitation-Dependent Emission in Mg-, Be-, Cd-, and Zn-Implanted GaAs. . . . .	43
6.3 Experimental Results . . . . .	44
6.4 Model. . . . .	44
6.5 Deep Emission Centers in Ge-Implanted GaAs . . . . .	50
7.0 EMISSION CHARACTERISTICS OF SEMI-INSULATING GaAs. . . . .	53
7.1 Introduction . . . . .	53
7.2 Results. . . . .	54
7.3 Conclusions. . . . .	58

# TABLE OF CONTENTS

	Page
8.0 PHOTOLUMINESCENCE CHARACTERIZATION OF BULK InP CRYSTALS . . . . .	59
8.1 Introduction . . . . .	59
8.2 Results and Analysis . . . . .	59
8.3 Conclusions. . . . .	<b>67</b>
9.0 DEFECT STUDIES IN GaAs. . . . .	68
9.1 Introduction . . . . .	68
9.2 Defects in n-type GaAs . . . . .	68
9.3 Type Conversion in Electron-Irradiated GaAs. . . . .	69
9.4 Defect Studies in Multilayer Epitaxial GaAs by Transient Capacitance . . . . .	71
9.5 Persistent Photoconductivity in GaAs: Relationship to Low-Temperature Solar Cell I-V Characteristiss . .	72
10.0 FAR INFRARED STUDIES IN GaAs. . . . .	76
11.0 SPARK-SOURCE MASS SPECTROSCOPY IN GaAs. . . . .	79
11.1 Background . . . . .	79
11.2 Analytical Program . . . . .	79
11.3 Summary. . . . .	80
12.0 OPTICAL SCHEME FOR DETERMINATION OF CONCENTRATIONS OF DONORS AND ACCEPTORS IN A SEMICONDUCTOR. . . . .	87
12.1 Introduction . . . . .	87
12.2 Theory . . . . .	88
12.3 Determination of $N_D$ and $N_A$ . . . . .	91
12.4 Life Times and Mobilities of Electrons and Holes . . . . .	95
12.5 Determination of Effective Temperatures of Electrons and Holes . . . . .	95
12.6 Remarks . . . . .	96
13.0 ENERGIES OF LINES DUE TO DONOR-ACCEPTOR TYPE COMPLEXES IN GaAs. . . . .	100
REFERENCES . . . . .	105
PUBLICATIONS. . . . .	109

# LIST OF TABLES

<u>Table</u>		<u>Page</u>
2-1	Energy levels in semi-insulating GaAs . . . . .	23
3-1	Ionization energies of p-type GaAs epitaxial layers . . . . .	28
3-2	Electrical properties of several, bulk, n-type GaAs samples. . . . .	30
5-1	Electrical and photoluminescence properties of Mn-doped GaAs . . . . .	39
6-1	Moving emissions in Mn-implanted GaAs . . . . .	46
6-2	Emission bands in Ge-implanted GaAs . . . . .	52
8-1	Electrical and photoluminescence properties of Fe-doped InP . . . . .	61
11-1	Comparison of several trace analytical techniques for GaAs. . . . .	81
11-2	Spark-source mass spectrographic analysis of GaAs . . . . .	83
13-1	Energies of lines calculated using a model of the double acceptor-single donor type complex. . . . .	101
13-2	Energies of lines calculated using a model of the double donor-single acceptor type complex. . . . .	102



# LIST OF FIGURES

<u>Figure</u>		<u>Page</u>
2-1	Block diagram of the automated Hall-effect apparatus . . . . .	8
2-2	Block diagram of the automated monochromator . . . . .	9
2-3	Circuit diagram of the grating-drive unit. . . . .	10
2-4	Ionized impurity concentration vs. electron mobility in Cr-doped GaAs. . . . .	12
2-5	True electron mobility vs. apparent electron mobility in semi-insulating GaAs . . . . .	14
2-6	Photoconductivity spectra in GaAs:Cr . . . . .	15
2-7	Photo-Hall data in GaAs:Cr . . . . .	16
2-8	Photoconductivity and photo-Hall data in GaAs:O. . . . .	18
2-9	Spectral detectivity of GaAs:Cr. . . . .	22
4-1	Photoconductivity spectrum of InP:Fe . . . . .	35
4-2	Proposed room-temperature energy diagram of $\text{Fe}^{2+}$ in InP. . . . .	36
5-1	Emission spectra in Mn-implanted GaAs. . . . .	40
6-1	Excitation intensity vs emission-peak energy in Mg-implanted GaAs . . . . .	45
6-2	Donor-acceptor pair emission in compensated GaAs . . . . .	48
6-3	Emission spectra in Ge-implanted, $\text{Si}_3\text{N}_4$ -capped GaAs. . . . .	51
7-1	Photoluminescence spectra of Cr- and O-doped semi-insulating GaAs at 4.2 <sup>0</sup> K. . . . .	55
7-2	Temperature dependence of Cr-emission intensity relative to O-emission intensity in GaAs:Cr. . . . .	57
8-1	The 1.10 eV emission band in InP . . . . .	60
8-2	Emission transitions expected from configuration-coordinate diagram . . . . .	63
8-3	AC photoconductivity spectra for various temperatures in InP:Fe. . . . .	64
8-4	DC photoconductivity spectra for various temperatures in InP:Fe . . . . .	65

# LIST OF FIGURES

<u>Figure</u>		<u>Page</u>
9-1	Isothermal anneal of VPE GaAs at 200°C after 1 MeV electron irradiation . . . . .	70
9-2	Change in sheet carrier concentration vs. photo fluence for GaAs structure . . . . .	73
9-3	Current vs. forward-bias voltage at 77°K for GaAs solar cell. . . . .	75
10-1	Transmission spectra as a function of annealing temperature in C-implanted GaAs . . . . .	78
11-1	Cryo-probe assembly for MS-702 mass spectrometer. . . . .	82
11-2	Source pressure vs. time for different methods of source pumping . . . . .	84
11-3	Oxygen and carbon background concentrations vs. sparking time for LN <sub>2</sub> and LHe cryo-pumping. . . . .	85
12-1	Effective temperatures and quasi-Fermi energies for electrons and holes in GaAs as functions of excitation intensity. . . . .	97
12-2	Neutral donor and acceptor concentrations in GaAs as functions of excitation intensity. . . . .	98

## 1.0 SUMMARY OF WORK

### 1.1 Introduction

In this section we will summarize some of the more important accomplishments of our work effort. More detailed discussions will appear in the following sections.

### 1.2 Semi-insulating GaAs

The doping of GaAs with Cr and/or O produces very high resistivity ( $10^8 - 10^9 \Omega\text{-cm}$ ) material<sup>1</sup> which is extensively used to provide substrates for GaAs field effect transistors (FET), integrated circuits, and optoelectronic devices. However, thin-layer devices, such as high frequency FET's, can be strongly influenced by the interface region between the substrate and active layer.<sup>2</sup> Therefore, substrate quality becomes important. Nearly everyone agrees, and indeed it has been experimentally shown, that substrate quality is one of the most important factors in the performance, reliability, and yield of GaAs FET's.<sup>3</sup> For this reason, we have devoted a large share of our manpower and equipment resources toward the solution of this problem.

In the area of electrical measurements, we have designed and constructed an automated high-resistivity Hall-effect and photoelectronic apparatus which has state-of-the-art capabilities. Temperature can be automatically varied between 4.2 and 800<sup>0</sup> K; magnetic field, 0-19 kG; monochromatic light irradiation, 0.6-3.4  $\mu\text{m}$ ; and light intensity,  $0 - 3 \times 10^{15}$  photons/cm<sup>2</sup>sec over most of this wavelength range. The mixed-conductivity nature of semi-insulating GaAs can be taken into account automatically by use of a somewhat complex magnetic-field sequencing scheme.<sup>4</sup> With this apparatus we have extensively studied GaAs:Cr and GaAs:O by the dark Hall, photo-Hall, photoconductivity, and photomagnetoelectric (PME) methods.<sup>5</sup> We have investigated the PME effect in the impurity (below band gap) regime for the first time and extended the PME theory to this regime.<sup>6</sup>

We have also determined the usefulness of each of these techniques for "fingerprinting" the substrate materials.<sup>5</sup> Certain of the measured parameters were found to correlate, although weakly, with the "conversion propensity," i.e., the tendency of the sample to form a thin, conducting layer during high-temperature processing. Furthermore, a correlation was found between the Cr concentration, as measured by spark-source mass spectroscopy (SSMS), and the Hall mobility.<sup>7</sup> However, we found that, unfortunately, commercially available SSMS results are unreliable in the 1 ppmA and below region especially for C and O, two of the most important impurities in GaAs. Recently we have solved this problem and discuss it in more detail below.

In the area of photoluminescence (PL) also we have established a state-of-the-art apparatus using a krypton laser and a cooled PbS detector. This system has a variable temperature capability (4.2 - 400°K) which often makes possible a much greater understanding of the particular center being studied. The important Cr and O lines in GaAs have been studied in detail,<sup>8</sup> and the 1.40 eV line in Mn-doped GaAs has been explained.<sup>9</sup> Another important finding is that Cr from a GaAs:Cr substrate can diffuse great distances at vapor phase epitaxy (VPE) growth temperatures, even appearing on the surface of a 100  $\mu$ m epilayer. This phenomenon has important consequences in the growth of high-purity buffer layers.

The far-infrared absorption effort has also contributed much to the substrate characterization program. This apparatus uses large optics (7 inch x 9 inch gratings) to increase light intensity but also has good resolution (200  $\text{\AA}$  per mm slit width at 30  $\mu$ m).<sup>10</sup> During the present contract period, substantial improvements have been made to the vacuum and cryogenic sections of the spectrometer. Although Cr and O electronic absorptions have been seen and analyzed in a number of samples, the major emphasis has been on observing localized-vibrational mode (LVM) absorptions for use as a trace-analysis technique.

Highlights of this program include the observation of Si at the  $1 \times 10^{16} \text{ cm}^{-3}$  level in bulk material<sup>11</sup> and C in an ion-implanted sample.<sup>12</sup>

### 1.3 GaAs Buffer Layers

One proposal to solve the substrate-active-layer interface problem involves growing a high-purity "buffer" layer between the two layers.<sup>2</sup> This solution raises costs, of course, but may be necessary for adequate performance, reliability, and yield of the resulting devices. We have measured VPE layers grown at the DHR Branch of the Air Force Avionics Laboratory (AFAL) with resistivities greater than  $10^5 \Omega\text{-cm}$ , qualifying them as "semi-insulating" substrates for many applications. It has been found that the epilayers of such resistivity are always controlled by a level  $0.50 \pm 0.02 \text{ eV}$  above the valence band.<sup>13</sup> Since Cr is often found in these epilayers, it is tempting to suggest that this center is Cr related. It could also, of course, be associated with a native defect, or both. In fact, this same level is seen in samples converted from n-type to p-type by irradiation<sup>14</sup> which supports the native-defect theory. The whole subject of native defects is extremely important and will be addressed below in a separate paragraph.

One of the highlights of the GaAs epilayer research has been the development of a PL technique to determine "electrical" parameters, namely  $N_D$  and  $N_A$ , in GaAs. One of our contract personnel developed the theoretical scheme for implementing the method,<sup>15</sup> and then DHR personnel carried out the experiment, which agreed well with the theory. Finally, another of our contract personnel checked the validity of the method by performing extensive PL measurements on many samples.<sup>16</sup> One of the beauties of this technique is its nondestructive nature, whereas Hall-effect measurements require contacts, which may be difficult to remove.

#### 1.4 Native Defects in GaAs

The DHR Branch of AFAL has a 1 MeV Van de Graaff accelerator which is very useful for creating point defects. Such simple defects, Ga and As vacancies and interstitials, must be understood before the more complex defects produced during growth, annealing, or ion implantation can be dealt with. Thus, we have devoted a major effort to this end and some of the results include the identification levels at 0.1, 0.2, and 0.3 eV below the conduction band<sup>17</sup> and at 0.1 and 0.5 eV above the valance band.<sup>14</sup> Some of these levels correspond to those seen by deep level transient spectroscopy (DLTS).<sup>18</sup> Furthermore, we have created, for the first time, good p-type GaAs from good n-type VPE layers.<sup>14</sup> This process has technological possibilities and the results should be studied further. Also the ability to vary the Fermi level from near the conduction band to near the valence band, by electron irradiation, makes it possible, for the first time, to study levels throughout the whole band gap in the same sample.

#### 1.5 Impurities in GaAs

Although impurities in connection with GaAs substrate and epilayer research have already been discussed, we feel that this subject deserves special mention because of the vast importance of impurities in nearly every phase of semiconductor device operation. Semiconductor researchers must be able to obtain accurate impurity analyses of elements like Cr, O, Si, C, Cu, Fe, and Mn in the 1 ppmA and below region. In our work effort we have attacked this problem in the following ways: (a) commercially available SSMS (in the United States); (b) our own SSMS; (c) localized-vibrational-mode absorption; (d) PL; (e) temperature-dependent Hall-effect measurements; and (f) photoconductivity (PC). Although the Hall-effect measurements can in certain cases give quite accurate quantitative results, nevertheless, the only well-established broadly applicable quantitative technique is SSMS. Accordingly early in the program

we had about 50 samples analyzed at a cost of about \$8,000. The results were unsatisfactory, especially with respect to C and O analyses. We then worked with a group at Wright State University to establish a spark-source spectrometer with liquid-helium cryopumping in the source region. The system has worked well and we have reduced C and O background levels to less than 0.1 ppmA for GaAs analyses. To our knowledge no other facility in the country has this capability.

The other techniques mentioned above have at this state been established as good qualitative trace-analysis techniques for many important impurity elements. Several of the shallow acceptors, such as C, Cd, Zn, Mg, Si, and Be, for example, can be distinguished in PL.<sup>19,20</sup> Likewise many of the deep impurities such as Cr and Fe<sup>21</sup> can be studied. The LVM technique has been used to identify trace amounts of Si, C, and Al in our laboratory, and other elements have been identified in other laboratories. One added virtue of this technique is its ability to distinguish the lattice site of many of the impurity elements. Hall-effect and photoconductivity measurements have also been used to study and identify deep impurities, especially Cr and O. All of the techniques mentioned above could be made more quantitative if standards were established.

#### 1.6 InP

Although GaAs is certainly by far the most important III-V compound in terms of presently available devices, others such as InP and GaP also have wide-band-gap applications. In fact, in the last two years or so, the Department of Defense has funded a rather large amount of InP research in connection with high-frequency FET applications.<sup>22</sup> We have characterized some of these samples, especially by Hall-effect,<sup>23</sup> PL,<sup>24,25</sup> and PC<sup>26</sup> measurements. A new PC peak, never seen before, was found in the important substrate material, InP:Fe, and attributed to an intracenter Fe transition,<sup>26</sup> in agreement with recent absorption measurements.<sup>27</sup> A reasonable Fe concentration was calculated for the sample.

## 2.0 ELECTRICAL AND PHOTOELECTRONIC PROPERTIES OF SEMI-INSULATING GaAs

### 2.1. Introduction

Electrical measurements are obviously a very important part of any semiconductor materials characterization program.<sup>28</sup> Further information can often be gained by measuring the electrical properties in the presence of monochromatic light, giving the photoconductivity (PC), photo-Hall (PH), and photomagnetoelectric (PME) effects. Much of our work in these areas has been published so that in some sections of this report we will simply reprint the abstract of a particular publication, with, perhaps, an illustrative drawing or table. An interested reader will then have enough information to decide whether or not to pursue the matter by obtaining a full copy of the publication. Reprints are available from the authors.

### 2.2. Apparatus Improvements

During the 4½-year period of this contract we have measured the electrical properties of more than 600 GaAs and InP samples. The minimum characterization carried out on each sample was a room-temperature Hall-effect and resistivity measurement, giving resistivity, carrier concentration, and mobility. However, for many samples we measured these properties as functions of temperature, magnetic field strength, and monochromatic light irradiation. To accomplish all this with only one professional employee and no technicians, it was necessary to automate the Hall-effect and photoelectronic apparatus.

The following abstract is reprinted from Ref. 29.

We have assembled a computer-controlled system capable of measuring a wide range of semiconductor resistivities and Hall coefficients, as well as their dependences upon temperature (4.2 - 600°K), magnetic field (0 - 18 kG), and monochromatic light irradiation (up to  $2 \times 10^{14}$  photons/cm<sup>2</sup>sec, held constant over the range 0.76 - 2.50  $\mu$ m). With the use of a guarded cable configuration, the response time for a  $10^{13} \Omega$  sample is less than 10 sec.



The system uses commercial components whenever possible and is built around a PDP 11-03 computer with a standard IEEE-488 I/O bus. The only important non-commercial piece of apparatus presented here is a wavelength-scan and intensity-control system for a popular,  $\frac{1}{4}$ -m, high-intensity monochromator.

In Fig. 2-1 we show a block diagram of the scheme for automatically controlling and measuring current and voltage. The block diagrams illustrating temperature and magnetic field control can be found in Ref. 29.

To further describe the automatic light control we reprint an abstract from Ref. 30.

A wavelength-scan and intensity control system for a widely-used, high-intensity monochromator is described. The wavelength scan is bidirectional and variable speed, and may be controlled manually or by TTL logic from a computer. The intensity control is effected by use of a programmable dc power supply and D-A converter. Various filters are described which allow an intensity of up to  $2 \times 10^{14}$  photons/cm<sup>2</sup> s to be achieved in a 1 cm x 3 cm area over a wavelength range 0.76-2.50  $\mu$ m, at 0.07  $\mu$ m bandwidth, with a single grating. (A lesser intensity is available to 3.4  $\mu$ m.) This wide range is made possible by the use of second-order light from 0.76-1.00  $\mu$ m. Photoconductivity data in GaAs:Cr and InP:Fe are presented, as an example.

The block diagram describing the external control system for the B&L High-Intensity monochromator is shown in Fig. 2-2. The stepping-motor circuitry is illustrated in Fig. 2-3. A list of equipment suppliers can be found in References 29 and 30.

### 2.3. A Comparison of Mass Spectrographic and Electrical Data

During the early phases of this contract we decided to test the relationship between carrier mobility and ionized impurity concentration in order to see if the former could be used as a measure of the latter. The impurity concentrations were obtained from commercial SSMS data.



## MONOCHROMATIC-LIGHT CONTROL

### MONOCHROMATOR WITH GRATING DRIVE

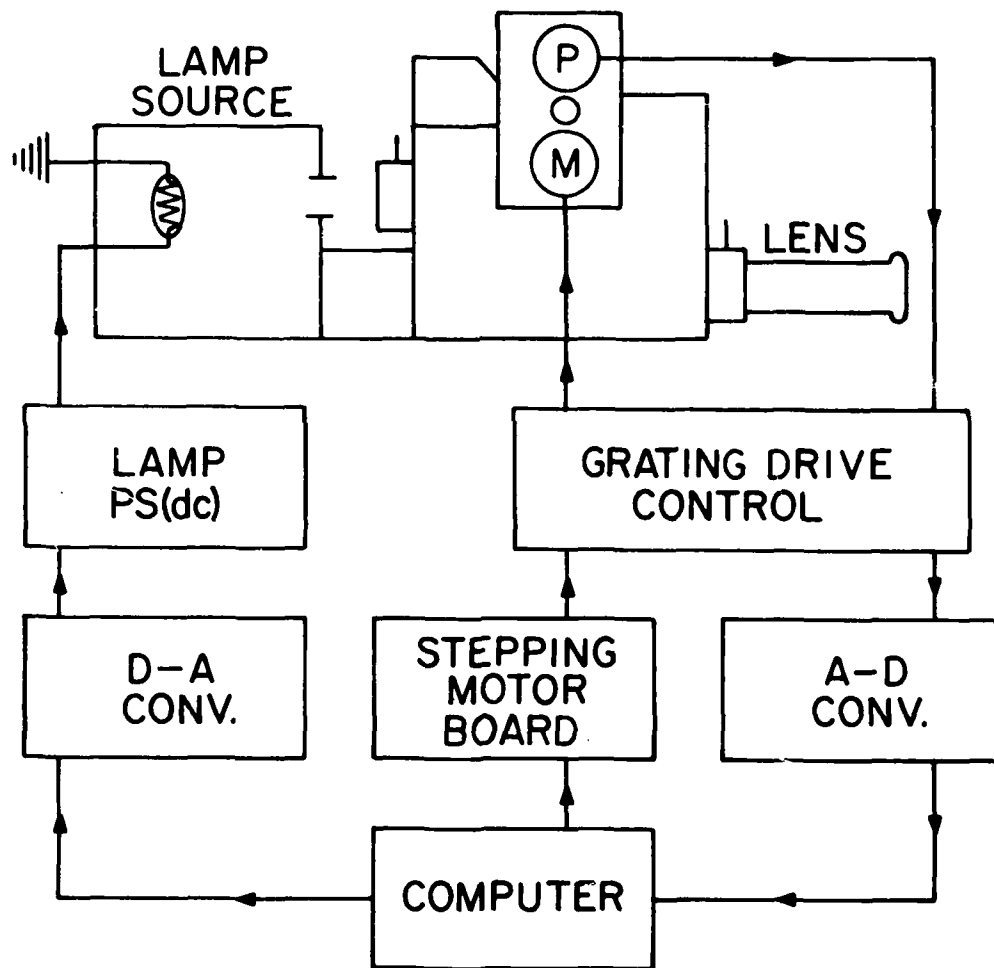


Fig. 2-2. The automatic wavelength-scan and intensity-control apparatus. Here, P  $\equiv$  potentiometer, and M  $\equiv$  motor.

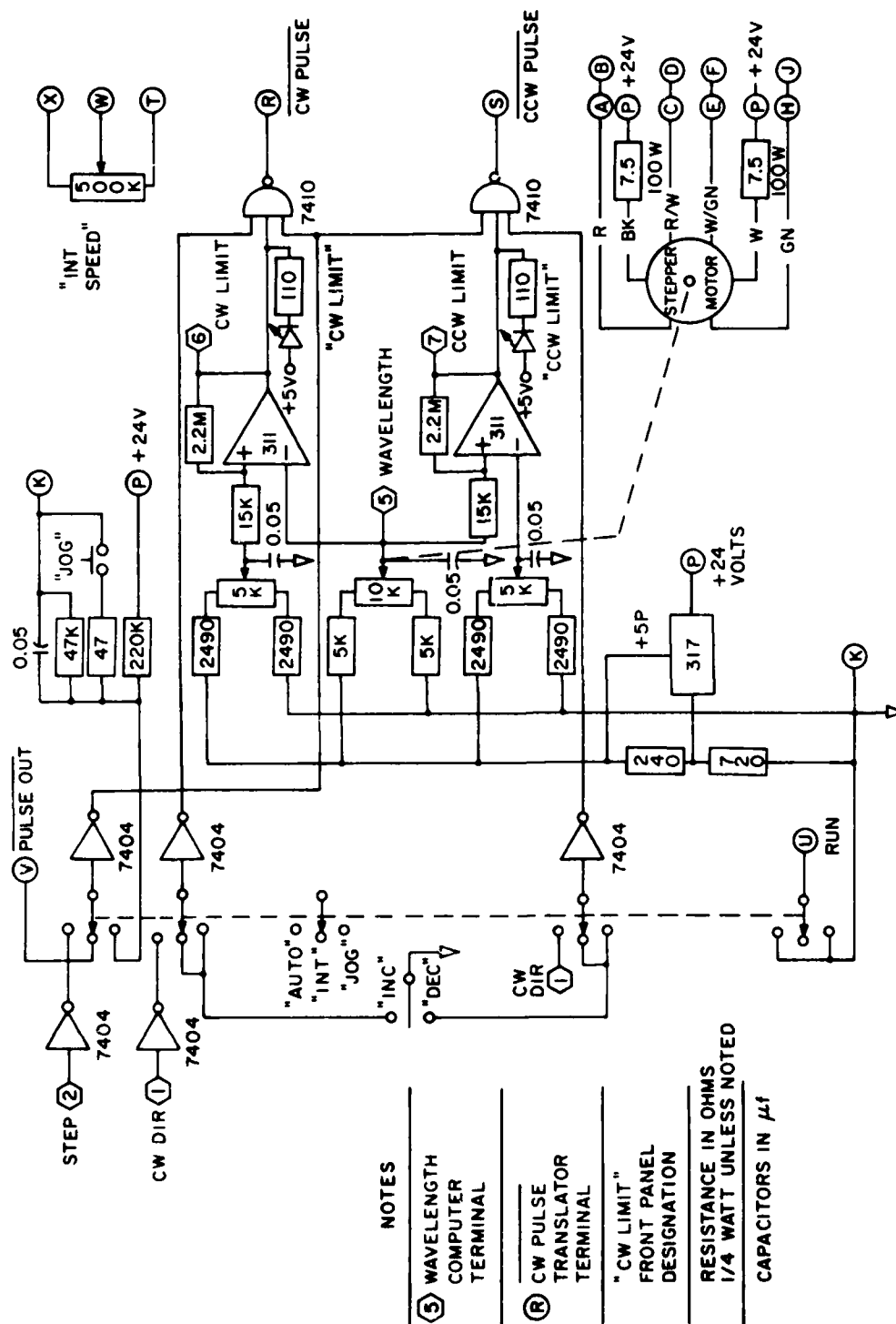


Fig. 2-3. A circuit diagram of the Grating-Drive Control Unit (cf. Fig. 2-2). The circled letters are terminal designations on a Slo-syn STM101 Translator Module. The hexagonally-enclosed numbers are remote connections, as follows: No. 1: from computer-controlled source of TTL stepping pulses; No. 2: from computer-controlled source of TTL "Hi" or "Lo" voltages, corresponding to cw or ccw motor directions, respectively; No. 5: to A-D converter, and then to computer.

The following abstract is reprinted from Ref. 7.

The room-temperature electrical properties of 28 semi-insulating GaAs crystals have been determined by using a mixed-conductivity analysis. It is shown that for most of these samples, such an analysis gives good accuracy for the electron mobility  $\mu_n$  and electron concentration  $n$ , but poorer accuracy for the hole mobility  $\mu_p$ , hole concentration  $p$ , and intrinsic concentration  $n_i$ . The intrinsic concentration is determined at 296°K to be  $n_i \approx (1.7 \pm 0.4) \times 10^6 \text{ cm}^{-3}$ , which compares favorably with the theoretical value deduced from the band gap and the effective masses. From a Fermi-level analysis, the dominant Cr acceptor is found to lie at  $0.69 \pm 0.92 \text{ eV}$  from the valence band. For many of the samples, the ionized-impurity concentrations  $N_I$  have been estimated from spark-source mass-spectrographic measurements and are compared with the concentrations predicted from  $\mu_n$ . In general, the expected inverse relationship between  $\mu_n$  and  $N_I$  is found to hold, but the scatter in the data is quite large, mainly due to the uncertainties in the mass-spectrographic results.

The results are shown in Fig. 2-4. Although there appears to be some correlation between the data and theory there are problems with the experimental values of both  $N_I$  and  $\mu_n$ . The problem with  $N_I$  results from unreliable SSMS data, and our steps to correct this situation are outlined in Sec. 11. The problem with  $\mu_n$  is discussed in the abstract below, reprinted from Ref. 31.

It is well known that an analysis of the magnetic-field dependences of the resistivity  $\rho$  and Hall coefficient  $R$ , in nearly intrinsic material, will uniquely yield  $\mu_n$ ,  $\mu_p$ ,  $n$ , and  $p$  as long as single-carrier magnetic-field dependences are not important. Unfortunately, recent data indicate that such effects are often important in semi-insulating GaAs, and thus a new approach is necessary. We suggest an approach that requires only the usual, low-field Hall-effect and resistivity parameters,  $R_0$  and  $\rho_0$ , but also assumes knowledge of the intrinsic carrier concentration  $n_i$ , and the hole mobility  $\mu_p$  as a function of the electron mobility, i.e.,  $\mu_p = f(\mu_n)$ . We describe analyses which yield

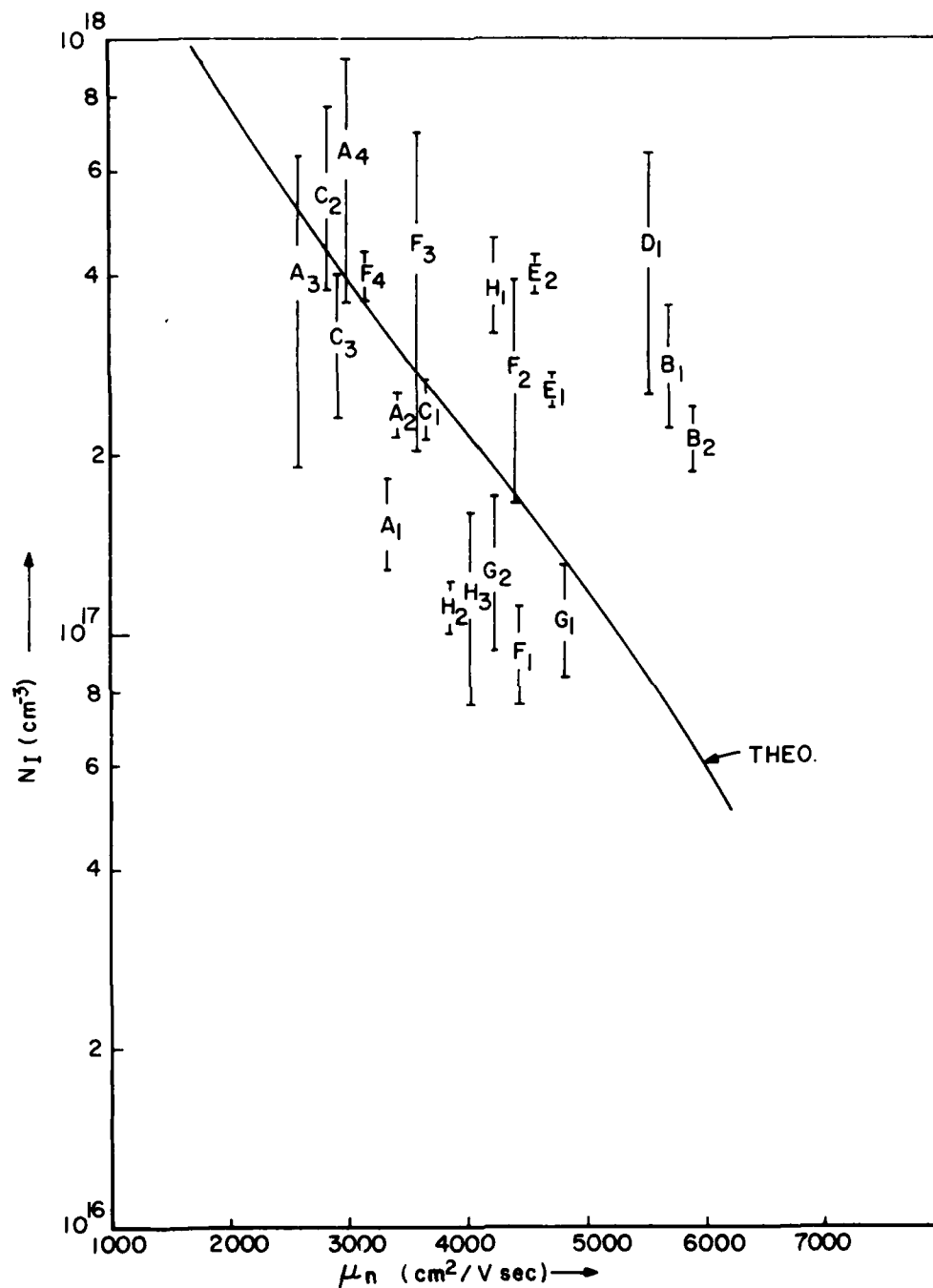


Fig. 2-4. The total ionized-impurity concentration  $N_I$  deduced from mass-spectrographic measurements versus the calculated electron mobility  $\mu_n$ . The symbols corresponds to various sample designations. The theoretical line is calculated by combining ionized-impurity scattering and lattice scattering ( $\mu_L \approx 8000 \text{ cm}^2/\text{Vsec}$ ) according to Matthiessen's rule.

$n_i \approx (2.6 \pm 0.5) \times 10^6 \text{ cm}^{-3}$ , and a tentative relationship for  $\mu_p$ , namely,  $\mu_p^{-1} \approx 9 \times 10^{-4} + 13\mu_n^{-1}$ . Curves of  $\mu_n$  vs  $R_o/\rho_o$ , with  $\rho_o$  as a parameter, are calculated by using these relationships. For  $\rho_o \leq 4 \times 10^8 \Omega\text{-cm}$ , the only solutions are  $\mu_n \approx R_o/\rho_o$ , which means that simple Hall measurements will suffice for nearly all O-doped, and undoped semi-insulating GaAs. For higher  $\rho_o$ , the solutions are double-valued, and means of selecting the proper solution are discussed. A simple compensation-distribution model is presented which yields the positions of the "O" and Cr energy levels.

Thus, the present best values of  $n_i$  and  $E_{Cr}$ , at room temperature, are<sup>31</sup>

$$n_i \approx (2.6 \pm 0.6) \times 10^6 \text{ cm}^{-3}$$

$$E_{Cr} - E_V \approx 0.74 \pm 0.02 \text{ eV.}$$

It should be emphasized that other Cr levels probably also exist. From an analysis of O-doped crystals<sup>31</sup> we believe that the dominant oxygen level is given by  $E_C - E_O \approx 0.59 \pm 0.03 \text{ eV}$ .

The true mobilities may be calculated from the curves shown in Fig. 2-5. When better SSMS data are also obtained, then the data in Fig. 2-4 can be re-plotted to more precisely test the  $\mu_n$  vs  $N_I$  relationship.

#### 2.4. The Interpretation of Photoconductivity and Photo-Hall Data

Photoconductivity (PC) and photo-Hall (PH) data are quite useful in the determination of impurity and defect energy levels in semiconductors. Illustrations of PC and PH results are given in Figures 2-6 and 2-7, respectively. The samples discussed here, A, B, and C, are Cr-doped GaAs crystals with dark Fermi levels of 0.64, 0.68, and 0.70 eV, respectively.<sup>13</sup> The peak at 0.88 eV in the PC spectra, and the dip near 1.0 eV in both the PC and PH spectra, are quite characteristic of Cr doping. It is desirable to determine the individual contributions of  $n$ ,  $\mu_n$ ,  $p$ , and  $\mu_p$  to the resultant photoconductivity. This can be done by using a mixed-conductivity analysis, developed in our laboratory,<sup>4</sup> and the results are shown in the insets of Figures 2-6 and 2-7. It is clear

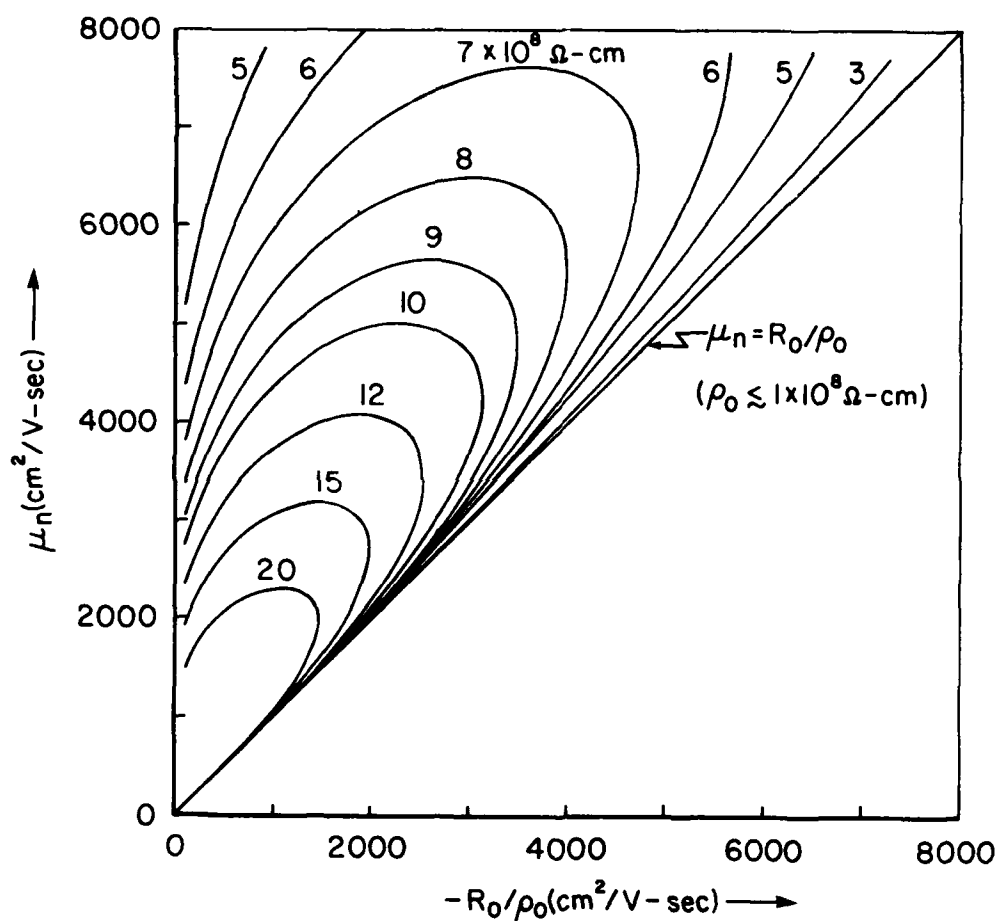


Fig. 2-5. Plots of  $\mu_n$  vs  $R_o/\rho_o$  for various values of  $\rho_o$  (units of  $10^8 \Omega\text{-cm}$ ). The assumptions are  $n_i = 2.6 \times 10^6 \text{ cm}^{-3}$ ,  $\mu_p^{-1} = 9 \times 10^{-4} + 13 \mu_n^{-1}$ , and  $r_n = r_p = 1$ . These curves hold only for samples with negative (n-type) Hall coefficients, the usual case.



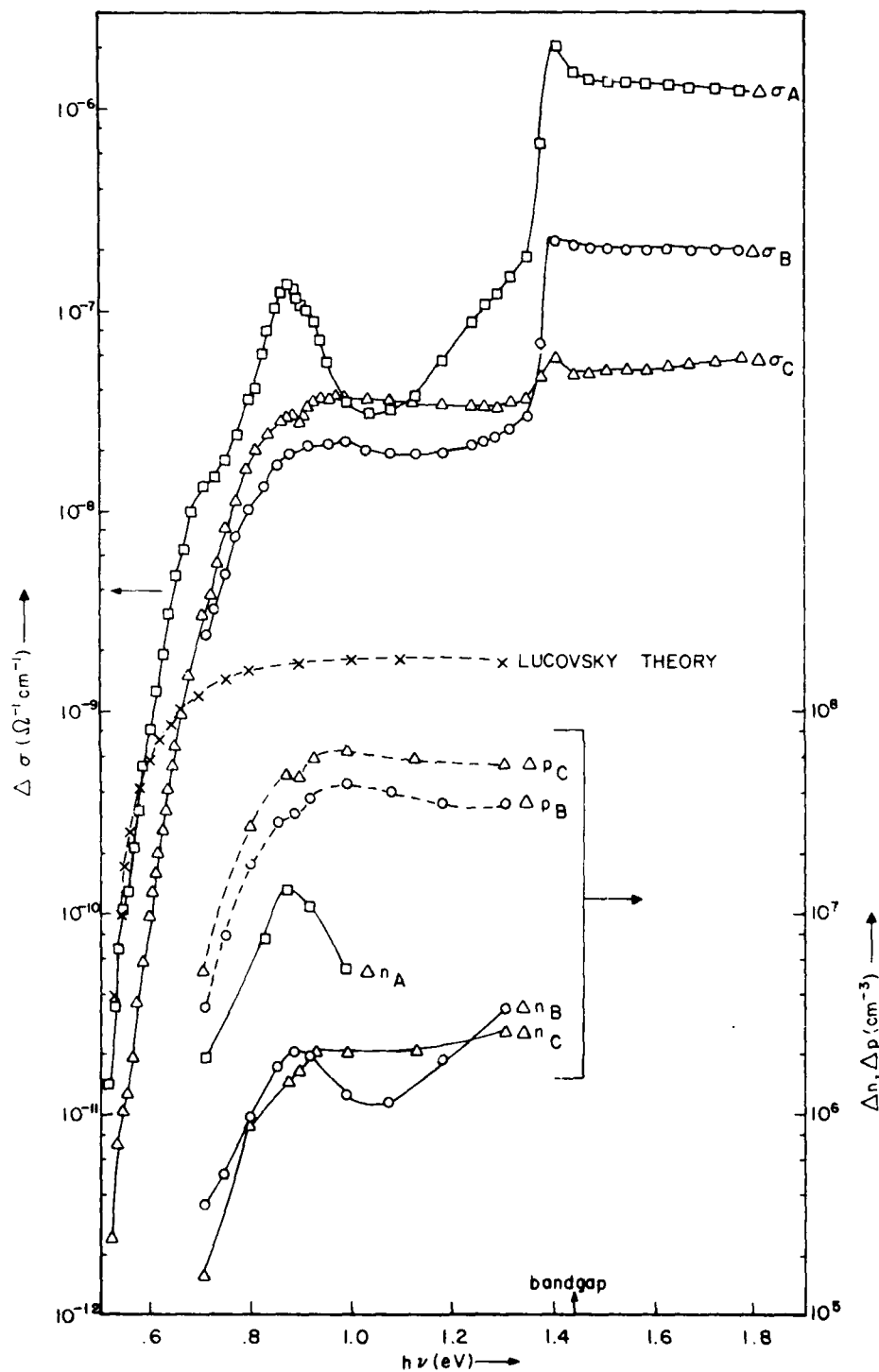


Fig. 2-6. Photoconductivity ( $\Delta\sigma$ ) and photoexcited carrier concentration ( $\Delta n$  and  $\Delta p$ ) spectral data for three GaAs:Cr samples, A, B, and C. Also shown is the Lucovsky photoionization cross section for excitation from a level at 0.52 eV. (The theory is fitted to the data at 0.53 eV.)

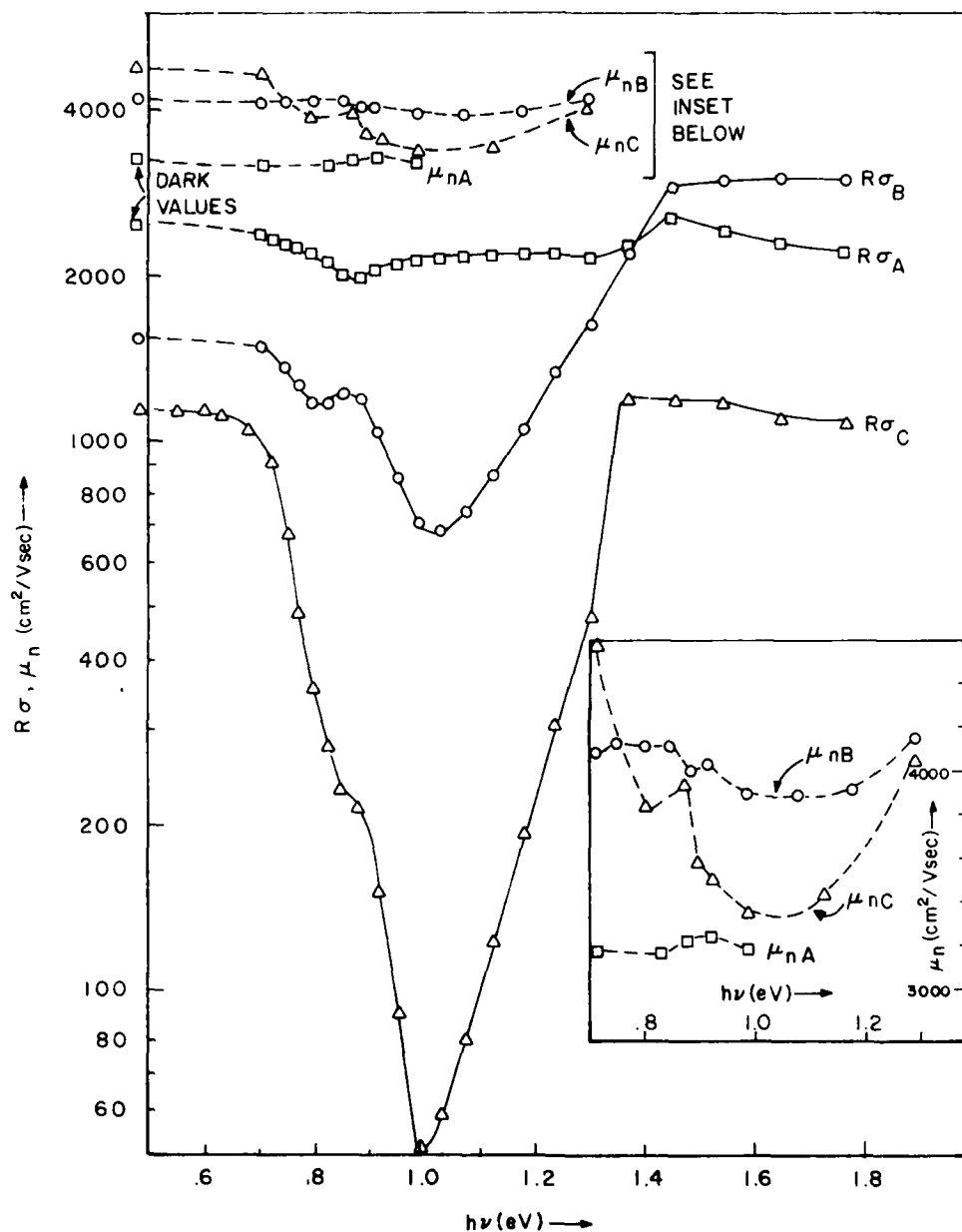


Fig. 2-7. Photo-Hall ( $R\sigma$ ) and electron mobility ( $\mu_n$ ) spectral data for three GaAs:Cr samples, A, B, and C. An expanded version of the  $\mu_n$  data is shown in the inset.

that the spectral variation of  $\mu_n$  is an important consideration for some samples, although this fact has never been considered before, to our knowledge.

In contrast to these results the PC and PH data for O-doped GaAs each have their own characteristic spectrum, as shown in Fig. 2-8. The dark Fermi levels (at 296°K) for samples B-10-S and B-5-T are 0.62 and 0.38 eV, respectively, from the conduction band, and the Arrhenius plots of  $n/T^{3/2}$  give activation energies of 0.75 and 0.43 eV, respectively. The 0.75 eV level is also commonly observed in "undoped" semi-insulating GaAs.<sup>32</sup> Recent low-temperature (100°K) PC spectra in an undoped, SI, Czochralski crystal (W 43/80) show a dominant, three-order-of-magnitude rise in PC between 0.7 and 0.8 eV. The near equivalence of the optical (PC) and thermal (electrical) values of the ionization energy, (both close to 0.75 eV) suggests that this level has only a small Franck-Condon shift. Since the 0.75 and 0.43 eV levels have been observed several times in O-doped samples it has been assumed that they are due to O. However, this assumption has recently been challenged, at least for the 0.75 eV level.<sup>33</sup> Furthermore, very recently we have estimated from electrical measurements that sample B-5-T has well over 1 ppmA of the 0.43 eV center whereas SSMS measurements list the O concentration at about 0.1 to 0.3 ppmA. Thus, the identity of this center is also open to question.

In spite of these complexities with regard to O, there seems to be little doubt that the 0.88 eV peak in Fig. 2-6 is due to Cr. The SSMS measurements are quite sensitive to Cr, and they clearly show that only samples containing appreciable quantities of Cr (relative to the shallow levels) display this PC peak. No features at this energy are seen in the O-doped or undoped SI crystals. Another unique feature of Cr-doped samples is the dip at 1.05 eV in both the PC and PH spectra.<sup>13</sup> Hole conduction is much more important in GaAs:Cr than in GaAs:O and has great influence in the spectra from 0.9-1.0 eV. The reduction (or more p-like nature) of the PH parameter ( $R_0$ ) above 0.9 eV, as seen in Fig. 2-7, is due either to a decreasing  $n/p$ , or  $\mu_n/\mu_p$ , or both.

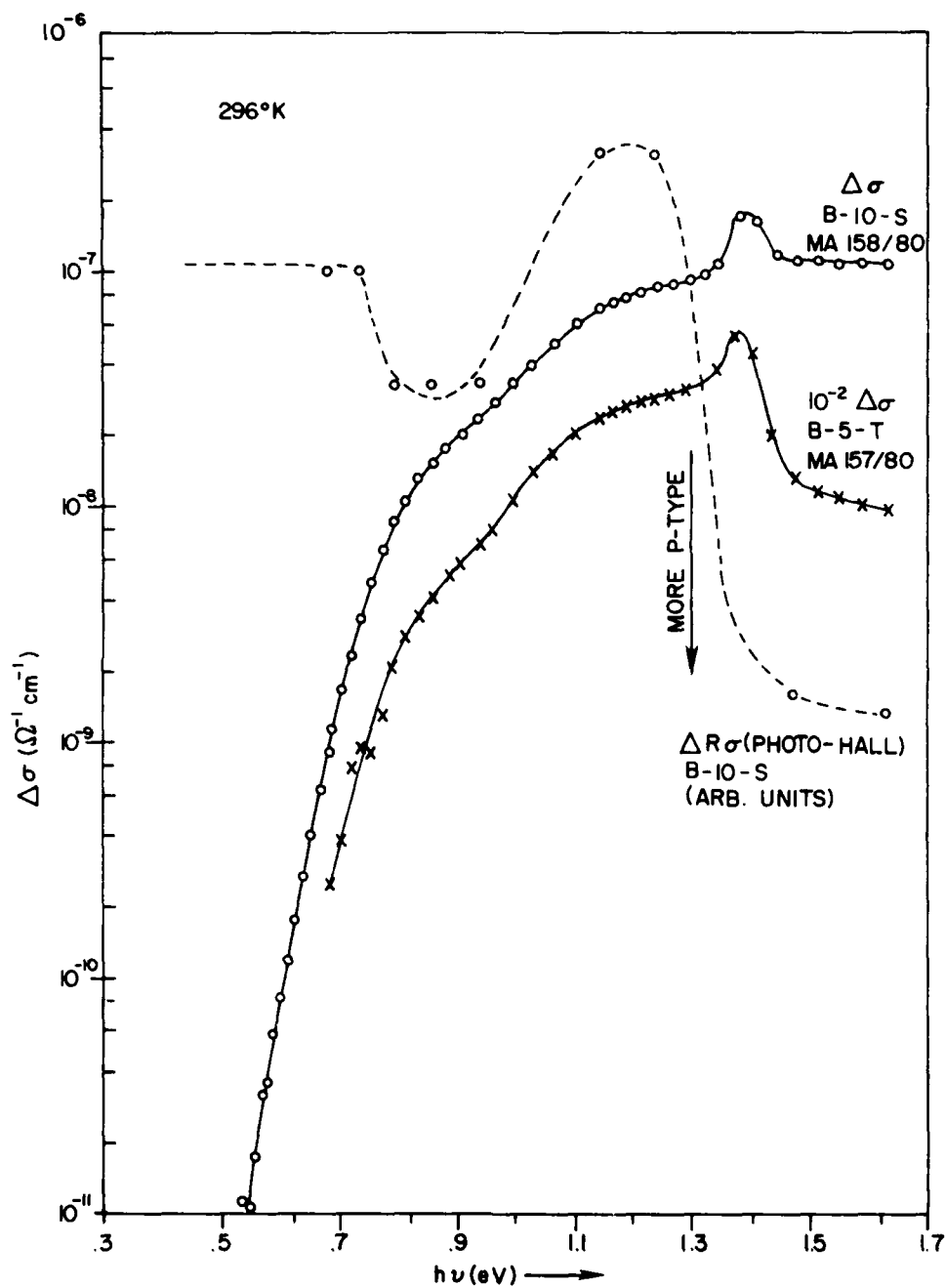


Fig. 2-8. Photoconductivity and photo-Hall data for two O-doped GaAs samples.

However, the decrease in PC above 0.9 eV (Fig 2-6) implies further that either  $n$  or  $\mu_n$  themselves must decrease, not just the ratios. The reason for a decrease in  $n$  can be twofold: (1) the increased hole concentration causes a decrease in electron lifetime; or (2) a peak is caused by a Cr intracenter resonance. These points are discussed in detail in the literature, (e.g. Ref. 13) and will not be belabored here. Some of these matters have not been fully resolved but the important technological point is that PC and PH measurements are able to distinguish O-doped SI GaAs from Cr-doped SI GaAs.

## 2.5. The Impurity Photomagnetoelectric Effect

The following abstract is reprinted from Ref. 6.

The theories of the photomagnetoelectric (PME) and photoconductivity (PC) effects in semiconductors are extended to include equal excitation rates of holes and electrons, as might be expected from impurity photo-excitation. The results are applied to two semi-insulating Cr-doped GaAs crystals, which exhibit mixed conductivity. It is seen that the PC and PME effects give complementary information on the holes and electrons. In the impurity excitation region the PME current responds strongly to changes in the absorption coefficient, and provides a convenient way to study this quantity.

The introduction from this paper is also reprinted.

Semi-insulating GaAs, produced by doping with Cr and/or O is widely used as a substrate material for GaAs devices. Because of this it has been studied extensively by many techniques in recent years, including the photomagnetoelectric (PME) effect. However, the PME effect varies strongly with the absorption constant ( $\alpha$ ), and, thus, as far as we know, has been experimentally applied to semiconductors only in the intrinsic photoexcitation region, where  $\alpha$  is large. This is true of the available theoretical treatments also, which are formulated under the condition that electrons and holes are excited at equal rates. For extrinsic (impurity, or defect) photoexcitation this condition may not hold, so the theory must be extended. In semi-insulating Cr-doped GaAs we have found

that the PME response can be measured down to about 0.6 eV, much lower than the intrinsic response, which cuts off at about 1.42 eV, the room-temperature bandgap. In this paper we develop the theory of the impurity PME and photoconductivity (PC) effects and use the results to elucidate the nature of the Cr energy levels in GaAs:Cr.

## 2.6. Infrared Spectral Detectivity of GaAs:Cr

The following abstract is reprinted from Ref. 34.

The room-temperature spectral detectivity of Cr-doped GaAs has been examined in the impurity excitation region out to 1.7  $\mu$ , a range which includes the wavelengths of several important laser as well as low-loss optical fibers. The results include values of  $D^*$  greater than  $10^{11}$  cm Hz<sup>1/2</sup>/W in the photoconductive mode, and  $10^{10}$  cm Hz<sup>1/2</sup>/W in the photomagnetolectric mode. Small carrier lifetimes,  $\sim 10^{-8}$  sec, offer the potential of high-speed operation; however, the measured response times are much larger,  $\sim 10^{-3}$ - $10^2$  sec, because of very high input impedances. Formulas are presented to show the variation of  $D^*$  with relevant parameters, and means of improving the performance are discussed.

The introduction from this paper is also reprinted.

In the course of some recent room-temperature dc photoconductivity measurements on semi-insulating GaAs:Cr, it was realized that many of the samples have as appreciable photoresponse at wavelengths up to 1.7  $\mu$ , well beyond the band gap of 0.87  $\mu$ . Since this response covers the intrinsic ranges of Si and Ge, several important laser wavelengths, and the low-loss region for optical fibers, it seemed worthwhile to investigate the infrared detectivity characteristics of GaAs:Cr, especially since it is already in wide use as a substrate material for GaAs FET;s and integrated circuits. In this paper, we first present formulas for the low-frequency thermal-noise-limited photoconductive (PC) and photomagnetolectric (PME) detectivities ( $D^*$ ), in the intrinsic and extrinsic excitation regions, and then present data for  $D^*$  as a function of wavelength in

two representative GaAs samples. Advantages, disadvantages, and possible methods of detector-performance improvement are discussed.

The spectral variations of  $D^*$  for GaAs:Cr operated in the PC and PME modes, and for undoped GaAs in the photovoltaic (PV) mode, are shown in Fig. 2-9.

## 2.7. Energy Levels

The Arrhenius plot ( $\ln n$  or  $p$  vs.  $T^{-1}$ ) is a well-known method for determining a high-precision value of a deep energy level at  $T = 0^\circ\text{K}$ . For finite-temperature values, some oft-used methods are the PC, PH, and PME effects, discussed earlier. Finally, we have used a special method, described in References 7 and 31, to determine room-temperature values of the dominant energy level in GaAs:Cr and GaAs:O. Some of the results are given in Table 2-1; only ionization energies greater than 0.4 eV are included in this discussion. Shallower levels are discussed in Sec. 3.

Several observations may be made. First, the Cr activation energies vary over a rather large range (.68 to .81 eV). The most likely reasons for this are the following: (1) the mixed-conductivity analysis is not always correct because of single-carrier effects; (2) other centers with similar activation energies (probably O) are competing with the Cr; or (3) the temperature dependences are not correct due to inhomogeneous material, etc. The first problem can be taken care of by extending the analysis described in Sec. 2 to higher temperatures. The second problem can be solved by simply adding a term for O (or some other center) in the charge balance equation. However, the analysis will then no longer be so simple. In short, from the Arrhenius plots of Cr-doped GaAs we know only that Cr forms a deep level close to mid-gap.

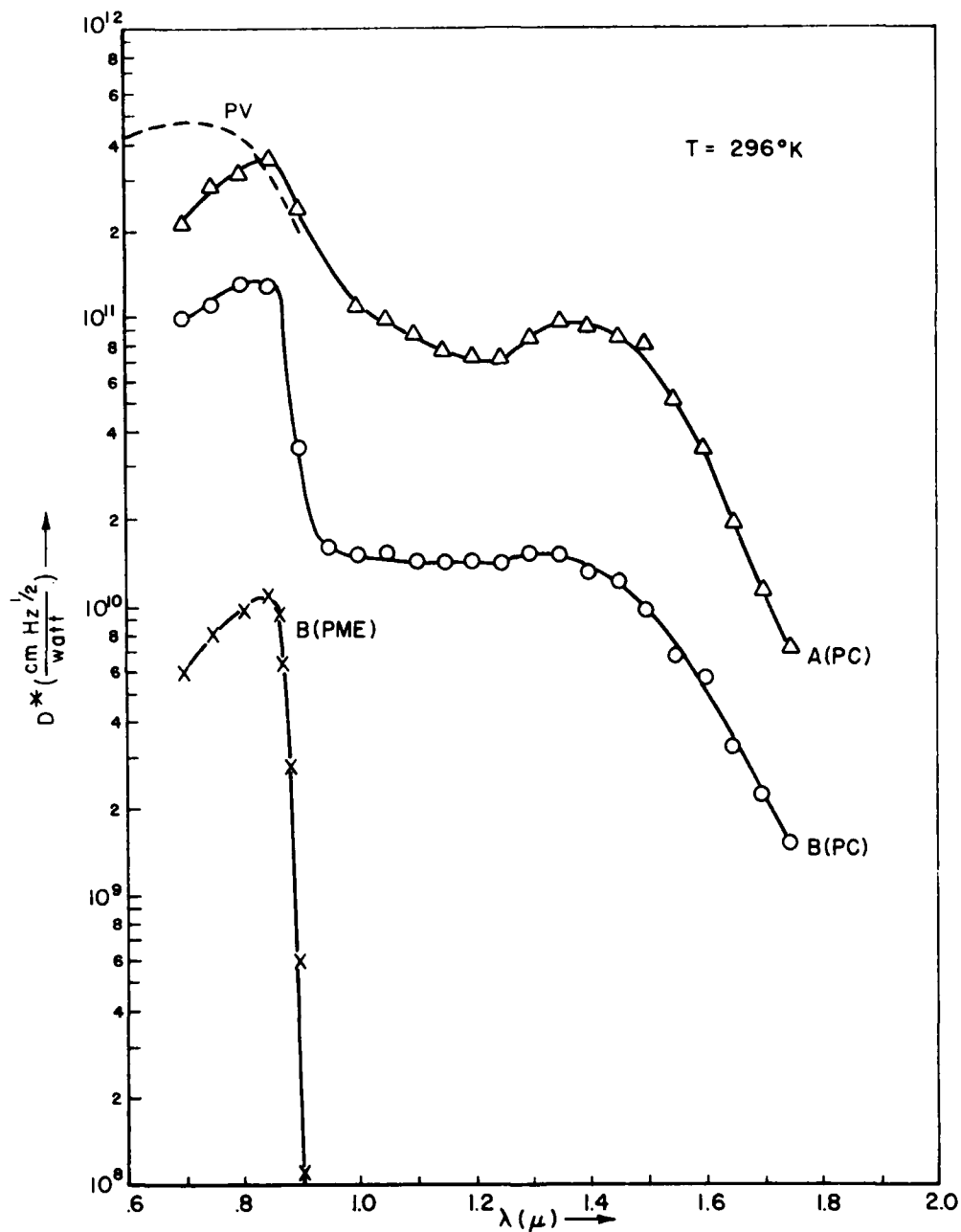


Fig. 2-9. The measured room-temperature spectral detectivities of GaAs:Cr samples A and B, operated in photoconductive (PC) and photomagnetolectric (PME) modes. The chopping frequency and bandwidth are both 7.5 Hz. Also shown is a GaAs sample operated in the photovoltaic (PV) mode at 90 Hz, from P. W. Kruse et al, Elements of Infrared Technology (Wiley, New York, 1962).



Table 2-1. Energy levels in semi-insulating GaAs.

<u>Sample</u>	<u>Doping</u>	<u>Energy Level</u> <u><math>E_C - E_T</math> (eV)</u>	<u><math>T(^{\circ}\text{K})</math></u>	<u>Method</u>
LD 6-10	Cr	$.77 \pm .02$	0	Arrhenius plot-Hall effect
Var	Cr	$.75 \pm .02$	0	Arrhenius plot-Hall effect
Sum 11/76	Cr	$.81 \pm .02$	0	Arrhenius plot-Hall effect
LD 2	Cr	$.78 \pm .02$	0	Arrhenius plot-Hall effect
Var 66-1	Cr	$.77 \pm .02$	0	Arrhenius plot-Hall effect
Mor 56/76	Cr	$.68 \pm .02$	0	Arrhenius plot-Hall effect
Mor 57/76	Cr	$.75 \pm .02$	0	Arrhenius plot-Hall effect
Mons 0	0	$.76 \pm .01$	0	Arrhenius plot-Hall effect
MA 158/80	0	$.75 \pm .01$	0	Arrhenius plot-Hall effect
W 43/80	none	$.76 \pm .01$	0	Arrhenius plot-Hall effect
Many different Samples	Cr	$.69 \pm .02$	$300^{\circ}\text{K}$	See Ref. 31
Many different Samples	0, or none	$.59 \pm .03$	$300^{\circ}\text{K}$	See Ref. 31

The situation is different for O-doped (or undoped) SI crystals. We and most others have found the same activation energy in all samples:  $0.76 \pm .01$  eV. Mixed conductivity effects are not important in this case.<sup>31</sup> To interpret this result we can apply the well-known formula

$$n = \frac{N_{DD}}{N_A - N_D} \frac{N_c}{2} e^{-E_{DD}/kT} \quad (2-1)$$

where  $N_{DD}$ ,  $N_D$ , and  $N_A$  are the densities of deep donors, shallow donors, and all acceptors below  $E_{DD}$ , respectively. Equation 2-1 is valid if  $n \ll N_A$ ,  $N_D - N_A$ , certainly the case here. A linear temperature dependence can be assumed for  $E_{DD}$ ; i.e.,  $E_{DD} = E_{DD0} + \alpha T$ , at least over a certain temperature range.

Then

$$n = \frac{N_{DD}}{N_A - N_D} \frac{N_c}{2} e^{-\alpha/k} e^{-E_{DD0}/kT} \quad (2-2)$$

The measured activation energy is just the slope of a  $\ln n$  vs  $T^{-1}$  plot, i.e.,  $-E_{DD0}/k$ , so that 0.76 eV is effectively the "oxygen" level at  $T = 0$ . Since we know the value of  $N_c/2$  (a donor degeneracy of 2 is assumed here) the quantity  $N_{DD}(N_A - N_D)^{-1} \exp(-\alpha/k)$  may also be obtained. We expect  $\alpha$  to be somewhere in the range 0 to  $-5 \times 10^{-4}$  eV/ $^{\circ}$ K, since the former would correspond to the level being tied to the conduction band, and the latter, to the valence band. Consider sample MA 158/80: if  $\alpha = 0$ , then  $N_{DD}(N_A - N_D)^{-1} \approx 3.8 \times 10^2$ , whereas if  $\alpha = -5 \times 10^{-4}$ , then  $N_{DD}(N_A - N_D)^{-1} \approx 1.4$ . The latter is a much more reasonable value, suggesting that the "oxygen" level may be more closely tied to the valence band than the conduction band. However, more work is needed to verify this conclusion.

The room-temperature O and Cr levels in Table 2-1 were obtained by a somewhat complicated analysis, described in Sec. 2-3 and in References 7 and 31.

It is interesting that a rough value of  $\alpha$  for the O level would be given from these data as  $\alpha \approx -(.76 - .59)/300 \approx -6 \times 10^{-4} \text{ eV/}^\circ\text{K}$ , quite consistent with the previous value and with the assertion that the O level is tied more closely to the valence band. The Cr center, on the other hand, appears to remain close to mid-gap as the temperature varies.

### 3.0 ELECTRICAL MEASUREMENTS IN SEMICONDUCTING GaAs

#### 3.1 Introduction

As mentioned in Sec. 2.2, we have performed electrical measurements, some simple and some extensive, on nearly 600 GaAs and InP samples during this contract period. Of these 600 samples, about 400 were epitaxial layers, mostly VPE, and 200 were substrates, mostly semi-insulating. In general, the n-type VPE layers were measured at 300 and 77°K, respectively, and then the analysis of Wolfe et al was applied to determine  $N_D$  and  $N_A$ . These same techniques were carried out for certain of the more pure, bulk, n-type GaAs samples, if the Fermi level was dominated by a shallow (hydrogenic) donor. In cases for which the Fermi level was deeper the  $n$  vs  $T$  data could sometimes be fitted by a well-known formula derived from the charge balance equation, which then yielded  $N_D$ ,  $N_A$ , and  $E_D$ .<sup>35</sup> A similar analysis could often be applied to p-type samples, also, as long as  $E_A \lesssim 0.2$  eV. The results are discussed below.

#### 3.2 Donor and Acceptor Concentrations

It would be pointless and belaboring to enter into this report all the data accumulated for 400 samples. This has been done in the monthly reports, No. 1 (June, 1976) to No 54 (November, 1980). We will confine ourselves to some of the highlights.

The highest measured 77°K VPE mobility was about  $180,000 \text{ cm}^2/\text{V-sec}$ . This sample had a 300°K electron concentration of  $1 \times 10^{14} \text{ cm}^{-3}$ , giving  $N_D \approx 1 \times 10^{14}$ ,  $N_A = 2 \times 10^{13} \text{ cm}^{-3}$ . This crystal also gave very sharp photoluminescence lines. Unfortunately, these excellent electrical properties were not always repeatable, pointing out the great difficulties in controlling impurities and defects at the ppb levels.

The best MBE crystal grown here had a 77°K mobility of about 35,000 cm<sup>2</sup>/V-sec, with  $N_D \approx 3 \times 10^{15}$ ,  $N_A \approx 2 \times 10^{15} \text{ cm}^{-3}$ . The MBE samples are typically not as good as VPE samples, evidently at least partially due to a less pure As source. However, recently a group at Lincoln Laboratories has succeeded in growing MBE layers with 77°K mobilities of about 140,000 cm<sup>2</sup>/V-sec, by using AsH<sub>3</sub> as the source.<sup>36</sup> This is a major breakthrough and greatly enhances the future of MBE for microwave devices.

Bulk GaAs, grown by the Bridgeman or Czochralski techniques, is nearly always more impure than epitaxially grown GaAs of even moderate quality. However, we have noticed a gradual improvement in quality over the last 3-4 years. The best bulk crystal observed so far had  $N_D \approx 7 \times 10^{15}$  and  $N_A \approx 2 \times 10^{15} \text{ cm}^{-3}$ , calculated from an Arrhenius plot. This particular crystal had  $n \approx 1.1 \times 10^{15} \text{ cm}^{-3}$  and  $\mu_n \approx 5.3 \times 10^3 \text{ cm}^2/\text{V-sec}$  at room temperature, indicative of fairly good epilayer quality, at first glance. However, in this case, and several others like it, a deeper donor (0.15 eV) dominates the electrical properties and the equality  $n \approx N_D - N_A$  (at room temperature) is no longer true. This fact is not recognized by many of the crystal vendors as well as the users and some claims of "epilayer-like" purity have simply not been true. This caveat notwithstanding, we believe that bulk crystal quality has been steadily improving in general, with perhaps the biggest advance being the suppression of silicon. Controlling the silicon is usually accomplished by introducing an oxygen partial pressure, which can be done in various ways.

### 3.3 Energy Levels

Table 3-1 shows the energy levels measured as the slopes of Arrhenius plots in p-type, epitaxial GaAs layers. (Most of the p-type bulk samples studied here have been controlled by shallow levels, which will not be considered in this report.) As discussed in a previous section, we interpret these slopes as being acceptor ionization energies at  $T = 0$ . The samples described in Table 3-1 are considered to be representative of all of the p-type epilayers

Table 3-1. Ionization energies of p-type GaAs epitaxial layers

<u>Sample</u>	<u><math>E_A - E_V</math></u>	<u>Sample</u>	<u><math>E_A - E_V</math></u>
HP-C-7-2-1	shallow $\sim .03$ eV	HP-C-4-3-1	0.47 eV
HP-C-4-1-7	.036, .048 eV	TI76B-21B	0.48
HP-C-4-2-3	0.14	RCA 2516	0.49
RAY 72099	0.14	VAR CR38-4	0.50
HP-C-4-2-4	0.15	TLD 9-66	0.51
HP-C-3-3-4	0.17	TI 118/76	0.53
RAY B362	0.21	HP-C-7-2-2	0.53
HP-C-4-1-9	0.22		
HP-C-4-3-5	0.35		

Notes: HP  $\equiv$  "high purity" sample grown at AFWAL/AADR

RAY  $\equiv$  Raytheon

TI  $\equiv$  Texas Instruments

VAR  $\equiv$  Varian

TLD  $\equiv$  Teledyne

that we have measured; it is clear that the preponderance of crystals are controlled by deep acceptor levels ( $>>0.03$  eV). (Most of the other samples have simple not been studied in as much detail, due to a lack of time and technical help.)

The first observation from Table 3-1 is that many different levels exist in the lower half of the GaAs band gap, agreeing with the multitude of literature on acceptor levels. This fact is mentioned because it is in stark contrast to the situation in the upper half of the band gap. The second observation is that there clearly is an often dominant level at  $0.50 \pm 0.03$  eV, appearing in samples from five different crystal growers. We believe that this level may be associated with a defect since it is also observed in electron-irradiated epitaxial layers.

For n-type semiconducting samples shallow ( $<10$  meV) donors nearly always predominate. Indeed, this has been the case in every single n-type VPE layer (over 200) that we have examined. This situation also obtains for most of the n-type bulk crystals observed by us as well as others. Recently, however, several samples, especially from Crystal Specialities and Morgan Semiconductor, have been found to be controlled by levels about  $0.12 - 0.20$  eV below the conduction band. It should be noted that some of these samples were doped with oxygen, which probably suppressed the common shallow donor, silicon. The data are given in Table 3-2. Also included are data on a VPE layer HP-C-4-2-1, which was irradiated with  $1 \times 10^{14}/\text{cm}^2$ , 1 MeV electrons. The activation energy of this sample is in the range of the other activation energies reported here. (Note that  $N_{DS}$  in Table 3-2 is the concentration of "shallow" donors, i.e., donors lying above the level in question)

Table 3-2. Electrical properties of several, bulk, n-type GaAs samples.

Sample	$n(10^{16} \text{ cm}^{-3})$ at 300°K	$N_D(10^{16} \text{ cm}^{-3})$	$(N_A - N_{DS})(10^{16} \text{ cm}^{-3})$	$E_D(\text{eV})$	$C(10^{13} \text{ cm}^{-3})$
MOR 6-43-1	.26	3-7	2-6	.127	15-45
MOR 11-44-1	.29	3-4	2-3	.127-.128	20-50
HP-C-4-2-1	.0037	.007-.015	.003-.012	.141-.142	2-8
CS 4422-2	.12	.7-.8	.2-.3	.151-.153	6-14
CS 3417	.11	.9-1.4	.4-1.0	.151-.152	10-25
CS 4422-1	.085	.9-1.9	.5-1.5	.156-.157	15-45
MA 124-80	.059	.9-2.9	.7-2.7	.160-.161	20-100
CS 3025-2	.084	1.0-2.3	.5-1.9	.169	25-80
CS 2531-3	.056	.5-.8	.2-.6	.199	40-110

Notes: MOR  $\equiv$  Morgan Semiconductor

HP  $\equiv$  "High Purity" VPE sample grown at AFWAL/AADR

CS  $\equiv$  Crystal Specialties

MA  $\equiv$  Microwave Associates



It is seen that the donor and acceptor concentrations are in the range 0.1 - 1 ppmA ( $1 \text{ ppmA} = 4.4 \times 10^{16} \text{ cm}^{-3}$  in GaAs). Thus, it can be safely said that these crystals are more pure than most of the bulk crystals available several years ago. Evidently, part of the reason for this is that the Si has been suppressed. The next question concerns the identification of the impurities remaining. Several of these samples are presently being analyzed by SSMS and atomic emission techniques in an attempt to answer this question.

It should be noted that we have implicitly assumed that the centers being discussed here are donors. However, the temperature-dependent Hall data can also be fitted by a different equation which is based upon acceptor behavior of the centers. Unfortunately, the "goodness of fit" is about the same in both cases, and a choice cannot be made on this basis. In the acceptor case the activation energies are about the same, but of course  $N_D \rightarrow N_A$  and  $N_A - N_{DS} \rightarrow N_D - N_{AS}$ , with  $N_A > N_D - N_{AS}$ . The other parameter determined from the fit, and one which again is about the same for either the donor or acceptor case, is  $g \exp(-\alpha/k)$ , where  $g$  is the degeneracy factor and  $\alpha$  is the temperature coefficient (see the discussion in Sec. 2.7). This factor is contained in  $C$  (Table 3-2), since  $C = 8 \times 10^{13} g \exp(-\alpha/k)$ . For a "classical" donor, tied to the conduction band, we might expect  $g = \frac{1}{2}$  and  $\alpha = 0$ , giving  $C = 4 \times 10^{13}$ . Only sample HP-C-4-2-1 could have these parameters, since  $2 < C < 8 \times 10^{13}$  for this crystal. For a "classical" acceptor tied to the valence band we would expect  $g = 4$  and  $\alpha = -5 \times 10^{-4}$ , or  $C = 1300 \times 10^{13}$ . None of the samples satisfy this case. If we go back again to  $g = \frac{1}{2}$ , then a range in  $\alpha$  from 0 to  $2 \times 10^{-4} \text{ eV}/^\circ\text{K}$  would include all of the samples, and a range from 0 to  $1.5 \times 10^{-4} \text{ eV}/^\circ\text{K}$  would include all but one of the samples. Since such a range of  $\alpha$  is quite reasonable, a conclusion that all of these centers are "simple" donors is not inconsistent with the data.

Another obvious question is then whether or not these centers could all be the same, or perhaps "mixtures" of, say, only two different centers. It is easy to show that two centers, of activation energies  $E_1$  and  $E_2$ , respectively, could experimentally look like one center, with  $E_1 < E < E_2$ , if  $|E_1 - E_2| \ll kT$ . However, at the temperatures of our data,  $kT \approx .03$  eV, but the spread in activation energies is  $\approx .07$  eV. Thus, it does not appear that only one or two different centers are involved here. There are some obvious similarities among the samples, however. For example, MOR 6-43-1 is nearly equivalent to MOR 11-44-1, and also CS 4422-1, CS 4422-2, and CS 3417 could be exhibiting the same center. One other possibility is that all of these centers are similar in that they have a common characteristic. For example, they could all consist of a particular lattice defect, say a vacancy, complexed with different impurities, say Si or S. This is an attractive possibility because it is almost certain that HP-C-4-2-1, the irradiated sample, exhibits a defect related state, perhaps a Ga vacancy. The states observed in the bulk crystals might then be  $V_{Ga}$ -Impurity complexes. More work needs to be carried out to test some of these ideas.

#### 4.0 ELECTRICAL AND PHOTOELECTRONIC PROPERTIES OF SEMI-INSULATING InP

##### 4.1 Introduction

The following introduction is reprinted from Ref. 37.

The highest resistivity form of single-crystal InP known to date results from doping with iron.<sup>38</sup> Typical resistivities measured in this laboratory and others<sup>27,38,39</sup> range from  $(1 - 8) \times 10^7 \Omega\text{cm}$ , less than an order of magnitude below the intrinsic resistivity of about  $1 \times 10^8 \Omega\text{cm}$ . Thus this material has already found great usefulness in providing high-resistivity substrates for certain InP and GaInAsP devices. Since its recent discovery, many investigations of the electrical and optical properties have taken place and certain aspects of the Fe centers are now reasonably well understood. For example, Arrhenius plots of the Hall coefficient or resistivity indicate an energy level at 0.64 - 0.68 eV below the bottom of the conduction band.<sup>27,38,39</sup> Furthermore, zero-phonon lines have appeared in low-temperature luminescence and absorption spectra near 0.35 eV and these have been interpreted by Koschel et al.<sup>40</sup> as intracenter transitions in  $\text{Fe}^{2+}$ . Nearly the same sharp absorption lines have been reported by Ippolitova et al.<sup>39</sup> at 20 K, and these authors have also seen a broad absorption band, near 0.4 eV, at 78 and 300 K. This broad band at 300 K was studied in more detail by Iseler,<sup>29</sup> who observed its peak at 0.44 eV.

We have seen, for the first time, a photoconductivity peak in InP:Fe. The position and shape of the photoconductivity spectrum are much like those of the 0.44 eV absorption spectra studied by Iseler<sup>27</sup> and by Ippolitova et al.<sup>39</sup> We interpret the photoconductivity as resulting from an  $\text{Fe}^{2+}$  intracenter optical excitation followed by a thermal excitation to the conduction band. In this paper we will attempt to explain the origin of the 0.44 eV absorption band and its relationship to the photoconductivity spectrum.

#### 4.2 Resonance Photoconductivity

The photoconductivity spectrum is shown in Fig. 4-1. The resonance peak is clearly evident at 0.44 eV. Also shown is a theoretical fit, described in Ref. 37.

The room-temperature energy diagram, deduced from the PC and dark Arrhenius plot data, is shown in Fig. 4-2. Discussion is given in References 23 and 37.

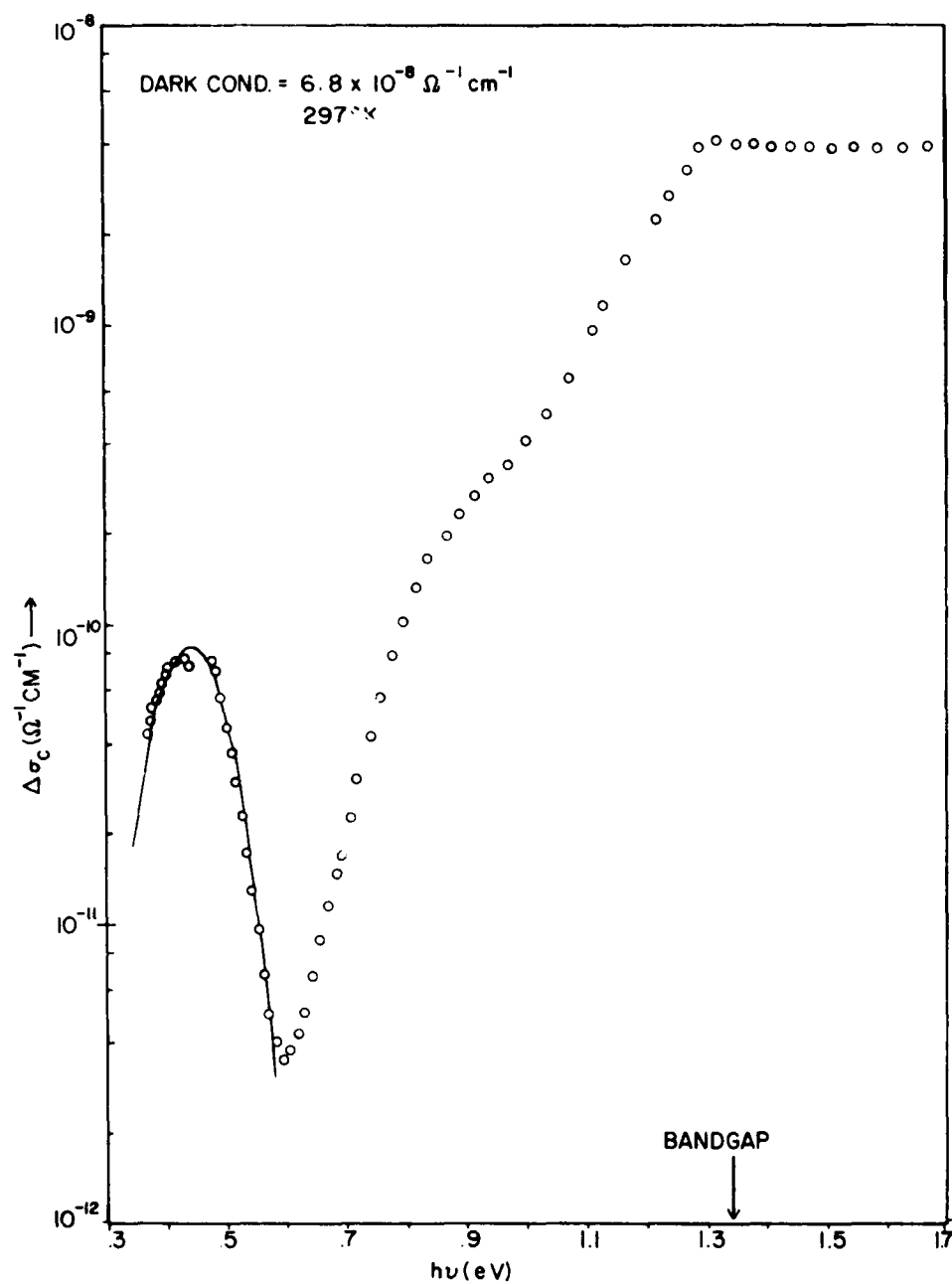


Fig. 4-1. The spectral dependence of the photoconductivity in InP:Fe at 297 K. The solid line is a theoretical fit with parameters as given in Ref. 37.

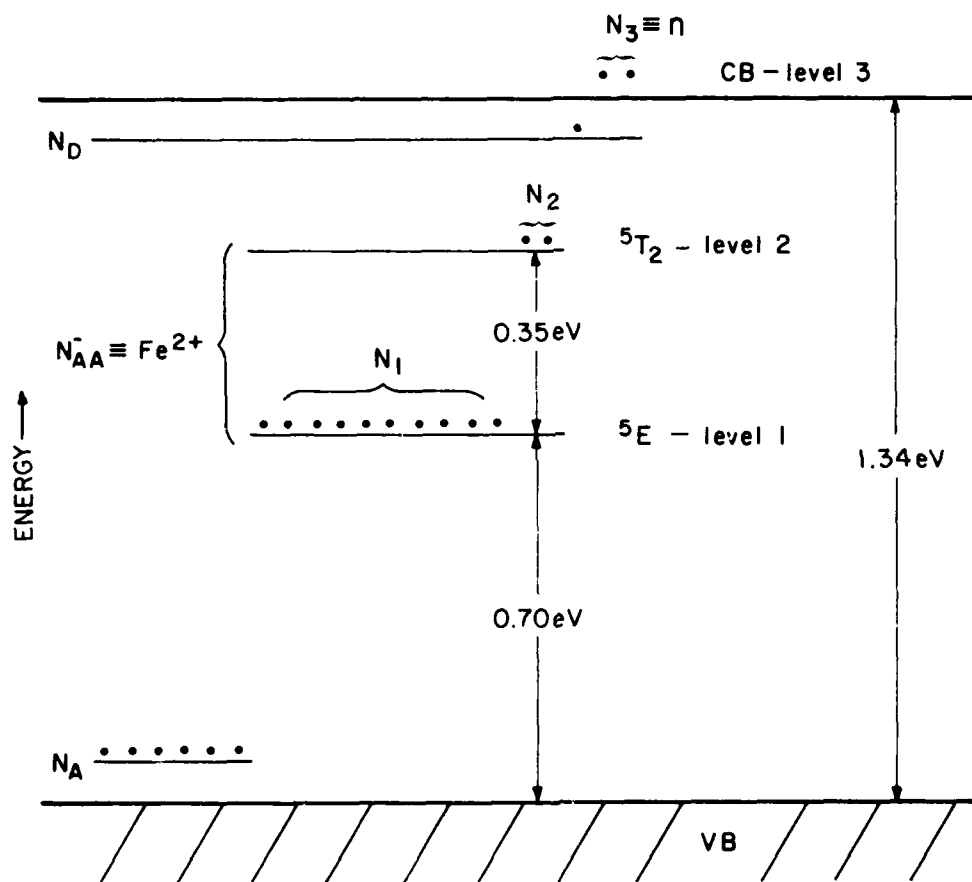


Fig. 4-2. Proposed room-temperature energy diagram for  $Fe^{2+}$  in InP. The various listed quantities are explained in Ref. 23.

## 5.0 PHOTOLUMINESCENCE IN HEAT-TREATED GaAs

### 5.1 Introduction

GaAs device fabrication involves a heat treatment at elevated temperatures through the process of either epitaxial growth or ion implantation. The heat treatment of substrate materials usually indicates the formation of vacancies, related complexes, and the migration of impurities. The out-diffusion<sup>41</sup> of Cr has been observed during a heat treatment. This phenomenon leads to an explanation of n-type conversion at the surface and also to the presence of Cr-related emission<sup>42</sup> in epitaxial layers. In particular, the emission at  $\sim 1.40$  eV has been reported in both as-grown and heat-treated GaAs. The origin of this band is thought to be due to an atomic complex of  $\text{Si}^{43}$ ,  $\text{V}_{\text{As}}^{44}$ ,  $\text{V}_{\text{As}}$ -acceptor complex<sup>45</sup>, or  $\text{V}_{\text{Ga}}^{46}$ . Also, this band at  $\sim 1.40$  eV has been obtained<sup>47</sup> from Mn-doped crystals and from the near-surface region of heat-treated, semi-insulating GaAs<sup>48</sup>. The near-surface region was thermally converted to a high conducting state. Therefore, the radiative mechanisms involved with Mn were investigated<sup>9</sup> by implanting Mn ions.

### 5.2 Mn-implanted GaAs

The following is the abstract of Ref. 9.

The emission properties of Mn-implanted layers in GaAs are investigated with respect to changes in excitation intensity, temperature, substrate, and encapsulation. The substrates used were n-type conducting and Cr-doped semi-insulating crystals. The depth-dependent measurements of the Mn emission show an increase of the diffusion coefficient with dose for  $\text{Si}_3\text{N}_4$  encapsulated samples, whereas a suppression of Mn diffusion is observed for  $\text{SiO}_2$  encapsulated samples. A large energy shift from  $\sim 1.36$  to  $1.41$  eV is observed for Mn emission at  $4.2^\circ\text{K}$  at various excitation intensities. The energy shift increases with

the concentration of compensating donors in the n-type substrate material. The excitation-dependent emissions are due to the donor-acceptor pair type transitions in the normal and the random-impurity-potential-disturbed energy states of the bands. Another emission becomes dominant at  $T > 30^\circ\text{K}$  following the quenching of the donor-acceptor pair type transitions with an increase of the temperature. An activation energy  $95 \pm 15$  meV is obtained from the temperature quenching of the emission intensity and the energy shift is observed to follow the band-gap variation. The possible radiative mechanisms are discussed.

The room-temperature electrical properties, growth process of the substrate materials, and Mn-emission shapes are shown in Table 5-1. Typical  $4.2^\circ\text{K}$  emission spectra from Mn-implanted layers are shown in Fig. 5-1, curves (b) and (c). The luminescence consists of a band-edge emission at 1.513 eV, a band related to the Si acceptor at 1.489 eV, and emission bands due to Mn. The Mn emission is characterized by a no-phonon line at  $\sim 1.40$  eV and the replicas of longitudinal optical phonons and transverse acoustic phonon as shown in Fig. 5-1, curve (b). However, some samples show a broad no-phonon line with the smearing of the transverse acoustic phonon. This difference of the emission shape is observed to depend on substrates, the details being summarized in Table 5-1. The features of the luminescence in the implanted layers are also influenced by the type of encapsulation. Samples in Fig. 5-1 curves (a) and (b) were cut from a wafer implanted with a dose of  $5 \times 10^{14} \text{ cm}^{-2}$ , capped with  $\text{SiO}_2$  and  $\text{Si}_3\text{N}_4$ , respectively, and annealed at  $800^\circ\text{C}$ . The samples capped with  $\text{SiO}_2$  show another emission band at  $\sim 1.36$  eV with its phonons in addition to the 1.40-eV emission. The band at 1.36 eV is known to be due to Cu in a Ga site. This indicates that more Ga vacancies are formed in the samples capped with  $\text{SiO}_2$  compared to  $\text{Si}_3\text{N}_4$ . The presence of the 1.36-eV emission in the samples capped with  $\text{SiO}_2$  was mainly observed in the implanted layers of Cr-doped substrates.



Table 5-1. Room-temperature electrical properties, growth process of substrate materials, and the Mn-emission shape.

<u>Substrate No.</u>	<u>Carrier conc. n (cm<sup>-3</sup>)</u>	<u>Mobility <math>\mu</math> (cm<sup>2</sup>/V sec)</u>	<u>Growth process</u>	<u>Mn emission</u>
1	$1.2 \times 10^{14}$	4200	EPI, undoped	TA
2	$4.2 \times 10^{16}$	3100	MG, undoped	No TA
3	$5.0 \times 10^{17}$	2670	MG, Sn	No TA
4	Semi-insulating	...	MG, Cr	TA
5	Semi-insulating	...	MG, Cr	No TA

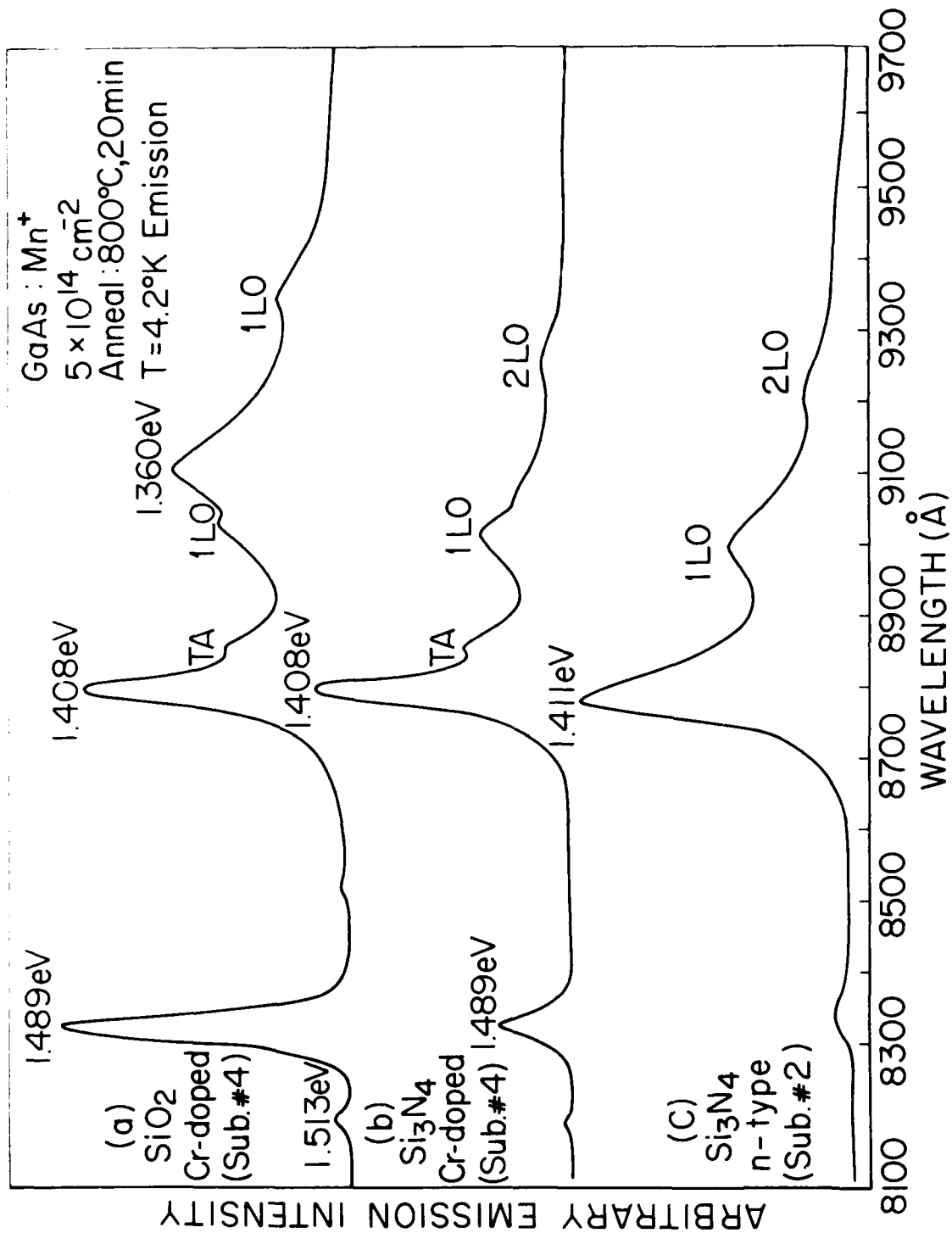


Fig. 5-1. Emission spectra obtained from Mn-implanted layers to a dose of  $5 \times 10^{14} \text{ cm}^{-2}$  and then annealed at  $800^\circ\text{C}$ . The samples for curves (a) and (b) are from one wafer. The presence of 1.36-eV emission for curve (a) is due to  $SiO_2$  encapsulation. The broadness of the no-phonon line for curve (c) is due to the substrate used for Mn implantation.

### 5.3 Discussion of the Mn-Related Emissions

As is well known from the emission spectra of shallow acceptors, donor-acceptor (D-A), and conduction-band-to-acceptor (C-A) transitions are clearly resolved with changes of excitation intensity and temperature. C-A transitions are dominant with the quenching of D-A emissions with an increase of temperature. Likewise, for Mn-doped samples<sup>47</sup> the C-A transition was identified. In this experiment we showed the presence of D-A type emissions, and the appearance of a new emission following the quenching of the D-A type emission and with lower excitation intensities.

Analogous to the explanations for the shallow acceptors and Mn-doped GaAs<sup>47</sup>, the new emission appears to be a C-A transition involving a Mn acceptor. The origin of the ~1.40 eV emission in the hydrogen-atmosphere heat-treated sample was thought to be due to the Si-V<sub>As</sub> complex. However, the temperature dependence in both experiments appears to be the same. We also have done a hydrogen-atmosphere heat-treatment study at 700-900°C for 20 min without any encapsulation on the samples. The ~1.40-eV emission originates from the near surface of the heat-treated sample. We have found a one-to-one correspondence between the ~1.40 eV emission bands for the samples heat treated under a hydrogen atmosphere, and those implanted with Mn; when the samples for the two experiments are from the same substrate, the emission shape and the temperature dependence of the emission characteristics are the same. This indicates that the ~1.40-eV emissions obtained from the hydrogen-atmosphere heat-treated, and from the implanted samples, have the same origin. Therefore, it can be thought that the hydrogen-atmosphere heat-treated samples are contaminated with Mn from unknown sources during the heat-treatment process. The observation of the ~1.40 eV emission in the Si<sub>3</sub>N<sub>4</sub>-capped control samples can also be explained by this contamination. However, we feel that further studies such as EPR measurements and chemical identifications are needed.

Known experiments for Mn-doped samples under stress<sup>49</sup> and EPR measurements show the presence of both cubic symmetry Mn, and complex centers such as Mn-Li and Mn-V<sub>As</sub>. Therefore, the emissions dominant at higher temperatures in our experiment can be explained as C-A transitions or intracenter transitions in complex centers, depending on the symmetry of the center responsible for the emissions at higher temperature.

#### 5.4 Conclusions

Mn implantation has been employed to investigate the radiative mechanism of the ~1.40-eV emission present in as-grown and heat-treated GaAs. The implantation provided an excellent way of controlling the concentration of deep-center Mn. The changes in substrate materials, excitation intensity, and temperature showed the presence of the ~1.40-eV emission in a wide range and led to an understanding of the radiative mechanism. Preliminary studies showed that the 1.40-eV emissions from the hydrogen-atmosphere heat-treated, and from the Mn-implanted samples, originate from the same center

## 6.0 ION IMPLANTED LAYERS IN GaAs

### 6.1 Introduction

The importance of ion implantation is a widely-known fact. Photoluminescence properties due to p-type dopants such as Mg, Be, Cd, and Zn were investigated with respect to changes in temperature, substrate, and excitation intensity. Also, an amphoteric dopant Ge was studied with an emphasis on deep-center characteristics. Below we describe the results of Mg, Be, Zn, Ge, and Cd-implanted layer studies.

### 6.2 Excitation-Dependent Emission in Mg-, Be-, Cd-, and Zn-Implanted GaAs.

The following is an abstract reprinted from Ref. 20.

The low-temperature properties of the excitation-dependent (moving) emissions in Mg-, Be-, Cd-, and Zn-implanted GaAs layers are investigated with respect to changes in temperature and excitation intensity. The substrates used were epitaxial layers, melt-grown n-type crystals, and Cr-doped semi-insulating crystals. Donor concentrations of the n-type substrates were in the range  $5 \times 10^{13}$  to  $2 \times 10^{18}$  electrons  $\text{cm}^{-3}$ . Models explaining a large energy shift are presented for both Cr-doped and n-type substrates. The moving emissions are classified into three different cases: (a) donor-acceptor-pair emissions in relatively pure weakly compensated crystals; (b) donor-acceptor-pair emission in impure strongly compensated crystals; and (c) a radiation transition from the conduction-band tails to the valence band. The donor-acceptor-pair emission in the impure compensated crystals shows the shift to lower energy with an increase of temperature in the temperature range 4-50°K, while the donor-acceptor-pair emission in pure crystals behaves in the usual manner. This is due to the increase in the random impurity potential. The large shift of emission peaks originates in the impure compensated regions, i.e., the near-surface region due to the out-diffusion of the implanted atoms in Cr-doped substrates, and the highly resistive layer between the p- and n-type region in n-type substrates. Additional compensating donors are found

to be defect-type donors, As vacancies. The formation of As vacancies differs depending on the substrate materials. The role of the As vacancy in forming a compensated region is discussed.

### 6.3 Experimental Results

In Fig. 6-1, the excitation intensity  $I_{ex}$  is plotted as a function of the emission-peak energy  $E_p$  of the moving band for nine samples. In general,  $I_{ex}$  has an exponential relationship with  $E_p$ , namely,

$$I_{ex} = I_0 \exp(E_p/\beta),$$

where  $\beta$  is the coefficient which represents the energy shift (an energy-shift constant). Table 6-1 contains the crystal parameters of the substrates, the implantation doses, annealing temperatures, the energy-shift constants, and half-widths of the emission band for the samples shown in Fig. 6-1. It is clear that the energy-shift constant and the half-width increase with the electron concentration of the substrate. The observed energy change per decade of the excitation intensity ranges from 0.7 to 15 meV.

### 6.4 Model

When only one type of impurity (donor or acceptor) is present in a semiconductor, the Mott transition takes place at a concentration given by

$$N_M^{1/3} a_B \approx 0.25, \quad (6-1)$$

where  $N_M$  is the concentration for the Mott transition and  $a_B$  is the Bohr radius of the impurity. Generally, we can define crystals as relatively "pure" or "impure" by comparing the impurity concentration with that for the Mott transition. When donors and acceptors are present simultaneously, the Mott transition will be relaxed. In impure compensated crystals, inversely charged impurity atoms and fluctuations in the concentration create irregular fluctuations of the electrostatic potential with position. This random impurity potential perturbs the energies of band states of impure crystals and also changes the well-defined energy level into broad band states.

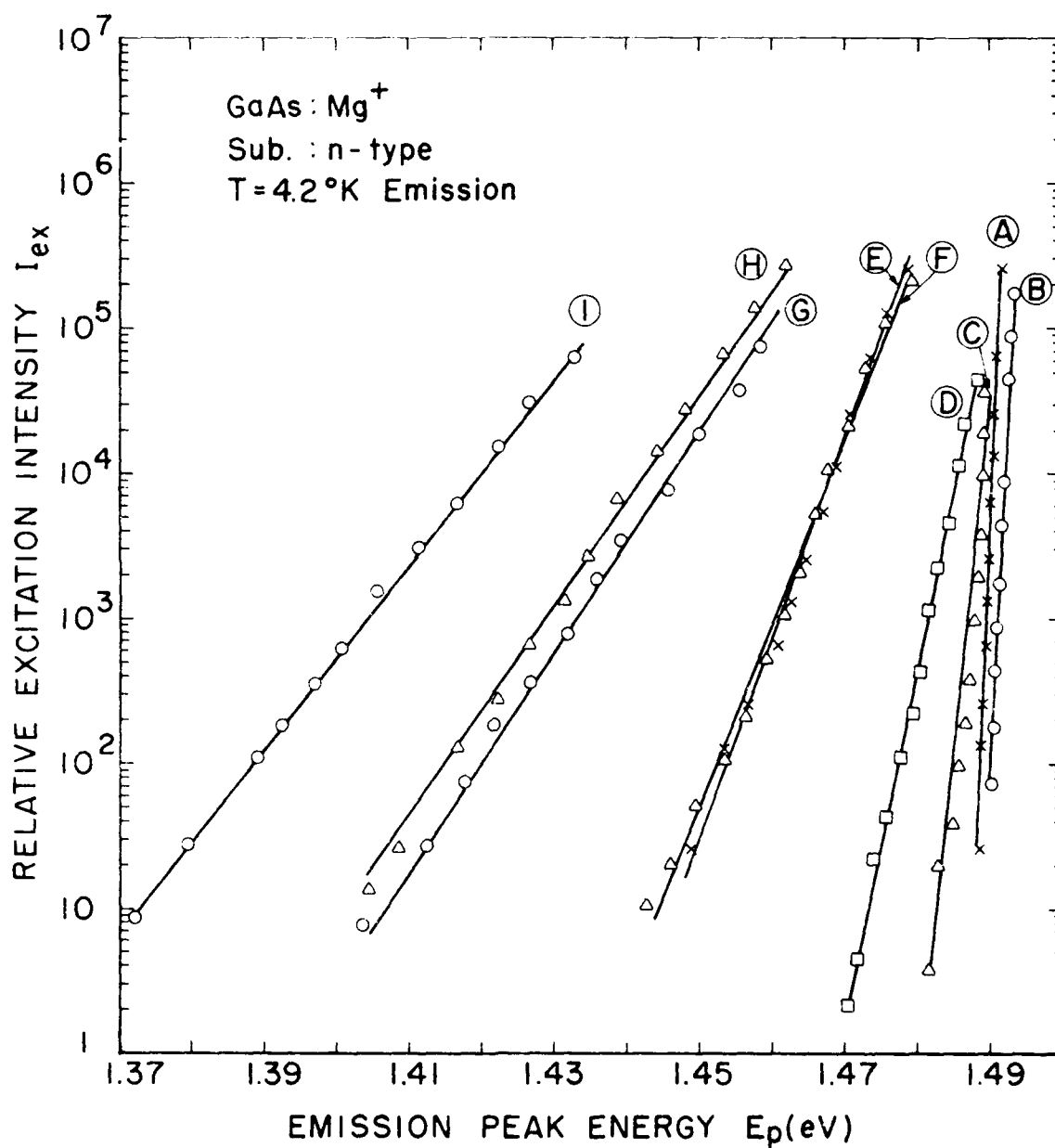


Fig. 6-1. Excitation-intensity-vs-emission-peak-energy relation obtained for Mg-implanted layers with different n-type substrates.

Table 6-1. Details for the moving emissions given in Fig. 6-1. All the emissions were obtained with Mg implantation

Sample No.	Substrate No.	Energy-shift		Half-width <sup>a</sup> (meV)	Dose $\phi$ (cm <sup>-2</sup> )	Annealing		Encapsulation
		Carrier conc. n (cm <sup>-3</sup> )	const. E (meV)			Temp. T <sub>0</sub> (°C)	T <sub>A</sub>	
A	1	$5.1 \times 10^{13}$	0.30	6.3	$5 \times 10^{12}$	800		SiO <sub>2</sub>
B	3	$1.4 \times 10^{15}$	0.45	6.3	$5 \times 10^{12}$	800		SiO <sub>2</sub>
C	4	$1.9 \times 10^{16}$	1.0	6.3	$1 \times 10^{13}$	800		SiO <sub>2</sub>
D	8	$3.6 \times 10^{15}$	1.9	11	$1 \times 10^{13}$	900		SiO <sub>2</sub>
E	12	$4.2 \times 10^{16}$	3.2	16	$5 \times 10^{12}$	800		SiO <sub>2</sub>
F	13	$6.5 \times 10^{16}$	3.4	16	$5 \times 10^{12}$	900		Si <sub>3</sub> N <sub>4</sub>
G	14	$4.0 \times 10^{17}$	5.3	33	$5 \times 10^{12}$	900		SiO <sub>2</sub>
H	15	$8.0 \times 10^{17}$	5.7	38	$1 \times 10^{13}$	900		SiO <sub>2</sub>
I	16	$2.0 \times 10^{18}$	6.4	38	$1 \times 10^{13}$	800		Si <sub>3</sub> O <sub>4</sub>

<sup>a</sup> Average value.



The average depth of potential can be given<sup>50</sup> by

$$V = 2\pi^{1/2} (e^2 / \epsilon r_0) (Nr_0^3)^{1/2}, \quad (6-2)$$

where  $\epsilon$  is the dielectric constant,  $r_0$  is the screening radius, and  $N$  is the total concentration of ionized donors and acceptors. Since the acceptor concentration is fixed in our experiment, an increase of the total number of donors would increase the total number of ionized impurities and, consequently, the screening length, due to the reduction of free carriers. Therefore, the potential depth increases.

With these considerations we can construct a model for D-A transitions for our samples as shown in Figures 6-2(a) and 6-2(b). Figures 6-2(a) and 6-2(b) represent the radiative recombination mechanisms of D-A emission in the relatively pure weakly compensated crystals and in the impure strongly compensated crystals, respectively. With a further increase of effective-mass donors, localized states associated with donors lose their original discrete characteristics and merge with the conduction band. Then, a radiative transition connecting the valence band and the conduction-band tail dominates, as shown in Fig. 6-2(c).

The donor-acceptor-pair-energy relation in the relatively pure uncompensated crystals is given by

$$h\nu = E_g - (E_d + E_a) + e^2 / \epsilon r, \quad (6-3)$$

where all the symbols have their usual meanings. In this case, the random impurity potential  $V$  is expected to be small compared to  $kT$ , and the perturbing of the energy band can be neglected. Increasing the excitation intensity favors the close pairs, and the emission energy moves to higher energies, according to Eq. 6-3. In the relatively pure uncompensated GaAs, the energy shift was found to be  $\leq 1$  meV per decade of the excitation intensity. However, a substantial shift of emission energy was observed in impure samples.

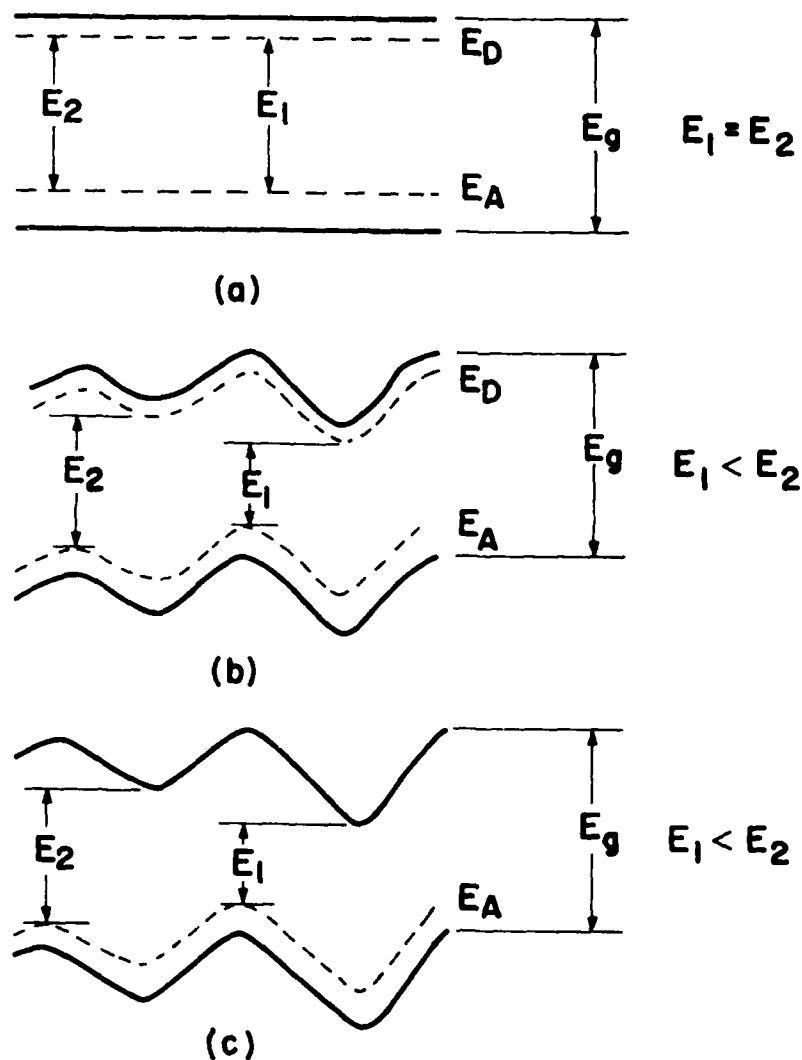


Fig. 6-2. Donor-acceptor-pair emission; (a) in the pure weakly compensated crystal and (b) the impure strongly compensated crystal. With an increase of the effective-mass donors, the donor level merges with the conduction band, and transitions connecting the valence band and the conduction-band tail dominate, as shown in (c).

The potential depth  $\Gamma$  increases with the impurity concentration and compensation. The energies of the conduction-valence band are distorted by the random potential as shown in Fig. 6-2(b). Electrons and holes originate in a range of states depending on the local potential. The nonequilibrium carriers localized in the potential wells near the generation participate in the radiative recombination through donors and acceptors. The radiative transition is thought to be due to tunneling. The emitted photon energy can be given by

$$E \approx E_g - (E_d + E_a) - 2\Gamma.$$

The potential depth  $\Gamma$  will be proportional to the energy-shift constant  $\beta$ .

An important feature of the situation illustrated in Fig. 6-2(b) is the fact that the capture probabilities of nonequilibrium carriers at the impurities are not uniform over the conduction and valence bands. This indicates that the energy distribution of carriers cannot be defined by introducing a single quasi-Fermi level of the impurity state, as demonstrated in a transition involving tail states occupied by nonequilibrium carriers in GaAs by the rise- and decay-time measurements.<sup>51</sup> The capture probability of the excess carriers at the impurity center is smaller in the deeper potential at lower temperatures. With an increase of temperature, the situation relaxes with the eventual establishment of a single quasi-Fermi level. Therefore, the photon energy obtained with a constant excitation shifts to lower energies with an increase of temperature. However, the temperature dependence of the emission intensity should be the same as expected for the D-A emission in the relatively pure uncompensated crystal. We call the D-A transition in the impure strongly compensated crystals "quasi-donor-acceptor-pair emission (Q-D-A)." The emission energy of the Q-D-A emission shifts to lower energies proportional to the random potential  $\Gamma$ , while the D-A emission in pure uncompensated crystals moves to higher energies with an increase of temperature.

### 6.5 Deep Emission Centers in Ge-Implanted GaAs

The abstract of Ref. 52 is reprinted as follows.

Photoluminescence emission spectra from Ge-implanted layers in GaAs were studied with respect to changes of exciting wavelength, excitation intensity, temperature, and the depth of the implanted layers. Deeper emissions are dominant in the near-surface region because vacancies and their complexes with Ge play important roles in the radiative processes. Emission due to a donor-acceptor pair transition involving the Ge acceptor is present in all Ge-implanted layers. The binding energy of the Ge acceptor is estimated to be  $40 \pm 3$  meV from the temperature dependence of the emission due to conduction-band-to-Ge-acceptor transitions. High-temperature annealing at  $900$ - $950^\circ\text{C}$  with a  $\text{Si}_3\text{N}_4$  cap is needed to increase the Ge activation which produces p-type conduction.

Figure 6-3, curves (a)-(f) show the typical 325-nm-line emission spectrum obtained from Ge-implanted and control samples which were annealed at  $800^\circ\text{C}$ . The control (unimplanted) sample shows two emission bands at 1.514 and 1.488 eV. The dominant emission at 1.488 eV can be ascribed to the presence of a Si acceptor in the substrate. The weaker band at 1.514 eV is presumably due to several unresolved excitons and valence-band-to-donor transitions. Emissions in Ge-implanted layers of Fig. 6-3, curves (b)-(f) can be characterized by lower-energy bands A-E. The dominant emission band shifts to a lower energy with an increase of dose. The fact that the emissions are related to Ge was confirmed by the lack of such emissions from layers implanted with Kr and subsequently annealed at  $800^\circ\text{C}$ . (The Kr implantation was performed at 120 keV for doses of  $5 \times 10^{12}$  to  $3 \times 10^{14} \text{ cm}^{-2}$ ). The explanation of the emission bands in Fig. 6-3 are summarized in Table 6-2.

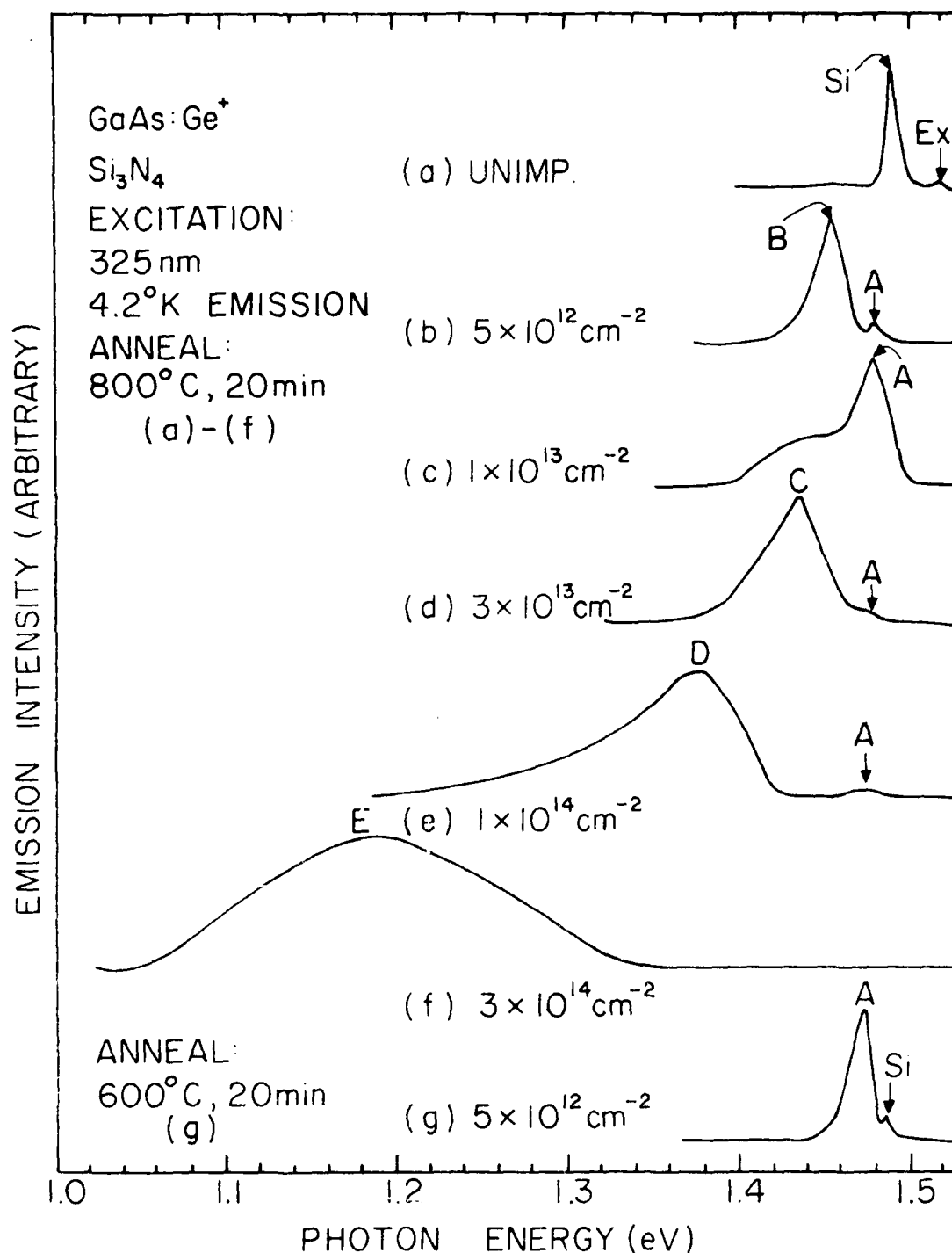


Fig. 6-3. Emission spectra obtained from GaAs layers implanted with Ge to doses of  $5 \times 10^{12}$  to  $3 \times 10^{14} \text{ cm}^{-2}$  with Si<sub>3</sub>N<sub>4</sub> encapsulation. In curves (a)-(f), the layers were annealed to 800°C and in curve (g) at 600°C. Excitation intensity is 10 mW from the 325-nm line of a He-Cd laser.

Table 6-2. Emission bands in Ge implanted layers.

Band	Energy (eV)	Explanation
Ex	1.514	Unresolved excitons
Si	1.488	Si-related
A	~1.47	Donor - Ge <sub>As</sub> pair (ordinary)
B	~1.45	Donor - Ge <sub>As</sub> pair modified by random impurity potential
C	1.435	V <sub>As</sub> - Ge <sub>As</sub> complex
D	~1.36	Ge <sub>Ga</sub> - deep acceptor pair transition
E	1.18	Ge <sub>Ga</sub> - V <sub>Ga</sub>

## 7.0 EMISSION CHARACTERISTICS OF SEMI-INSULATING GaAs

### 7.1 Introduction

The characterization of semi-insulating material is necessary for understanding the origin of compensation mechanisms. Cr is usually used as a dopant to obtain a high resistivity. Therefore, the deep-center photoluminescence in Cr-doped GaAs has been the subject of numerous investigations. A broad emission band at  $\sim 0.8$  eV has been reported by several authors. A sharp no-phonon line at 0.839 eV with a broad side-band at  $\sim 0.80$  eV has been observed<sup>42</sup> at low temperatures and has been attributed either to the  $^5E-^5T_2$  internal transition<sup>53</sup> of  $Cr^{2+}$  or to transition<sup>42</sup> of an electron in the conduction band to the  $^5T_2$  level of  $Cr^{2+}$ . A band of  $\sim 0.56-0.63$  eV has also been observed by many workers. They associated the band with the presence of Cr. Recent high resolution cathodoluminescence measurements<sup>54</sup> showed that the line at 0.839 eV consisted of many components and that there were three no-phonon components at 0.574 eV. The photoluminescence measurements<sup>55</sup> of GaAs over a wide range of Cr- and Si-concentrations showed that the 0.839 eV line was associated with an internal  $^5E-^5T_2$  transition of  $Cr^{2+}$  and the 0.839 eV line disappeared due to the conversion to  $Cr^{1+}$  state of all the Cr in sufficiently n-type materials. Also, the independence of Al composition of the  $Cr^{2+}$  band at 0.8 eV in  $Al_xGa_{1-x}As:Cr$  showed<sup>56</sup> that this band at 0.8 eV originates from the internal  $^5E-^5T_2$  transition of  $Cr^{2+}$ . However, the origin of the 0.839-eV emission was recently attributed to Cr-donor complexes by White.<sup>57</sup> In our work, we have showed that Cr-doped samples were contaminated by oxygen. Therefore, the contribution of the oxygen-related level to the compensation mechanism is important.

## 7.2 Results

The room-temperature resistivities of the Cr- and O-doped materials were  $4.7 \times 10^7 - 1.1 \times 10^9 \Omega\text{cm}$  with apparent electron mobilities of  $2500-5700 \text{ cm}^2\text{V}^{-1}\text{sec}^{-1}$ . Photoluminescence measurements were made at  $T = 4.2 \text{ K}$  by immersing samples in liquid helium or at  $T = 5 - 320 \text{ K}$  by using a Heli-tran variable temperature dewar. A Kr-laser operating at  $6471 \text{ \AA}$  with a maximum intensity of  $5 \text{ W cm}^{-2}$  was used as a source of excitation. The emission spectra were analyzed by a  $3/4 \text{ m}$  spectrometer with a  $600 \text{ grooves mm}^{-1}$  grating blazed at  $1.24 \text{ }\mu\text{m}$  or a  $300 \text{ grooves mm}^{-1}$  grating blazed at  $1.7 \text{ }\mu\text{m}$  and were detected by a liquid-nitrogen cooled PbS cell. All the spectra were calibrated for the spectral sensitivity of the detecting system.

Typical 4.2 K-emission spectra obtained from various samples can be summarized as shown in Fig. 7-1. The curve (a) of Fig. 7-1 shows a broad-band emission at about  $0.62 \text{ eV}$  obtained from an O-doped sample. The peak energy of this band shifts to  $0.68 \text{ eV}$  as  $T$  is raised to  $40 \text{ K}$ , and remains at the same energy for  $T = 40 - 260 \text{ K}$ . The emission band, we believe, is the same as that observed by Turner et al.<sup>58</sup> and attributed to the presence of O. From the temperature dependence of the half-width of this band we find that the center responsible for the emission is not likely to be a simple substitutional center.

Curve (d) of Fig. 7-1 shows an emission spectrum obtained from a Cr-doped sample. The sharp no-phonon line at  $0.839 \text{ eV}$  and its phonon satellites, and two no-phonon lines at  $\sim 0.574 \text{ eV}$  appear with the subsequent structureless lower-energy band. The spectra in curves (b) and (c) are also obtained from Cr-doped samples. A broad band at  $\sim 0.62 \text{ eV}$  is present with the Cr-emission at  $\sim 0.81 \text{ eV}$ . No-phonon lines at  $\sim 0.574 \text{ eV}$  are seen in the curve (c) but not in the curve (b).



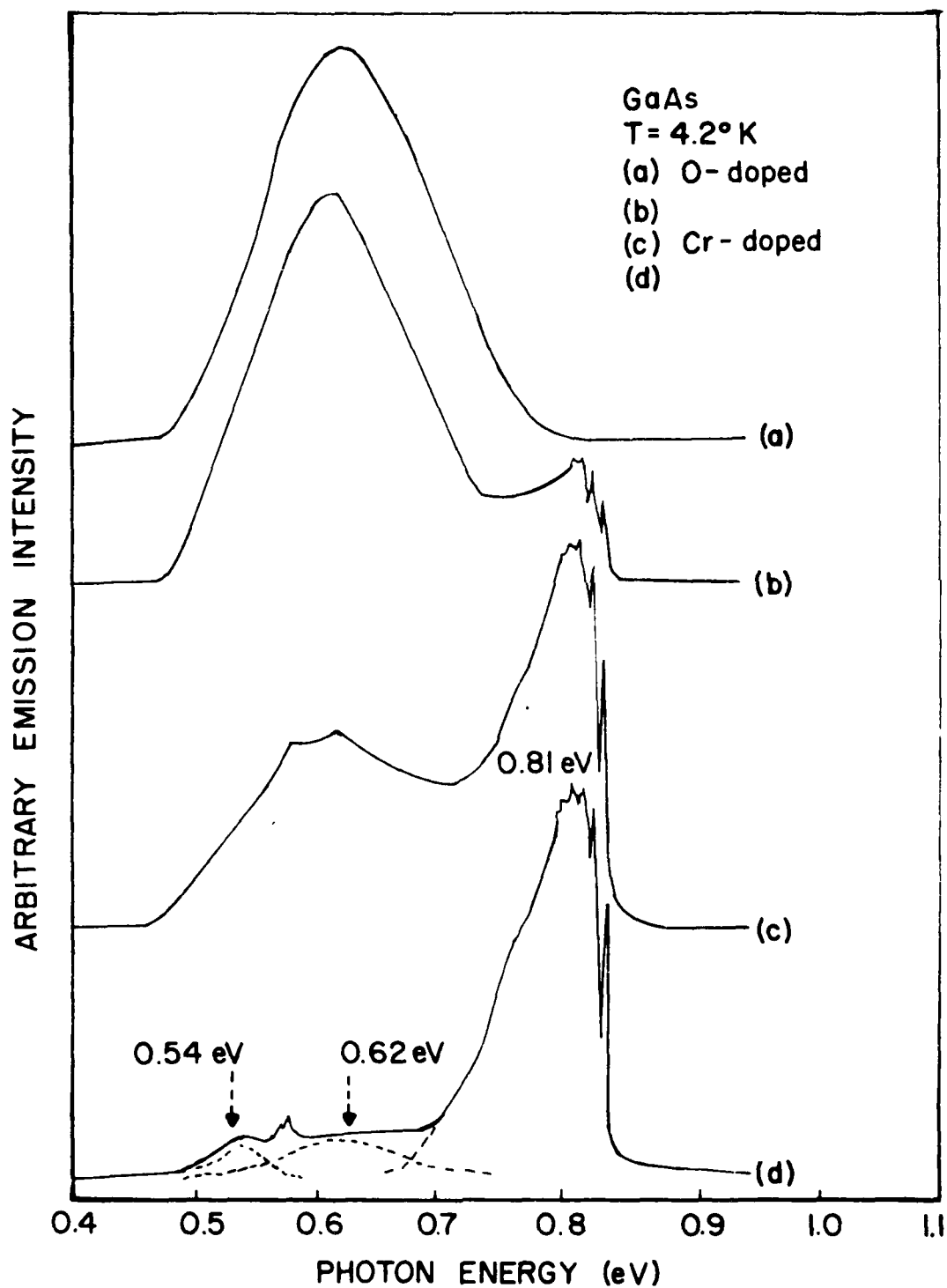


Fig. 7-1. Photoluminescence spectra of Cr- and O-doped semi-insulating GaAs at  $T = 4.2$  K. Curve (a) and curves (b)-(d) were obtained, respectively, from O-doped and Cr-doped crystals. The dashed line in the curve (d) shows three bands at 0.81, 0.62, and 0.54 eV. All the spectra are normalized.

This is the reason why Koschel et al.<sup>53</sup> could not observe sharp no-phonon lines. We believe that the emission characteristics of Cr-doped semi-insulating crystals can be represented by the curves (b)-(d) of Fig. 7-1. The relative emission intensity ratio between the band at 0.62 eV and the Cr band at ~0.81 eV varies approximately from 25 to 0.1 for about 100 samples. The broad band at 0.62 eV in Cr-doped samples was studied as a function of temperature. The temperature-dependent emission characteristics are the same as those of the band in O-doped samples. Therefore, the band in Cr-doped crystals can be attributed to the presence of O during the crystal growth process. We believe that the bands at ~0.59 eV in Deveaud and Favenec's work<sup>59</sup> are probably due to O.

Figure 7-2 shows the relative emission intensity of the Cr band at 0.81 eV as a function of temperature for samples having different values of  $I_O/I_{Cr}$ . Curve (a) shows the intensity vs  $10^3 T^{-1}$  relationship for samples with  $I_O/I_{Cr} \leq 0.1$ . This is a typical temperature variation for samples which are less influenced by the presence of O. A sharp decrease of the emission intensity is seen at  $T > 200K$ . The curves (b) and (c) represent typical temperature-dependent characteristics of the samples with  $\sim 4 \geq I_O/I_{Cr} > 0.1$ . The enhancement of the emission intensity is clearly observed at  $T = \sim 100$  and  $200K$  from the temperature dependence in the region  $T = 70 - 200K$ . There is also a sharp drop of the emission intensity at  $T > 200K$  as in the curve (a). The enhancement of the emission intensity can be explained as follows. We assume that  $Cr^{3+}$  state changes into  $Cr^{2+}$  by capturing an electron and that this center is responsible for the 0.81 eV emission. The electrons trapped at the trapping centers present with O-doping are relocated at Cr-centers with an increase of temperature. Therefore the enhancement appeared for O-doped samples only. With a further increase of O, the Cr-emission drastically quenches down at  $T < 200K$  as shown in curves (d) and (e). This is true for

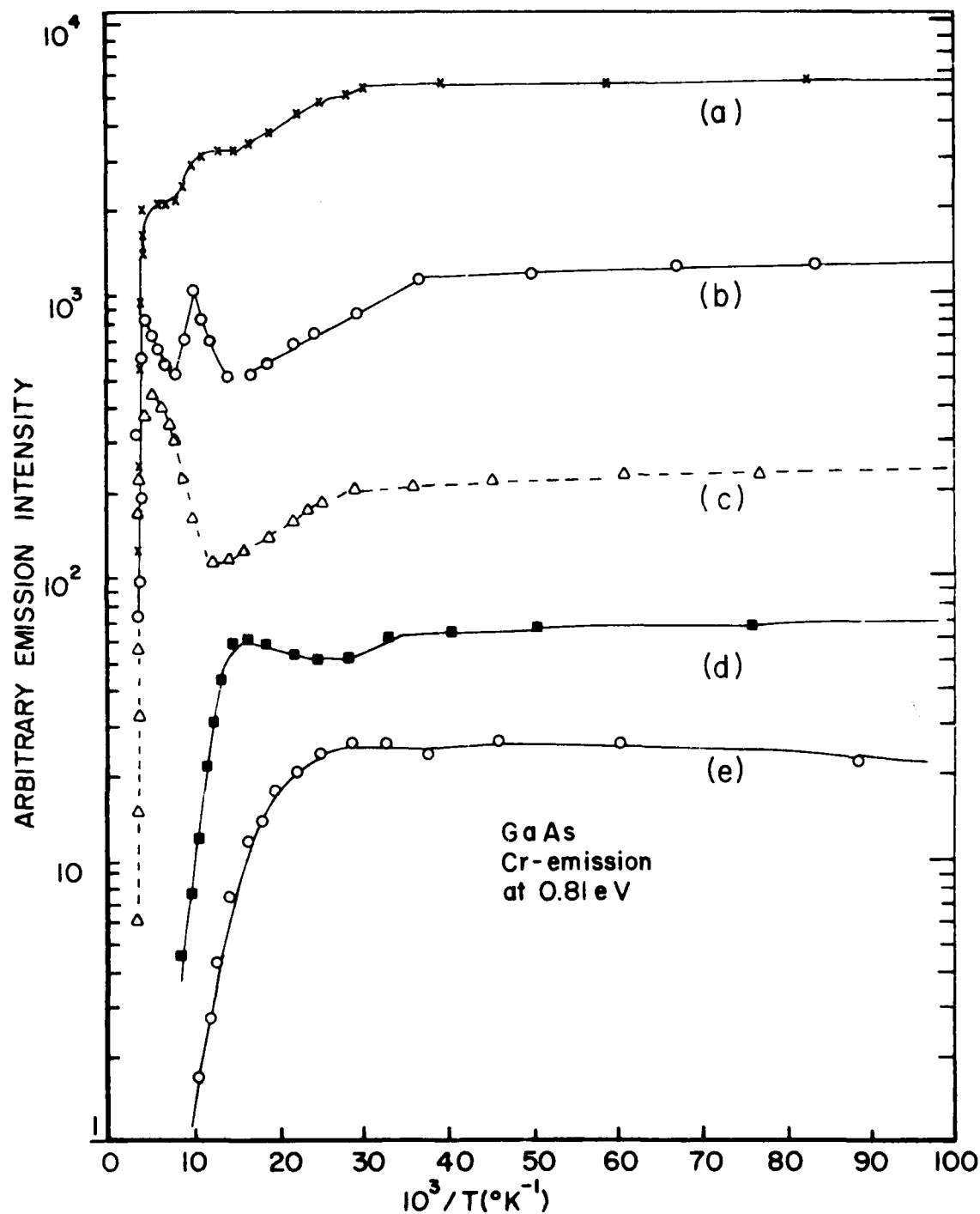


Fig. 7-2. The relative emission intensity of the broad Cr emission at 0.81 eV vs  $10^3/T$  for (a)  $I_0/I_{Cr} \leq 0.1$ , (b) and (c)  $4 \geq I_0/I_{Cr} \geq 0.1$ , and (d) and (e)  $I_0/I_{Cr} \rightarrow 4$ . Here,  $I_0/I_{Cr}$  is the emission intensity ratio of the O-band, and the Cr-band at 0.81 eV.

the samples having  $I_0/I_{Cr} > 4$ . The quenching is due to the dominance of O which has a large nonradiative electron capture cross section, as shown by Lang and Logan.<sup>60</sup>

### 7.3 Conclusions

We have shown by the photoluminescence method that most of Cr-doped semi-insulating crystals are also doped with O. The characteristics of the 0.53 eV band were clarified by using the quenching behavior of the O-emission as a function of temperature. This leads to an explanation of the Cr emission at  $\sim 0.81$  and 0.54 eV in terms of a static Jahn-Teller distortion in the ground state of  $Cr^{2+}$ . Also, the temperature dependence of the Cr-emission intensity was found to drastically change depending on the relative concentration of Cr and O.

## 8.0 PHOTOLUMINESCENCE CHARACTERIZATION OF BULK InP CRYSTALS

### 8.1 Introduction

Indium phosphide has recently received growing interest because of applications in microwave and optical devices. However, it has not received a systematic impurity and defect characterization study like GaAs and GaP. By using the photoluminescence and photoconductivity methods, we have characterized both shallow and deep centers. Particularly, we have explained the nature of the 1.10 eV emission band and have found a correlation between PL and PC data for the 1.10 eV energy level. The origin of the emission band was previously ascribed to a P vacancy<sup>61</sup> or Cu<sup>62</sup>.

### 8.2 Results and Analysis

Figure 8-1 shows the 4.2K emission spectra near 1.10 eV obtained from four different samples. Room-temperature electron concentration and crystal growth parameters of the crystals are given in Table 8-1. The emission characteristics of the band are the same for a given sample without regard to the sample size or thickness. In addition to the emission at ~1.10 eV, these crystals typically show the near-bandedge emissions at ~1.416 and 1.38 eV which can be ascribed to exciton complexes and donor-acceptor pairs, respectively. The relative intensity ratio of the 1.416 eV emission to the 1.10 eV emission,  $I_{1.416}/I_{1.10}$  ranges from 0.1 to 60 at 4.2K with an excitation intensity of ~100 mW. The ratios are usually small for high-resistivity bulk materials doped with Fe while undoped conducting bulk materials show larger values. However, the near-bandedge emissions are not our concern here. We find the following characteristics of the 1.10 eV bands from our experiment; (1) the emission has phonon structure at 4.2 K in contrast to a broad structureless band observed previously, (2) the peak position ranges from 1.15 to 1.06 eV, (3) the band shape becomes more symmetrical with the shift of the peak position to a lower energy.

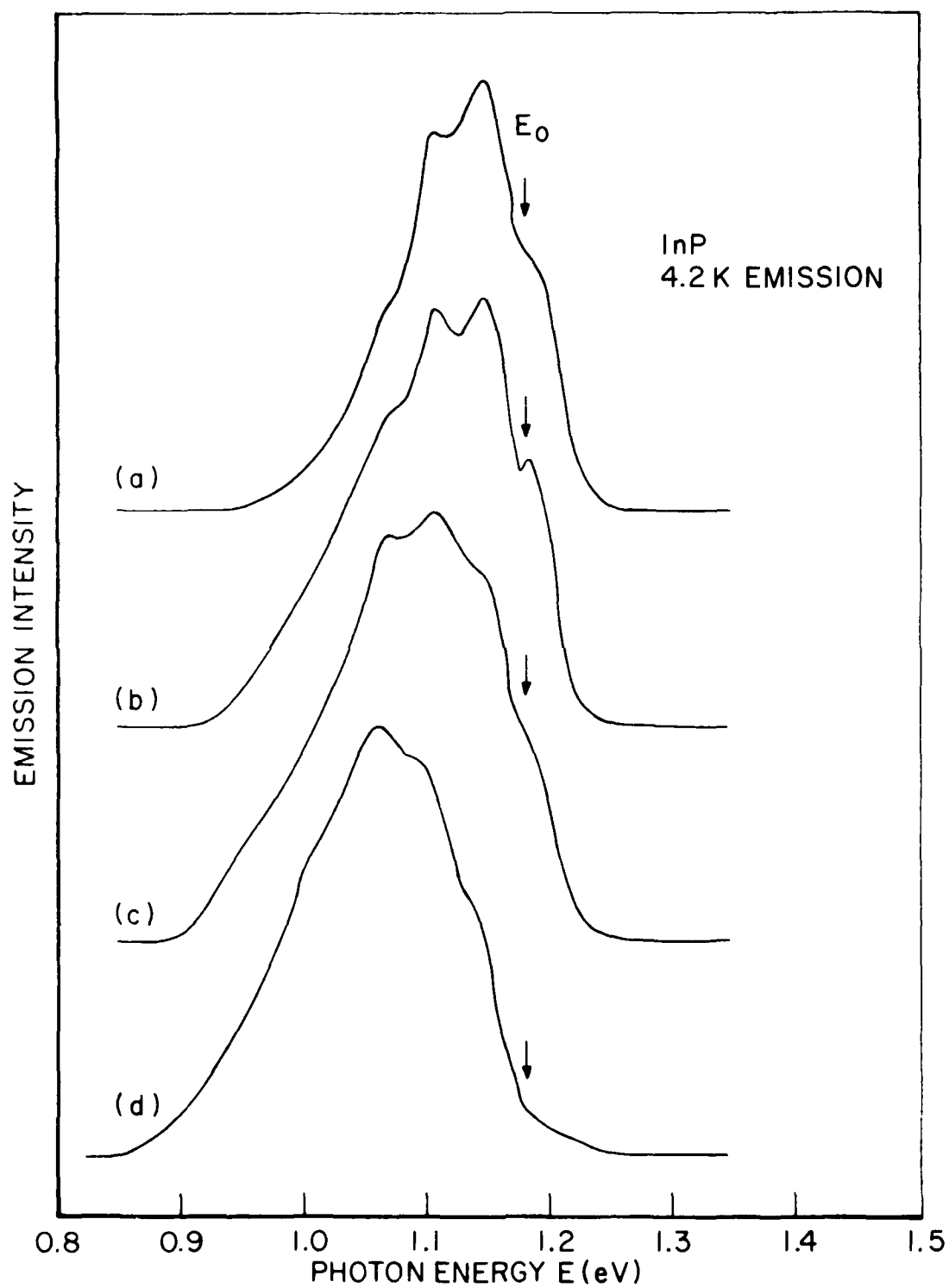


Fig. 8-1. The  $\sim 1.10$  eV emission band at 4.2 K obtained from four InP crystals. The peak position does not change with the excitation intensity. The peak position depends on the sample. The details of samples used are given in Table 1.  $E_0$ , the zero-phonon energy at 1.18 eV is indicated by arrows.

Table 8-1. Room temperature carrier concentration, crystal growth process and the coupling strength  $S$  for the samples shown in Fig. 8-1.

Sample number	Electron concentration $n(\text{cm}^{-3})$	Growth process	Coupling strength $S$
a	$5.1 \times 10^{15}$	Epi, undoped	1.7
b	$2.0 \times 10^{15}$	Bulk, undoped	1.9
c	$4.4 \times 10^{15}$	Bulk, undoped	2.8
c	$2.0 \times 10^8$	Bulk, Fe-doped	3.5

In order to explain the emission characteristics of the band at 1.10 eV we use a theoretical model in which two nondegenerate electronic states at the localized center are assumed to couple linearly to a single normal coordinate of the lattice. In the adiabatic approximation, the initial- and final-state potentials, respectively, are given by

$$E_b(q) = E_{ab} + am\hbar w(mw/\hbar)^{1/2}q + \frac{1}{2}mw^2q^2$$

$$E_a(q) = \frac{1}{2}mw^2q^2$$

where  $q$ ,  $m$ , and  $w$  are the normal coordinate, mass, and the coupled phonon frequency, respectively,  $E_{ab}$  is the energy separation between the two states at  $q = 0$ , and  $a$  is a measure of strength of the interaction. The curve (a) of Fig. 8-2 shows the schematics of  $E_a$  and  $E_b$ . The vibrational states  $\beta$  and  $\alpha$  in the initial and final states are also given. At  $T = 0K$ , the only occupied initial state is  $\beta = 0$ . Then the position of the  $n$ th phonon side band is given by

$$E_{0n} = E_0 - n\hbar w,$$

where  $E_0$  is the zero-phonon energy. The transition probability of the  $n$ th phonon side band is given by

$$I_{0n} = \exp(-S) \cdot S^n / n!,$$

where  $S(=a^2/2 = \Delta^2mw/2\hbar)$  is a coupling strength parameter of the localized center-phonon interaction.  $\Delta$  is the displacement in configuration coordinate space as shown in the curve (a) of Fig. 8-2. With the above model, we found out that the coupling constant ranged from 1.7 to 3.5 as shown in Table 8-1.

Figures 8-3 and 8-4 show, respectively, dc and ac photoconductivity spectra obtained from an Fe-doped high-resistivity InP sample at  $T = 7, 90, 223$  and  $300$  K. The ac method was necessary to find signals much weaker than the dark conductivity. The ac and dc photoconductivity spectra at  $7$  K show an initial onset of the photoresponse at  $\sim 0.60$  eV, a maximum near  $0.78$  eV, and a subsequent quenching of the photoresponse at higher energies than  $0.78$  eV. Another strong photoconductive onset occurs at  $1.1$ - $1.2$  eV with a continuous



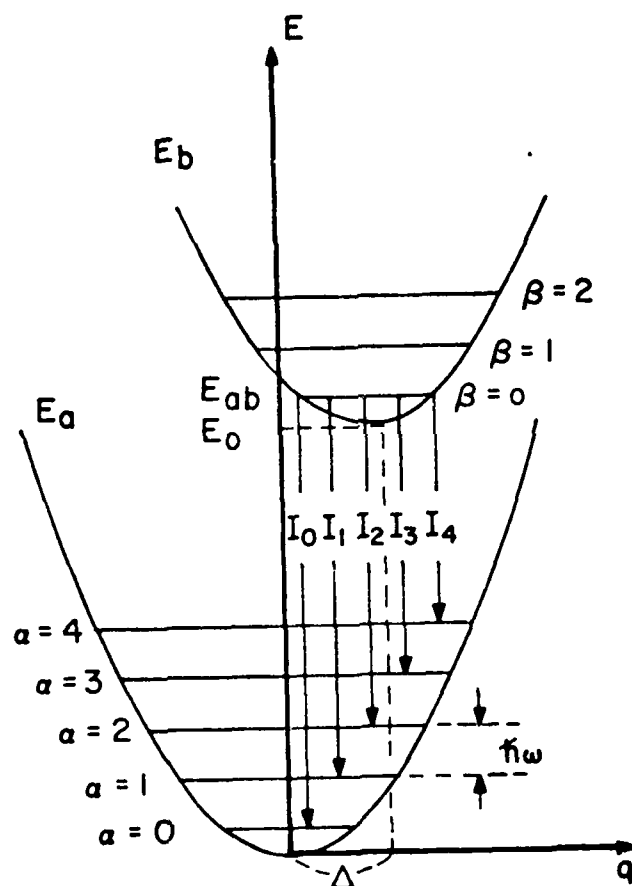


Fig. 8-2. Schematic energy diagram on vibrational transitions for a linear coupling to a single normal coordinate of the lattice at  $T = 0\text{K}$ . The vertical arrows indicate the emission transitions involving the vibrational levels in the final state from the lowest initial state.

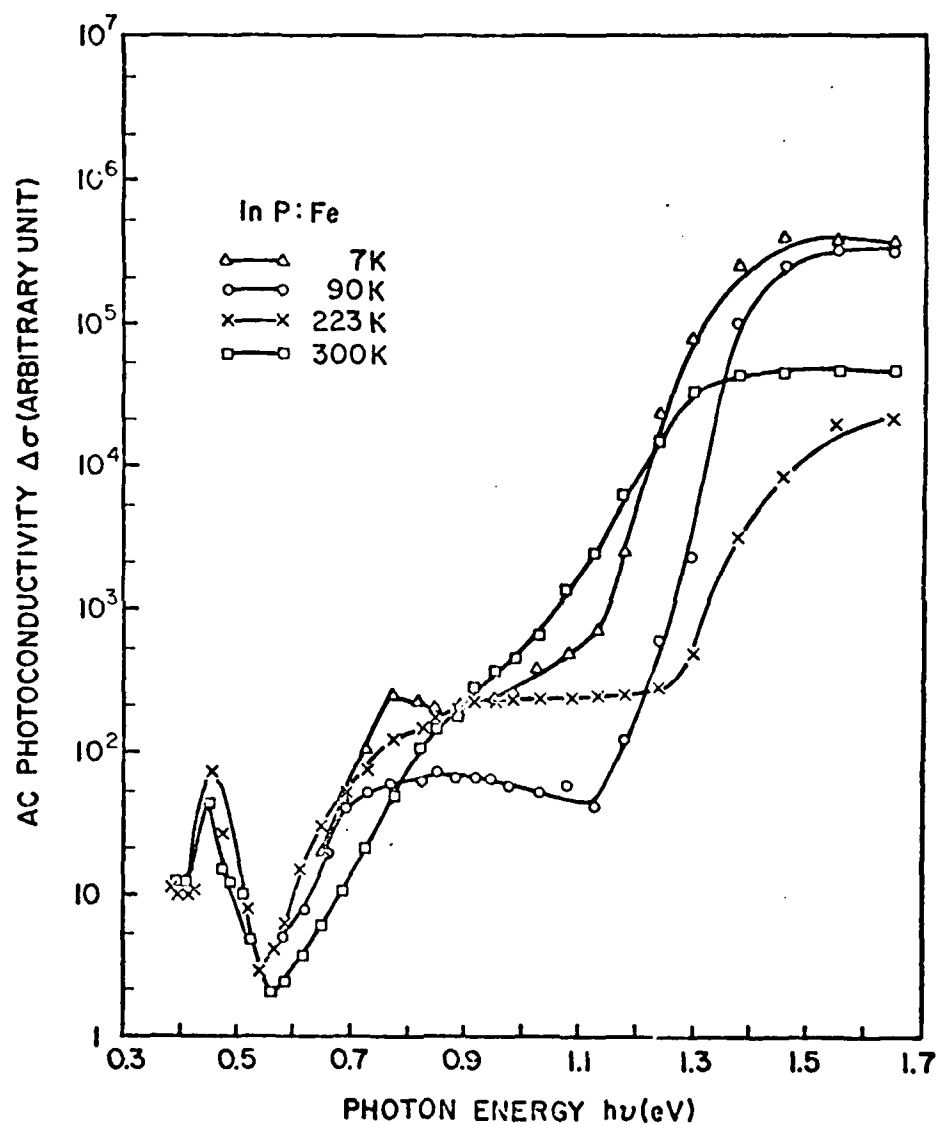


Fig. 8-3. AC photoconductivity ( $\Delta\sigma$ ) spectra obtained at  $T = 7, 90, 223$  and  $300$  K obtained from an Fe-doped high-resistivity sample.

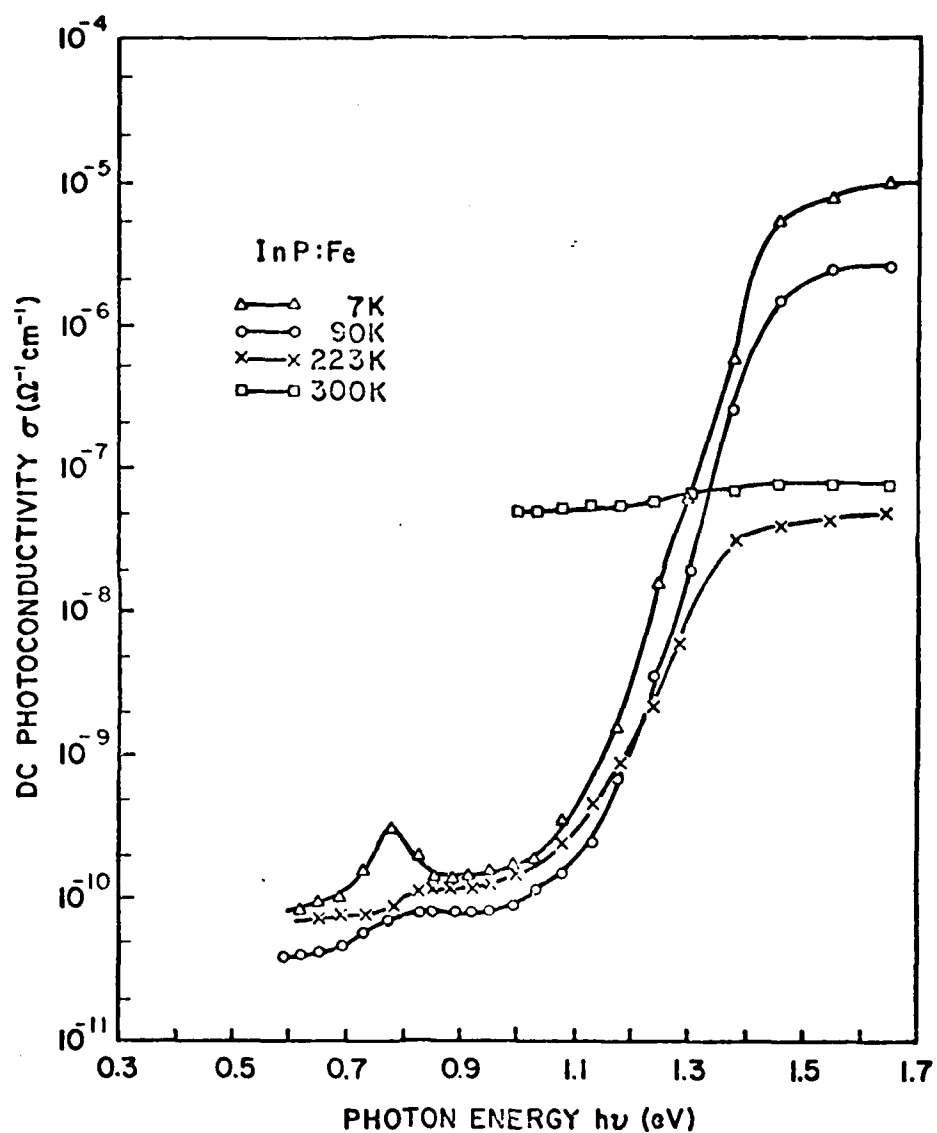


Fig. 8-4. DC photoconductivity ( $\sigma$ ) spectra obtained at  $T = 7, 90, 223$  and  $300$  K obtained from an Fe-doped high-resistivity sample.

increase of photon energy before the bandgap region is reached. At  $T > 7$  K, the characteristics of the ac and dc photoconductivity spectra can be described as follows: 1) the PC maximum present at 7 K disappears; 2) the PC response has an onset near 0.60 eV, increases up to 0.8 eV, has a weaker onset near 0.8 eV, changes little at  $0.8 < h\nu < 1.1$  eV, and shows a strong onset at 1.1 - 1.2 eV. Especially, the ac spectra at  $T = 223$  and 300 K show a broad band peaking at 0.44 eV in the energy range of 0.38 - 0.60 eV.

The 0.60 eV onset can be taken to result from the transition of  $\text{Fe}^{2+}(^5\text{E}) \rightarrow$  the conduction band. Fung et. al.<sup>63</sup> ascribed the PC maximum at 0.78 eV and the subsequent quenching effect to the strong reduction in lifetime of the photoexcited carriers when the transition from the valence band to the  $\text{Fe}^{2+}(^5\text{E})$  level becomes possible with  $h\nu \geq 0.78$  eV. The competition between  $\text{V.B.} \rightarrow \text{Fe}^{2+}(^5\text{E})$  and  $\text{Fe}^{2+}(^5\text{E}) \rightarrow \text{C.B.}$  is likely to be responsible for the PC maximum at 7 K and the slowly varying features at  $0.8 < h\nu < 1.1$  eV in our experiment. However, this PC response will be influenced by the Fermi level which determines the fractional occupation of  $\text{Fe}^{2+}(^5\text{E})$ . The broad band at 0.44 eV was ascribed to the resonance photoconductivity<sup>23</sup> resulting from an  $\text{Fe}^{2+}$  intracenter optical excitation followed by a thermal excitation to the conduction band. This PC band corresponds to the 0.35-eV emission due to an  $\text{Fe}^{2+}$  intracenter transition in the PL.

From both photoluminescence and photoconductivity experiments we know that the zero-phonon line of the 1.06 eV band is at 1.18 eV and the strong PC onset occurs at 1.1 - 1.2 eV. Furthermore, the plot of the relative emission intensity of the 1.10 eV band - vs -  $10^3/T$  yields an activation energy of  $0.24 \pm 0.02$  eV, which corresponds to the thermal release of a carrier bound to the defect center  $(\text{Fe})_{\text{I}_n} - (\text{V})_{\text{p}}$ . So the zero-phonon energy involves a transition to the defect center relative to the band edge.

We can consider that the PC onset is initiated from the zero-phonon energy of the 1.06-eV band. The peak energy of the 1.06-eV band remains at almost the same energy for  $T = 7 - 100$  K and shifts to a lower energy with an increase in temperature. However, we note that  $\text{Fe}^{2+}({}^5\text{T}_2)$  is at  $E_v + 1.13$  eV, near  $T = 7$  K, when  $\text{Fe}^{2+}({}^5\text{E})$  is located at  $E_v + 0.78$  eV. The transition  $\text{V.B.} \rightarrow \text{Fe}^{2+}({}^5\text{T}_2)$  will enhance hole excitation and give the PC onset at 1.13 eV. In this case the large difference of the photoionization cross-section between the transitions  $\text{V.B.} \rightarrow \text{Fe}^{2+}({}^5\text{E})$  and  $\text{V.B.} \rightarrow \text{Fe}^{2+}({}^5\text{T}_2)$  remains to be answered.

### 8.3 Conclusions

Both photoluminescence and photoconductivity methods were used to investigate the nature of the 1.10-eV band and the 1.10-eV threshold in P.C. spectra. A nearest-neighbor molecular-like center  $(\text{Fe})_{\text{I}_n} - (\text{V})_{\text{p}}$  is responsible for the 1.10-eV emission in n-type and Fe-doped semi-insulating material. The P.C. onset at  $\sim 1.10$  eV can also be ascribed to the  $(\text{Fe})_{\text{I}_n} - (\text{V})_{\text{p}}$  which has a carrier trapping level of 0.24 eV.

## 9.0 DEFECT STUDIES IN GaAs

### 9.1 Introduction

In this section, the experimental work concerning native defects will be presented. The primary tool for the study of native defect has been the use of 1 MeV electron irradiation to introduce simple point defects (a major constituent of the full class of native defects). The "native" defects were then studied using electrical measurements, transient capacitance, photoluminescence, and far-infrared spectroscopy. The bulk of the effort has been in the areas of electrical measurements and capacitance studies and this report will deal exclusively with these two aspects of the native defect work. Since most of this work has been published, only brief summaries of the major conclusions will be presented here.

### 9.2 Defects in n-type GaAs

The following abstract is reprinted from Ref. 17.

We have studied the production and annealing of defects produced by 1-MeV electron irradiation of n-type GaAs. Two of these defects lie at 0.15 and 0.31 eV from the conduction band, respectively; in addition, there is at least one acceptor much closer to the valence band. The carrier-removal rate depends upon sample purity but is independent of the irradiation flux. The removal rate is also highly dependent upon the position of the Fermi level, an effect which is considered in some detail. At about 200°C, the defects recover in two stages, with the respective recovery rates given by  $\lambda_1 \approx 3 \times 10^8 \exp(-1.2/kT)$  and  $\lambda_2 \approx 1 \times 10^{12} \exp(-1.6/kT)$  where the energies are in eV;  $\lambda_2$  is somewhat dependent upon sample purity. In the highest-purity samples a reverse recovery phenomenon sometimes occurs, on about the same scale as  $\lambda_1$ . We present models for the production and recovery which are consistent with most of these results, as well as with other data found in the literature. It is suggested that the activation energies found in  $\lambda_1$  and  $\lambda_2$  may well be dissociation energies, rather than motional energies. Although the observed defects cannot be specifically

identified, it appears that the level at 0.31 eV is a donor, and that at 0.15 eV is an acceptor; however, these conclusions are not firm.

This work has made a large contribution toward the understanding of the nature of the defects created during electron irradiation. The use of the automated Hall effect apparatus built during this contract made possible the precise measurement of the annealing kinetics of the 200°C substage defects (see Fig. 9-1). The detailed study of both defect production and defect annealing leads to the conclusion that the activation energies associated with the annealing are probably dissociation energies rather than motional energies. This conclusion is contrary to the generally accepted view and will undoubtedly stimulate further research in this important area. This work also casts strong doubts as to the validity of the identification of the gallium vacancy with the so-called E3 defect in capacitance spectroscopy.<sup>64</sup> A recent publication further supports our conclusions.<sup>65</sup> In other words, even through an enormous effort (covering a span of 20 years) has been made toward the identification of the simplest defects in GaAs, not a single defect has been clearly identified. However, much progress has been made recently and it is almost certain that continued diligence in this area will bear much fruit in the near future.

### 9.3 Type Conversion in Electron-Irradiated GaAs

The following abstract is reprinted from Ref. 14.

The unambiguous type conversion of GaAs by electron irradiation is reported here for the first time. Several high-quality n-type GaAs epitaxial layers ( $\rho \approx 3\Omega\text{cm}$  and  $\mu \approx 7000\text{ cm}^2/\text{V sec}$  at 300 K) were converted by 1-MeV electrons to high-quality p-type layers ( $\rho \approx 30\Omega\text{cm}$  and  $\mu \approx 400\text{ cm}^2/\text{Vsec}$ ). Temperature-dependent Hall-effect data show energy levels at 0.5, 0.3, and 0.1 eV above the valence band. Evidence is presented to indicate that the failure of some of our samples (and, perhaps, other samples reported in the literature) to convert to low-resistivity p type is due to a rather high

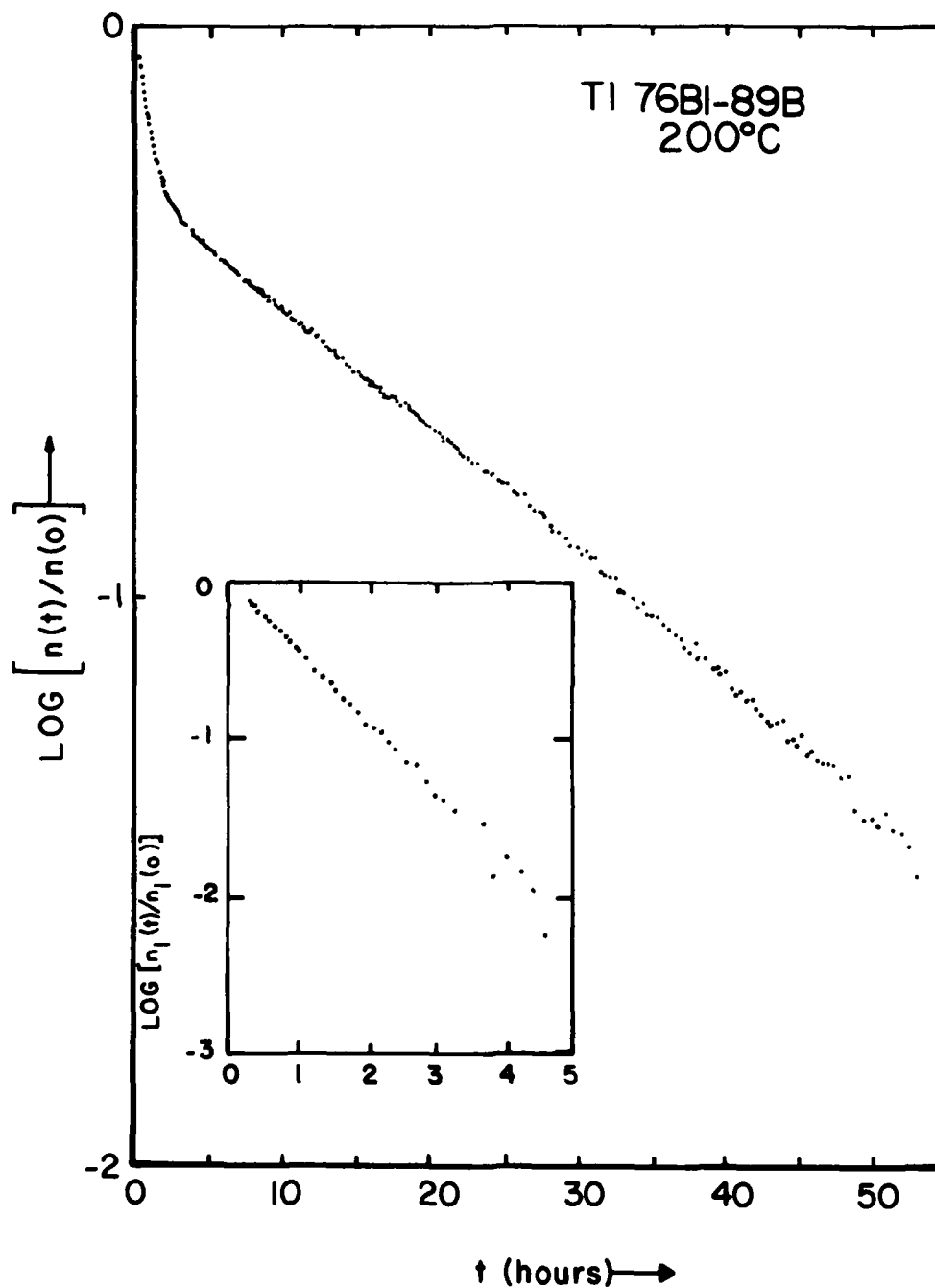


Fig. 9-1. Isothermal anneal at 200°C. The insert is obtained by subtracting the linear portion of the curve (extrapolated back to zero time) from the rest of the data.



concentration of as-grown deep levels which pin the Fermi level near midgap.

This work has been significant in two ways. Not only does it represent a first-time identification of the electron-irradiation-induced type-conversion effect, but it also yields additional information concerning the distribution of defects in the band gap. Prior to this work it was thought that the major fraction of electron-irradiation defects were in the upper third of the band gap. The observation of type conversion clearly means that there is a significant fraction of defects in the lower third. This finding has broad implications in regard to the identification of defects in GaAs. Any model of defect production and annealing must take into account the presence of a large fraction of defects in the lower part of the band gap.

#### 9.4 Defect Studies in Multilayer Epitaxial GaAs by Transient Capacitance.

The following abstract is reprinted from Ref. 66.

Majority-carrier defects, induced by 1-MeV-electron irradiation in n-type epitaxial GaAs were studied by deep-level-trap spectroscopy. The samples were fabricated in the form of FET-like devices on the epitaxial active and buffer layers. Anomalies in the DLTS response such as the appearance of double peaks, a rapid growth of transient response, and lack of exponential behavior as the depletion width extends into the buffer are discussed in terms of the planar geometry, the series resistance, and the multilayer nature of the devices.

Recently there has been a great interest in this relatively new technique for the study of defects, DLTS (deep level transient spectroscopy). This technique provides a relatively simple method to fingerprint a distribution of individual defect levels throughout a large portion of the band gap. The popularity of the DLTS technique is largely due to its ease of use. However, a firm understanding of the physics of the measurement process is required to avoid some subtle pitfalls in the technique. The paper referenced above addresses some of these anomalies and points out the need for care in the proper use of the DLTS technique.<sup>66</sup>

## 9.5 Persistent Photoconductivity in GaAs: Relationship to Low-Temperature Solar Cell I-V Characteristics

The following abstract is reprinted from Ref. 67.

We have studied persistent photoconductivity in thin epitaxial GaAs. The dependence of the persistent photoconductivity on photon dose was studied. At high fluences a decay component was also observed. The temperature dependence of the persistence was determined. All the data are qualitatively well understood in terms of a macroscopic barrier model of persistent photoconductivity. At low fluences excellent quantitative agreement between theory and data is obtained. In addition, low temperature I-V characteristics of GaAs solar cells were measured. It was found that the low temperature data cannot be explained by the traditional generation-recombination model. The relationship between persistent photoconductivity and low temperature I-V characteristics of solar cells is discussed.

While the observation of persistent photoconductivity in thin epitaxial GaAs has previously been attributed to a macroscopic barrier model,<sup>68</sup> this paper represents the first clear interpretation of the data in a physically meaningful model. The dependence of the persistent photoconductivity on fluence is in excellent quantitative agreement with the model at low fluences (see Fig. 9-2). In the simplest example the model addresses the case of the macroscopic barrier (or junction) associated with the epilayer-substrate interface. We find that in all instances, except after low fluences, the effects of the front surface junction must also be included. The addition of the second junction greatly complicates the theoretical analysis and one is forced to rely solely on qualitative agreement between data and model.

A study of the I-V characteristics of GaAs solar cells at low temperature provided additional support for the macroscopic barrier model of persistent photoconductivity.<sup>67</sup> Analysis of the decay of the open-circuit voltage following a pulse illumination was in excellent agreement with the directly measured

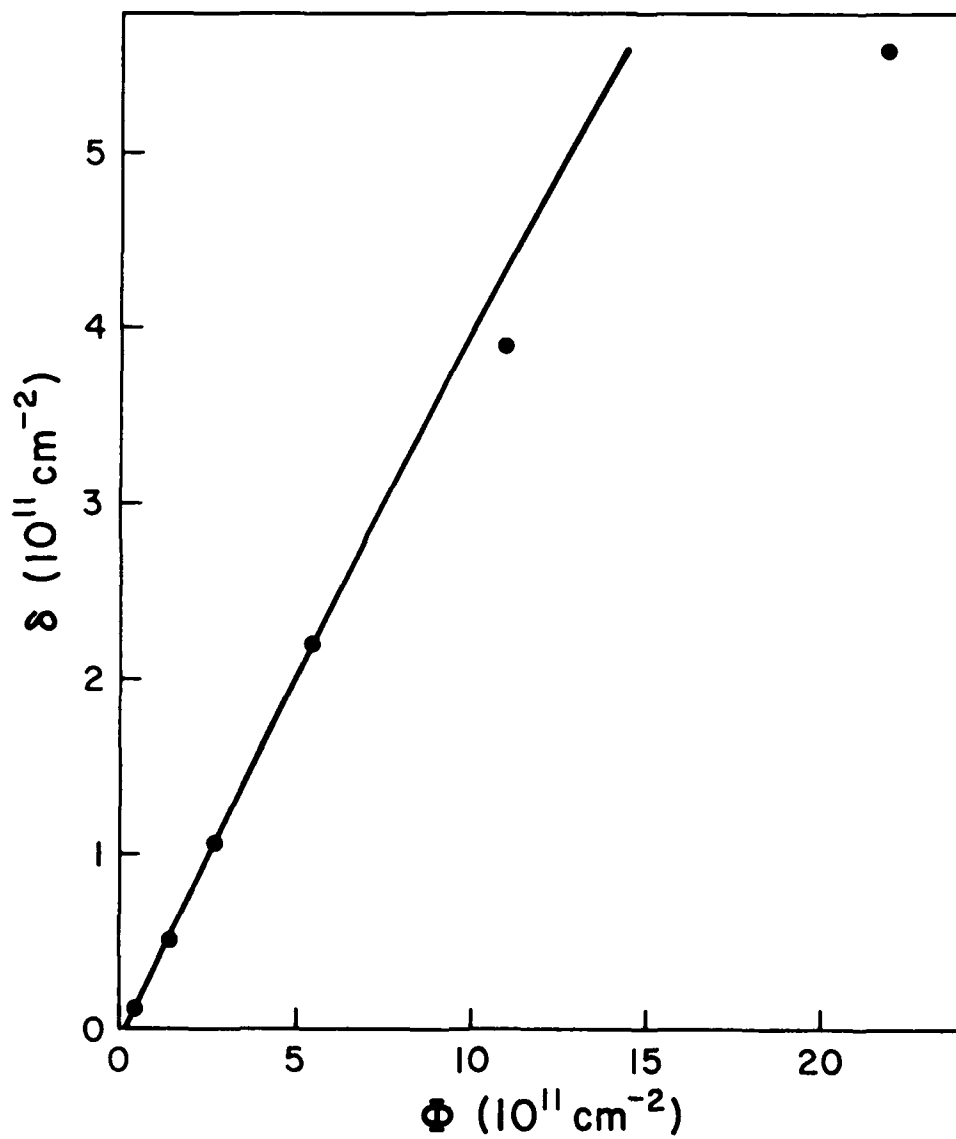


Fig. 9-2. Change in sheet carrier concentration vs. photon fluence. The solid line is from a calculation based on a macroscopic barrier model of persistent photoconductivity.

I-V curve (see Fig. 9-3). However, some severe shortcomings in the traditional interpretation of the I-V characteristics were found at low temperature. The application of the generation-recombination model to the low temperature data gives unphysical results. Clearly another mechanism is at least partially responsible for the characteristics of the low temperature data. The relatively small dependence on temperature suggests that tunneling may play a role.

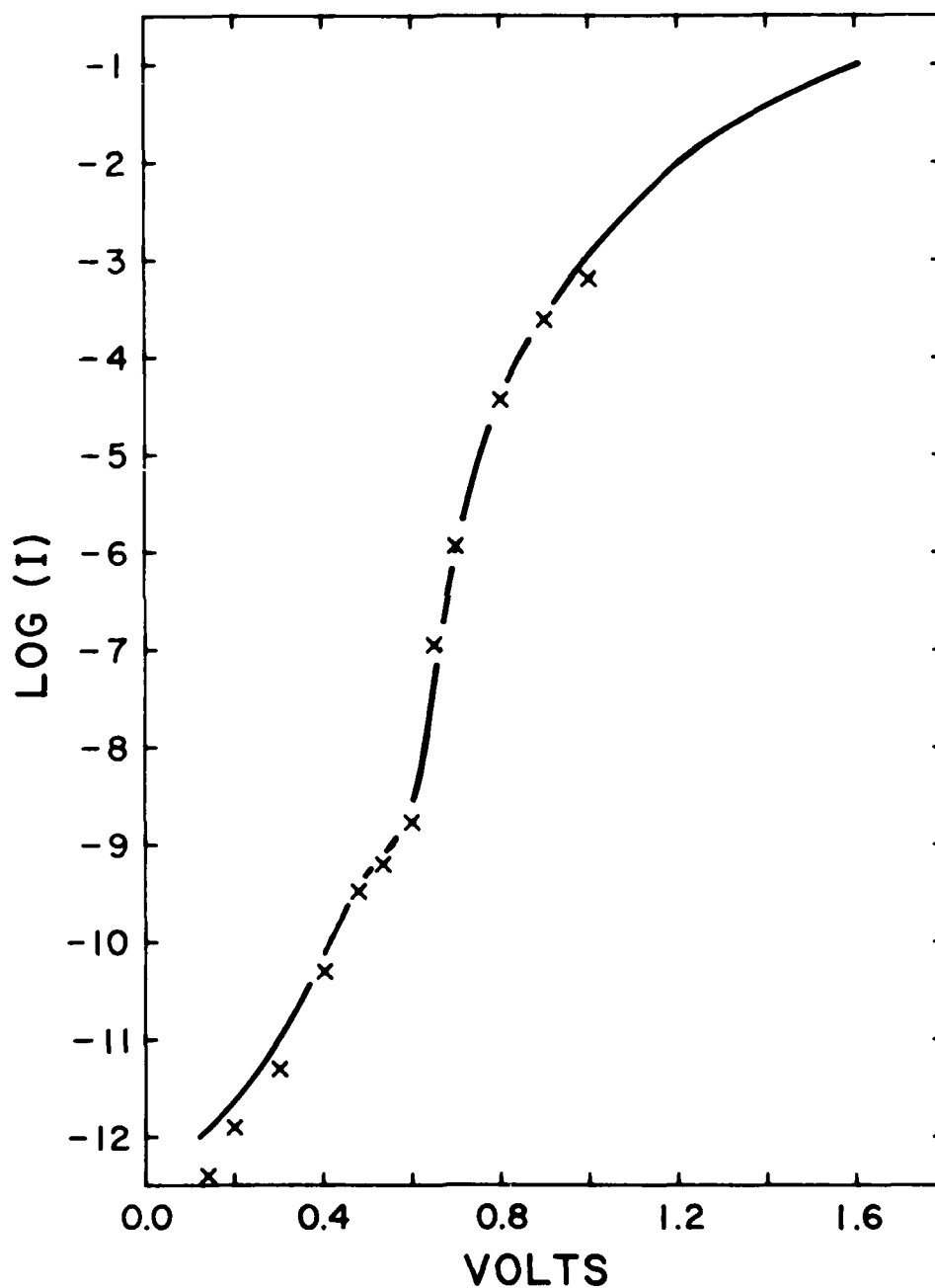


Fig. 9-3. Current vs. forward-bias voltage at LN<sub>2</sub> temperature. The solid line is for directly measured I-V, and the "x's" are for I-V calculated from open-circuit voltage decay data following pulse illumination.

## 10.0 FAR INFRARED STUDIES IN GaAs

Materials such as high resistivity GaAs appear to be well suited for material characterization by the localized phonon mode technique. The method is known to be non-destructive and it can be used to obtain information about the chemical nature of the impurity and its location in the lattice. Both electrically active and inactive purities can be identified by their absorption spectra.

The GaAs characterization effort using infrared spectroscopy has centered around the investigation of localized vibrational modes (LVM) arising from various impurities in the GaAs system. The first phase of this work involved the verification of Si LVM due to Si impurity in bulk GaAs. We have performed experiments on crystals of high resistivity GaAs at 30, 100, and 300 K, with silicon impurity in the  $10^{17}$ - $10^{19}$  cm<sup>-3</sup> range in an attempt to study the possibility of using the method for quantitative analysis of the impurity.<sup>69</sup> Localized phonon modes related to the presence of the silicon impurity have been observed as discrete absorptions in the energy interval 300-400 cm<sup>-1</sup> with a temperature dependence of  $\sim -0.02$  cm<sup>-1</sup>/K in the 100-300 K temperature range.

We were able to verify the absorption peaks<sup>70</sup> due to Si impurity on the substitutional gallium and arsenic sites,  $\text{Si}_{\text{Ga}} = 384$  cm<sup>-1</sup> and  $\text{Si}_{\text{As}} = 399$  cm<sup>-1</sup>, respectively, thus supporting the amphoteric nature of Si in GaAs. In addition, we have verified the LVM due to various Si nearest neighbor complexes<sup>71</sup> and the existences of absorption lines due to the Si isotopes<sup>72</sup>  $^{28}\text{Si}$ ,  $^{29}\text{Si}$ , and  $^{30}\text{Si}$ , and their complexes. Moreover, the observation of naturally occurring LVM peaks due to  $^{27}\text{Si}_{\text{Ga}}$  and  $^{30}\text{Si}_{\text{Ga}}$  in the data were used to demonstrate the ability to observe Si below the  $10^{17}$  cm<sup>-3</sup> range since these isotopes exist in abundance of only 6.2 and 4.2% (respectively) of the total Si content. Subsequently we were able to observe Si impurity in concentrations ranging from  $3 \times 10^{16}$  to  $3 \times 10^{19}$  cm<sup>-3</sup> with absorption coefficients of Si atoms

in various sites and complexes ranging from  $1$  to  $110 \text{ cm}^{-1}$  approximately,<sup>11</sup> demonstrating the ability to employ the LVM technique as a nondestructive characterization tool.

We then turned our attention to carbon impurity in GaAs. Our initial results<sup>73</sup> indicated an absorption peak at  $\sim 582 \text{ cm}^{-1}$  at  $\sim 77^\circ\text{K}$ . This peak is identified as being due to substitutional carbon, an identification which agrees with that of Newman.<sup>74</sup> In other GaAs samples which were reported to have carbon impurity at approximately  $1 \times 10^{17} \text{ cm}^{-3}$  no carbon LVM could be seen, a result that suggested that the mass spectrographic data on this impurity might be invalid. (Since carbon is a common contaminant in the mass spectrographic analysis technique, this conclusion is easily believable.)

Having observed carbon in a number of carbon doped GaAs samples, an effort was made to investigate several carbon implanted GaAs crystals. Subsequently we reported<sup>75</sup> the first observation of the LVM due to carbon implanted in GaAs. The relative transmission as a function of energy for three different GaAs crystals at  $\sim 82^\circ\text{K}$  is shown in Fig. 10-1 for several annealing temperatures. It was observed<sup>12,76</sup> that for annealing temperatures below  $300^\circ\text{C}$ , the LVM absorption increases, while above  $500^\circ\text{C}$  it decreases rapidly. The reader is referred to the published work for further details on carbon and for comparisons with the behavior of the LVM's of other implants in GaAs. It may be noted that the LVM's of other impurities such as Al (occurring in a Laser Diode sample) were easily observed during the course of the carbon study.

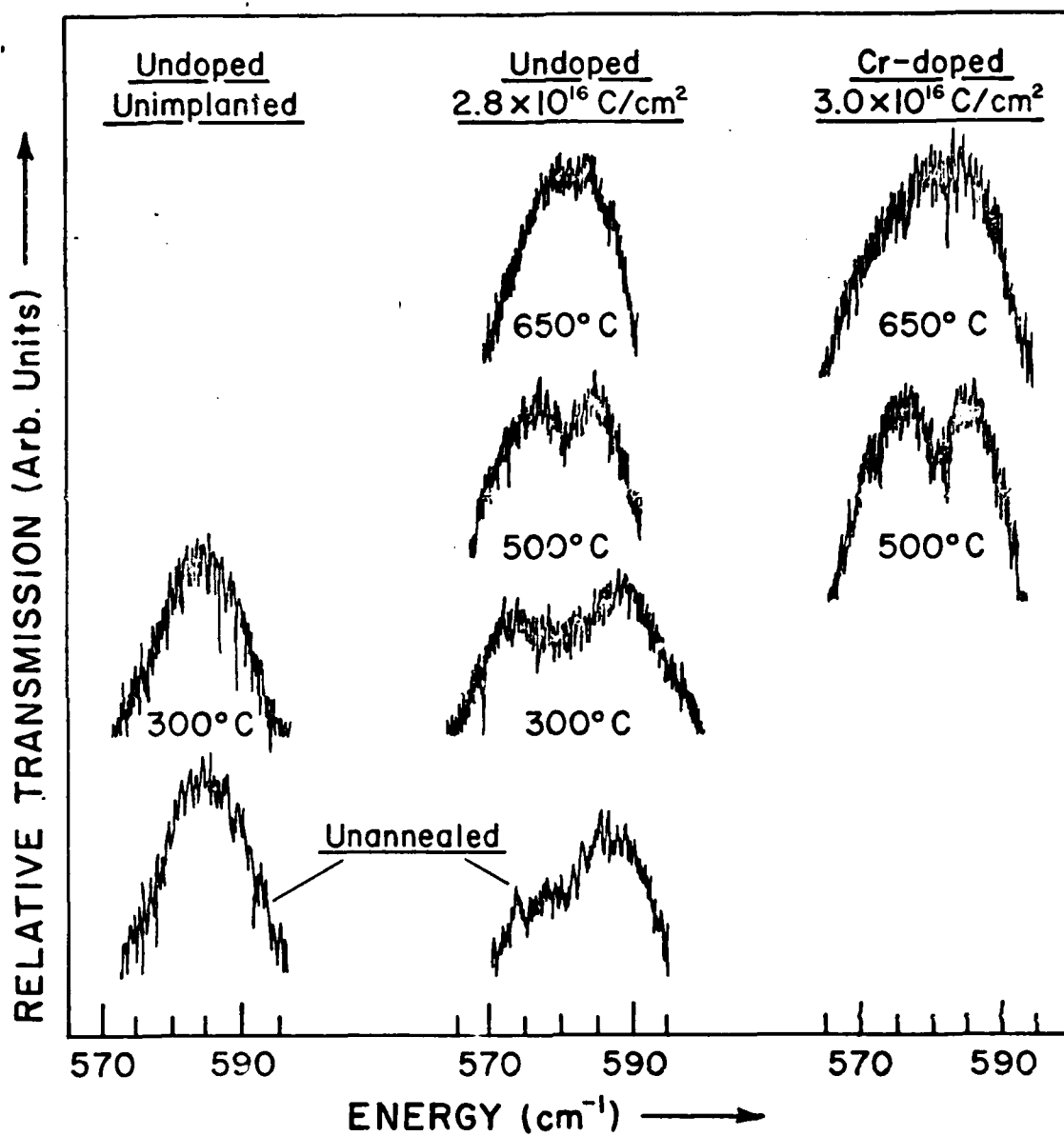


Fig. 10-1. Relative transmission and annealing temperature as a function of energy for three different GaAs crystals. All data shown here were taken with the samples at ~82 K.



## 11.0 SPARK SOURCE MASS SPECTROSCOPY IN GaAs

### 11.1 Background

Traditionally, spark source mass spectrometry has been utilized for the comprehensive identification and quantification of the elemental make-up of inorganic, solid materials with the major emphasis on trace and ultra-trace elemental impurities. The participation of the SSMS (MS-702, AEI-CEC Ltd., Manchester, England) facility located at Wright State University's Brehm Laboratory was initiated in late 1979 to assist AFWAL/AADR in its characterization of gallium arsenide research materials. Since the type and concentration of many elemental impurities-both doped and residual- are known to drastically affect the electrical properties of GaAs, the basic function of the SSMS effort has been to provide reliable determinations of low-level impurities in GaAs samples, including thick epitaxial layers and substrate materials. In the past year about 70 GaAs and InP samples have been analyzed.

### 11.2 Analytical Program

Two major goals involving the spark source mass spectrometer were pursued:

- 1) The development of calibration techniques for the accurate measurement of Cr, primarily, and other elements of interest such as Fe, Mn, Si, B, Cu, Zn and Te.

- 2) The reduction of instrument background levels of oxygen and carbon to allow analytical determination of less than 0.1 part per million, atomic (ppma).

In conjunction with the initial goal, supplementary analytical techniques such as atomic-absorption spectrophotometry, optical emission spectroscopy,

neutron activation, and secondary ion mass spectrometry were employed. The results from these analyses are given in Table 11-1. Generally, the agreement between the various methods is reasonable. The large discrepancies occurring for Fe and Cr determinations between AAS and SSMS are possibly due to inconsistent flame characteristics of AAS sample and standard analysis. Also, samples HP E654-2 and E654-5 are two wafers from a boule which was purposely doped with many elements and turned out highly polycrystalline. Both wafers are undoubtedly inhomogeneous but especially E654-5. Therefore, some rather large discrepancies may be expected.

The second goal sought during the program involved the development of a new cryogenic pumping system for the ion source of the MS-702 spark source mass spectrometer. A stainless-steel source flange assembly was designed and fabricated at Wright State University to permit transfer of liquid helium from a storage dewar (Cryofab Model CMSH) to a special retractable cooling collector which is positioned inside the ion source vacuum housing. Transfer of liquid helium is accomplished by using an Air Products and Chemicals Heli-Tran Model LT-3-110, which permits cooling of a copper collector disc via a 1/8" Cryo-probe to the  $10^{\circ}\text{K} - 20^{\circ}\text{K}$  temperature range. The operating temperature is regulated by a controlled flow of liquid helium and is monitored by a silicon diode sensor with digital read-out. A picture of the Cryo-probe assembly is included as Fig. 11-1.

Data obtained by SSMS cryopumping experiments are shown in Table 11-2 and Figures 11-2 and 11-3. It is seen that the C and O background levels decrease dramatically with LHe cryopumping.

### 11.3 Summary

It is felt the program objectives of establishing reliable analytical methods for the trace elemental impurity characterization of GaAs were largely successful. In addition to spark source mass spectrometry, valuable contributions

Table 11-1 Comparison of several trace analytical techniques for GaAs  
(all concentrations in ppmA)

Element	Technique	Sample						HP F436-E
		HP F409-ES	LD 5169	HP E654-2	BA 067	LD 8250	HP E654-5	
Al	OES	<0.3	<0.3	1.8	2.2	1.5	0.5	
	SSMS	<0.01		0.1	<0.03	5	1	
Ca	OES	<0.2	4.5	11	<0.2	2	3	
	SSMS	<0.1	3	1	<0.1	20	1	
Cr	OES	2.8	<0.01	1.7	0.08	0.43	26,000	
	SSMS	2	<0.03	1	0.03	2	1000	<.06
	NA	2.2			<0.15	4.9		<.5
	SIMS	1.3				2.8		<.05
	AA	100	<1				30	
Cu	OES	<0.03	<0.03	3.8	<0.03	<0.03	200	
	SSMS	<0.03	<0.05	0.5	<0.02	<0.03	100	
	AA						100	
Fe	OES	2.3	0.5	1	<0.1	0.16	770	
	SSMS	0.1	1	2	0.5	1	200	
	AA	30	20				150	
Mn	OES	<0.1	<0.1	<0.1	<0.1	<0.1	<0.2	
	SSMS	<0.01	<0.03	<0.1	<0.03	<0.03	2	
	AA						4	
Na	OES	<3	<3	<3	<3	<3	<3	
	SSMS	<1	<1	<1	<1	10	<1	
Mg	OES	<0.03	<0.03	0.06	<0.03	0.06	0.03	
	SSMS	<0.3	<0.3	<0.3	<0.3	<0.3	<0.3	
Si	OES	0.8	3.6	0.47	9	0.03	0.05	
	SSMS	<0.3	10	3	20	30	30	
Zn	OES	<4	23	<4	<4	<4	5	
	SSMS	<0.06	25	2	<0.06	<0.06	10	
	NA		50					
	AA		138					
Sn	SSMS	<0.1	<0.1	<0.1	<0.1	<0.1	2	
	NA						11	
	AA						10	

Notes: OES ≡ Optical Emission Spec., performed by Eagle Picher  
SSMS ≡ Spark-source Mass Spec., performed at Wright State U.  
NA ≡ Neutron Activation Anal., performed by General Activ. Anal.  
SIMS ≡ Secondary Ion Mass Anal., performed by C. A. Evans, Assoc.  
AA ≡ Atomic Absorption Anal., performed at Wright State U.

HP ≡ Hewlett-Packard  
LD ≡ Laser Diode  
BA ≡ (unknown crystal vendor)

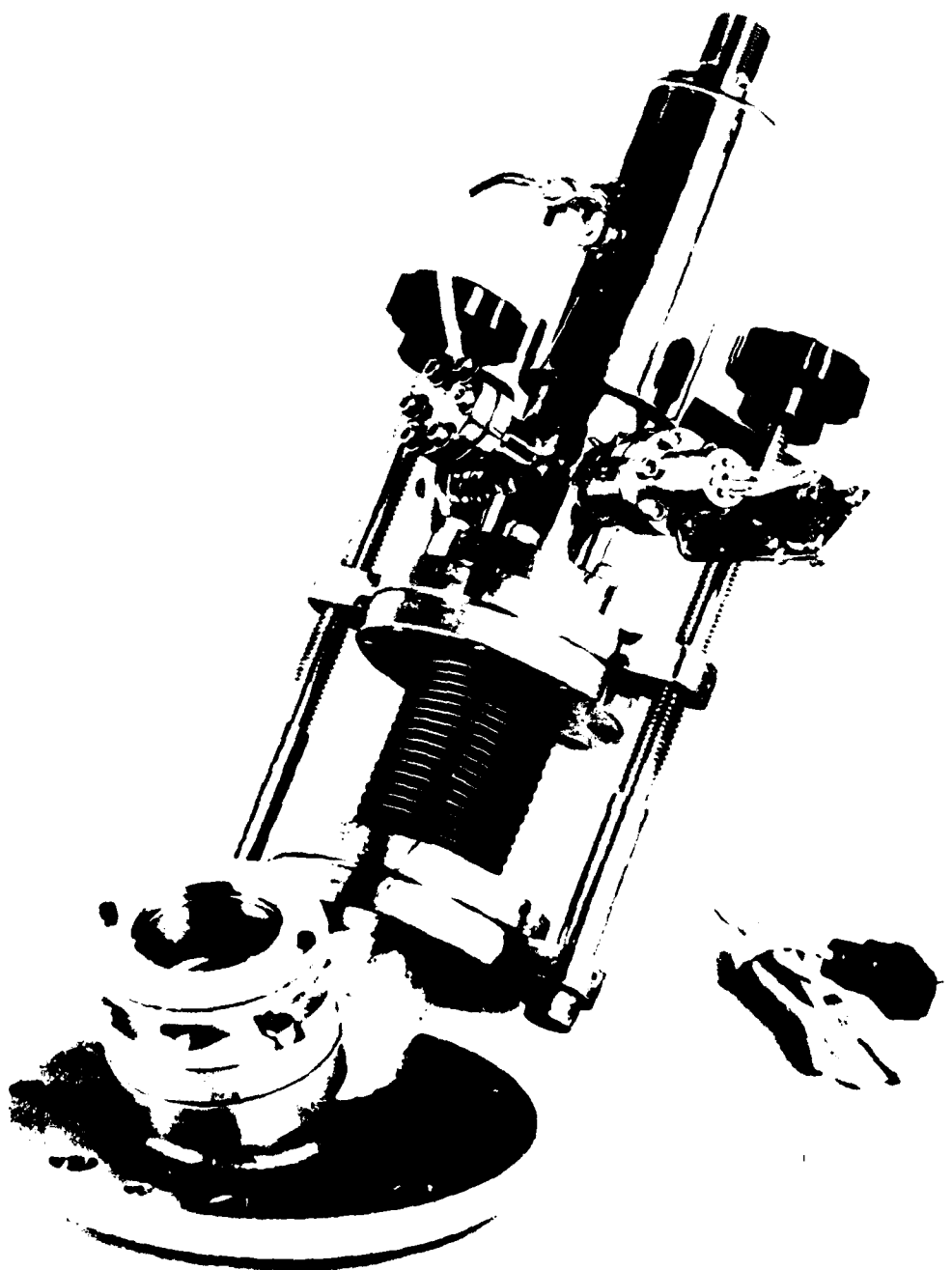


Fig. 11-1. A photograph of the cryo-probe assembly which utilizes an Air Products Heli-Tran LHe transfer system.

Table 11-2 Spark source mass spectrographic analysis of GaAs  
under LHE cryopumping (concentrations in ppmA)

Element	HP49/79 F409-ES (a)	MA155/80 B-3-S	Sample		MA158/80 B-10-S	MA187/80 B-5-7
			MA156/80 B-5-S	MA157/80 B-5-T		
B	0.03	<0.01	<0.01	<0.01	<0.01	<0.01
C	0.1	0.1	0.1	0.1	0.1	0.1
O	0.05	0.05	0.05	0.3	0.1	0.1
Mg	<0.03	<0.03	<0.03	<0.03	<0.03	<0.03
Al	0.03	0.3	0.1	<0.03	<0.03	<0.1
Si	<0.3	1	0.3	<0.1	<0.1	<0.1
S	<0.03	<0.1	<0.1	<0.1	<0.3	<0.1
Cr	2	<0.03	0.03	<0.02	0.1	<0.03
Fe	<0.3	1	<0.2	<0.2	0.3	<0.2
Zn	<0.06	<0.02	<0.02	<0.02	<0.06	<0.02

(a) Average of three runs

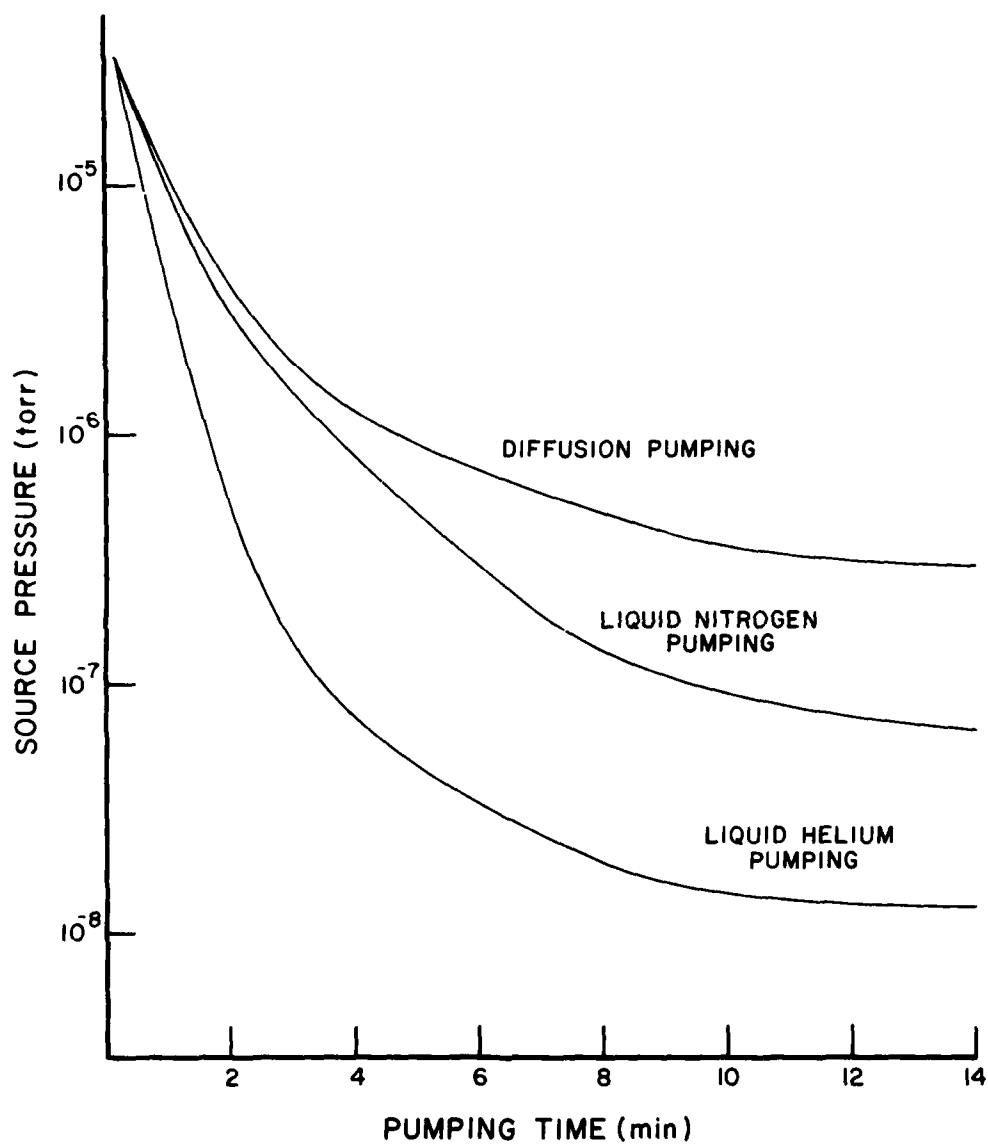


Fig. 11-2. The source pressure as a function of pumping time for three different types of pumping. The diffusion pumping is standard on the MS-702, the  $\text{LN}_2$  pumping involves a commercially available faceplate modification, and the  $\text{LHe}$  pumping is described in this report.

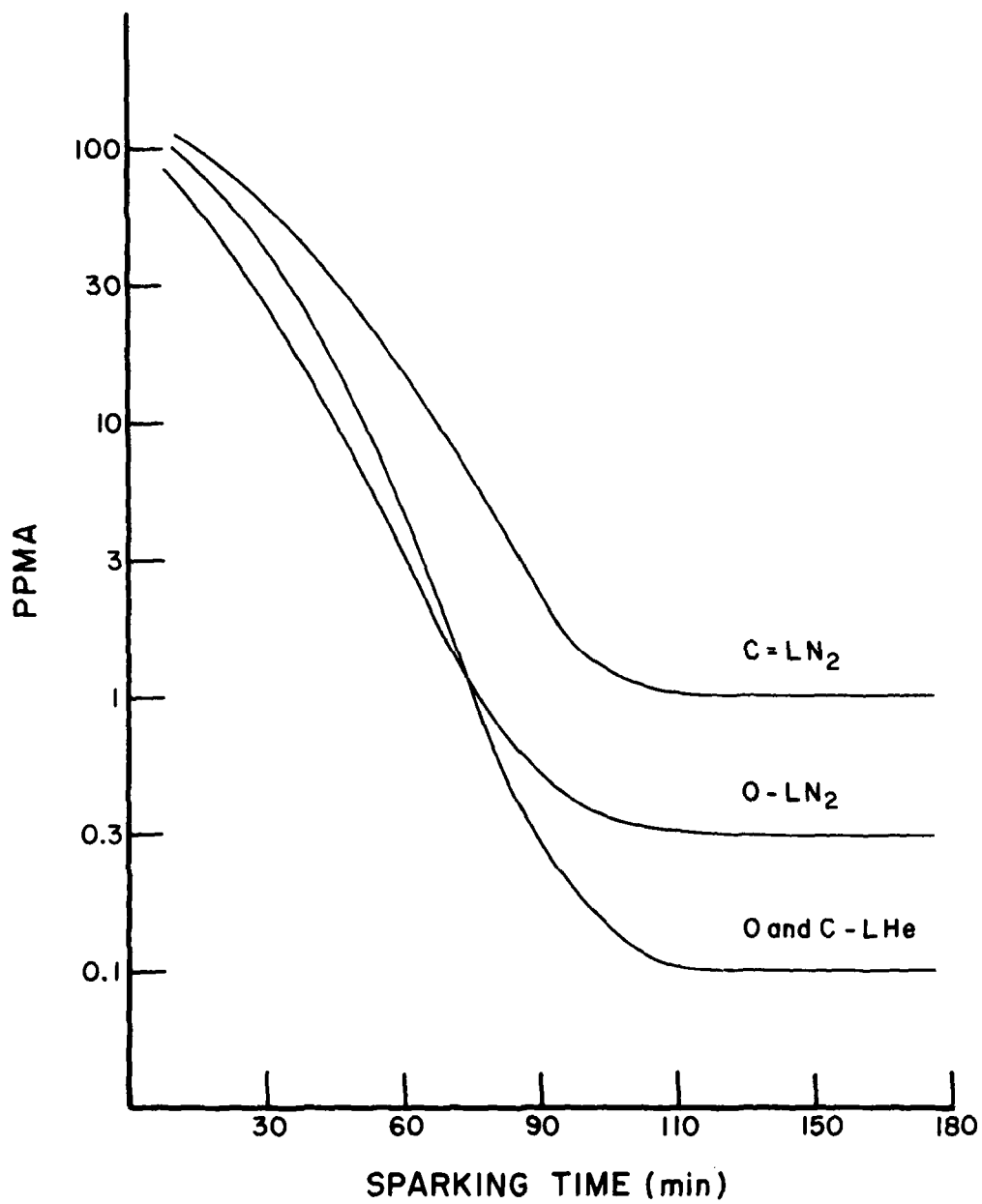


Fig. 11-3. The measured C and O concentrations as a function of sparking time for both LN<sub>2</sub> and LHe cryo-pumping.

to the program were obtained from other analytical techniques. In particular, optical emission spectroscopy and secondary ion mass spectrometry were found to offer great potential for the routine evaluation of trace impurity concentrations in semiconductor material.



## 12.0 OPTICAL SCHEME FOR DETERMINATION ON CONCENTRATIONS OF DONORS AND ACCEPTORS IN A SEMICONDUCTOR

### 12.1 Introduction

The impurity centers in a semi-conductor play a major role in its electrical properties. The concentrations of donors ( $N_D$ ) and acceptors ( $N_A$ ) in a semiconductor are very important parameters for characterizing it. They are determined conventionally by electrical means, such as, resistivity and Hall-effect measurements. These measurements require electrical contacts and homogeneity of the sample. Even though these problems may be resolved, the results rely on the theoretical treatments of various scattering processes of carriers<sup>77,78</sup>. Thus it is desirable to have an entirely different method for determination of  $N_D$  and  $N_A$ . One of these schemes is an optical one which does not require any contacts and can scan the homogeneity of the sample. Recently there have been several attempts made to obtain the compensation ration,  $N_D/N_A$ , by analyzing the shapes of photoluminescence emission bands due to the conduction band-to-neutral acceptor and neutral donor-to-neutral acceptor transitions at low excitation levels.<sup>79</sup> The method still needs the value of  $N_D - N_A$  from electrical measurements to determine  $N_D$  and  $N_A$ .

We have developed a scheme by which  $N_D$  and  $N_A$  are determined solely from the optical data, based on the charge neutrality condition and the pseudo-sum rules of the photoluminescence intensities due to the conduction band-to-neutral acceptor ( $I_{CA}$ ), neutral donor-to-valence band ( $I_{DV}$ ), and neutral donor-to-neutral acceptor ( $I_{DA}$ ) transitions. In Sec. 12.2, the theoretical descriptions are given, and the deduction methods for obtaining  $N_D$  and  $N_A$  from optical data

AD-A100 399

DAYTON UNIV OHIO DEPT OF PHYSICS  
CHARACTERIZATION OF III-V SEMICONDUCTORS.(U)  
APR 81 D C LOOK, M M KREITMAN, P WON YU

F/G 20/12

F33615-76-C-1207

UNCLASSIFIED

AFWAL-TR-81-1036

NL

2 of 2  
AD-A  
10-13-81



END  
DATE  
FILMED  
7-81  
DTIC

are given in Sec. 12-3. In Sec. 12-4, the determinations of the mean life times and mobilities of electrons and holes are described. In Sec. 12-5 the effective carrier temperatures are deduced from the optical data. In Sec. 12-6, remarks are given.

## 12.2 Theory

When an excitation is introduced in a semiconductor, say optically, electrons and holes are created. They may form excitons, or be trapped on impurity centers and distributed such that the charge neutrality condition is preserved:

$$n + N_A - n_A = p + N_D - n_D, \quad (12-1)$$

where  $n_D$ ,  $n_A$ ,  $n$ , and  $p$  are the concentrations of neutral donors, neutral acceptors, electrons in the conduction band, and holes in the valence band, respectively.

For simplicity, we discuss hereafter a semiconductor with shallow donor and shallow acceptor centers. It is easy to include other centers in the theory and non-radiative centers do not affect the final results, which will be discussed later. The emissions due to the decays of excitons and excitons bound to impurity centers are not of interest here. For our purpose, the emissions associated with impurity centers and bands are studied in detail.

The emission rate of a photon with energy,  $\omega$ , with a polarization vector,  $\hat{e}$ , by an electron from the initial to final states can be written as

$$(2\pi e/m_e)^2 \omega \epsilon^{-1/2} O_i (1 - O_f) |P_{if}|^2 \delta(E_i - E_f - \omega)$$

with the usual matrix element,

$$P_{if} = -i \langle \Psi_i | \hat{e} \cdot \hat{p} | \Psi_f \rangle,$$

where  $E$ 's,  $O$ 's, and  $\Psi$ 's are the energies, corresponding occupation numbers, and wave functions of the initial and final electron states, respectively,

$-i\hat{p}$  and  $\epsilon$  denote the usual momentum operator and the dielectric constant whose dependence on the concentrations is assumed to be insensitive for our purposes.

We use the units of  $\hbar = 1 = c$ , hereafter. It is convenient to write the wave functions of the neutral impurity centers as

$$\Psi_D(r) = F_D(r) U_C(r),$$

$$\Psi_A(r) = F_A(r) U_V(r),$$

where  $F_D$  and  $F_A$  are the slowly varying envelope functions for donor and acceptor,  $U_C$  and  $U_V$  are the usual conduction-electron and valence hole wave functions, respectively. Then the matrix element,

$$M = \langle U_C | \partial | U_V \rangle$$

needs to be calculated for the direct transition. In particular, for a zinc blende structure crystal, such as, GaAs, it can be written by<sup>80</sup>

$$M^2 = m_e E_g (1/m_c^* - 1) (1 + s)/(6 + 4s),$$

where  $E_g$ ,  $m_c^*$ , and  $s$  are the band gap energy, the effective mass of an electron in the conduction band in units of the free electron mass,  $m_e$ , and the ratio of the spin orbital interaction energy to  $E_g$ ; for GaAs,  $s = 0.2$ . For the indirect transition, one can write the corresponding matrix element with the electron-phonon interaction in the second order perturbation.<sup>81</sup> We here discuss a direct band gap material without loss of generality. The theory can easily be extended to an indirect band gap material with the appropriate matrix element.

Using a standard rule<sup>82</sup> and taking into account the appropriate kinematic factor, one obtains easily the desired integrated spontaneous emission intensities, which we call "the pseudo-sum rules of the photoluminescence intensities" as

$$I_{CA} = \int dE N_{CA}(E) = m^2 n n_A f_A^2, \quad (12-2)$$

$$I_{DV} = \int dE N_{DV}(E) = m^2 p n_D f_D^2, \quad (12-3)$$

$$I_{DA} = \int dE N_{DA}(E) = m^2 n_A n_D f_{DA}^2, \quad (12-4)$$

where the  $N$ 's are the spectral densities, and  $m^2$  is the mean value of  $M^2$  times the appropriate kinematic factor,

$$m^2 = 2(e/m_e)^2 \epsilon^{1/2} E_g M^2,$$

$f_D^2$  and  $f_A^2$  are the mean values of the squares of the amplitudes of  $F_D$  and  $F_A$  in  $k$ -space, and  $f_{DA}^2$  is the summation of the square of the overlapping integral of  $F_D$  and  $F_A$ . To obtain the above results, the matrix element is assumed to be almost constant within the energy regimes of interest. The crucial point is to write the integrated emission intensities in terms of  $n$ ,  $p$ ,  $n_D$ , and  $n_A$  with the appropriate  $f$ 's and  $m$  in general cases. The above results can be understood easily by considering a simple physical argument that the total transition probability is proportional to the occupation numbers of the initial states involved.

For a direct band gap material, such as GaAs,  $f_D^2$  and  $f_A^2$  can be approximated by their values at  $k = 0$ , since the main emissions come from the transitions near the band edges. Using the hydrogenic  $s$ -wave functions for  $F_D$  and  $F_A$ , appropriate for shallow donors and shallow acceptors one can obtain easily the  $f$ 's at  $k = 0$  as

$$f_i^2 = \left\{ \int d^3r F_i(r) \right\}^2 = 64\pi r_i^2$$

$$\text{with } F_i(r) = (\pi r_i^3)^{-1/2} \exp(-r/r_i)$$

$$r_i = e^2 / 2\epsilon E_i, \quad (i = D, A),$$

$$\begin{aligned} \text{and } f_{DA}^2 &= \int d^3R J^2(R) \\ &= g(y) f_D^2 \end{aligned}$$

$$\begin{aligned} \text{with } J(R) &= \int d^3r F_D(r) F_A(r - R), \\ &= (1 - z^2)^{3/2} (J_1 + J_2) \exp(-u), \end{aligned}$$

$$J_1 = (1 + u)(\sinh x)/x,$$

$$J_2 = u^2(x \cosh x - \sinh x)/x^3,$$

$$g(y) = \{2y/(1 + y)\}^3 (33 - 22z^2 + 5z^4)/128,$$

$$x = uz,$$

$$y = E_D/E_A ,$$

$$u = (1 + y) R/r_A ,$$

$$z = (1 - y)/(1 + y) ,$$

where  $E_D$  and  $E_A$  are the donor and acceptor binding energies, respectively.

Now the principle idea is to get  $N_D$  and  $N_A$  from Equations 12-1 to 12-4. In the next section we describe how one can get  $N_D$  and  $N_A$  from the optical data I's.

### 12.3 Determination of $N_D$ and $N_A$

The numerical values of  $N_D$  and  $N_A$  can be obtained from the optical data of the I's by observing that the n's depend upon the excitation intensity, G.

#### 12.31 Limiting method

It is easy to show, using the rate equation, that the behavior of the n's with excitation intensity is as follows: in the high excitation limit,

$$\lim_{G \rightarrow \infty} (n_D, n_A) \rightarrow (N_D, N_A) \quad (12-5)$$

and the charge neutrality condition yields  $p=n$ , while, in the low excitation limit,

$$\lim_{G \rightarrow 0} (n_D, n_A) \rightarrow (N_D - N_A, 0) \text{ for n-type} , \quad (12-6a)$$

$$\lim_{G \rightarrow 0} (n_D, n_A) \rightarrow (0, N_A - N_D) \text{ for p-type}$$

materials, respectively.

Note that at low temperature, the numbers of thermally excited electrons and holes are negligibly small,

$$|n - p| \ll |N_D - N_A| \quad (12-7)$$

Thus, getting the expressions for  $n$ ,  $p$ ,  $n_D$ , and  $n_A$  in terms of  $N_D$  and  $N_A$  and taking their limiting values one can achieve the desired objective.

From Equations 12-1 to 12-4, one gets the following expressions for p-type material,

$$n_D = (B^2 + d\gamma)^{\frac{1}{2}} - B = n/C \quad (12-8)$$

$$n_A = \{(B^2 + d\gamma)^{\frac{1}{2}} + B\}/\gamma = p/V \quad , \quad (12-9)$$

with  $\gamma = (1 + V)/(1 + C) = 2\beta(1 + V) \quad ,$

$$B = \beta(N_A - N_D) \quad ,$$

$$C = (I_{CA}/I_{DA})(f_{DA}/f_A)^2 = (I_{CA}/I_{DA}) g(y)/y^3 \quad ,$$

$$V = (I_{DV}/I_{DA})(f_{DA}/f_D)^2 \quad ,$$

$$d = I_{DA}/(mf_{DA})^2 \quad .$$

Taking the limiting values of the above expression, we get

$$\lim_{G \rightarrow 0} F_1 = (N_A - N_D)mf_{DA} = L = \lim_{G \rightarrow \infty} F_2 \quad , \quad (12-10)$$

$$\lim_{G \rightarrow \infty} F_3 = N_D/N_A = \lim_{G \rightarrow \infty} F_4 \quad (12-11)$$

with

$$F_1 = \{I_{DA}(1 + C)/V\}^{\frac{1}{2}}$$

$$F_2 = (I_{DA} C/V)^{\frac{1}{2}} - (I_{DS} V/C)^{\frac{1}{2}}$$

$$F_3 = \{(b^2 + \gamma)^{\frac{1}{2}} - b\}^2$$

$$F_4 = V/C$$

$$b = B/d^{\frac{1}{2}} = \beta L/(I_{DA})^{\frac{1}{2}}$$

For n-type material, the equivalent formulae are obtained by simply interchanging donor and acceptor variables.

The value of  $N_A - N_D$  can be obtained by dividing  $L$  of Eq. 12-10 by  $mf_{DA}$ , in two different cases. The value of  $L$  is needed for  $F_3$ , but for  $F_4$  it is not. Finally,  $N_D$  and  $N_A$  are to be obtained from the optical data. Note that to obtain only  $N_D/N_A$ , the value of  $mf_{DA}$  is not required; only the excitation dependent  $I$ 's and ratios of  $f$ 's which turn out for our case to depend on only  $v(= E_D/E_A)$ , are needed without any other parameter.

Let us examine the effect of non-radiative centers on the above results. Consider a semiconductor with the concentrations of non-radiative donors ( $N_D^t$ ) and non-radiative acceptors ( $N_A^t$ ), and study the excitation dependencies of neutral non-radiative donor ( $n_D^t$ ) and acceptor ( $n_A^t$ ) concentrations. Then the limiting values of  $n_D^t$  and  $n_A^t$  in the low and high excitation regimes will be given by  $N_D^t$  and  $N_A^t$  in the forms similar to those of Equations 12-5 and 12-6 with the superscript,  $t$ . Thus, non-radiative centers do not affect the limiting values of  $F$ 's. In other words, they are irrelevant for getting  $N_D$  and  $N_A$ . When the condition of Eq. 12-7 is relaxed, the limiting values of  $F_1$  and  $F_2$  in two opposite limits may have different values due to the appreciable numbers of thermally excited carriers. This can be avoided by carrying out measurements at reasonably low temperature, say, liquid helium temperature.

The initial test of this scheme was carried out in a high quality GaAs epitaxial layer sample at about 8K, and the results are in excellent agreement with theoretical predictions.<sup>15</sup>

#### 12.32 Random variable method

The values of  $N_D$  and  $N_A$  remain constant, even though the  $n$ 's are varying with the excitation intensity. This observation leads us to get  $N_D$  and  $N_A$  by treating  $x = n_D/N_D$  and  $y = n_A/N_A$  as independent variables. From Equations 12-8 and 12-9, we get  $N_D$  and  $N_A$  in terms of  $x$ ,  $y$ , and the  $I$ 's as



$$N_D = (d/xy)^{1/2} (\gamma y - 2\beta)^{1/2} / (x - 2\beta)^{1/2} , \quad (12-12)$$

$$N_A = (d/xy)^{1/2} (x - 2\beta)^{1/2} / (\gamma y - 2\beta)^{1/2} . \quad (12-13)$$

Next we write  $x$  and  $y$  in terms of  $g(G)$  as

$$x = \sum D_i g^i(G) , \quad (12-14)$$

$$y = \sum A_i g^i(G) , \quad (12-15)$$

where the functional form for  $g(G)$  is by no means unique. The best choice would be in the form of formal solutions of the  $n$ 's with  $G$  from the rate equations.

We, then, may write

$$g(G) = \left\{ (G + G_o)^{1/2} - G_o^{1/2} \right\} / \left\{ (G + G_o)^{1/2} + G_o^{1/2} \right\} . \quad (12-16)$$

Now we determine  $N_D$  and  $N_A$  by choosing  $D_i$ ,  $A_i$ , and  $G_o$  such that the values of  $N_D$  and  $N_A$  become constants for all excitations.

Note that if we impose the conditions

$$\sum D_i = 1 = \sum A_i$$

on  $D_i$  and  $A_i$ , then this random variable method is equivalent to the limiting method.

In the present method, the conditions of Eq. 12-6a become

$$\begin{aligned} (A_o, D_o) &= (1 - N_D/N_A, 0) \text{ for p-type} \\ (A_o, D_o) &= (0, 1 - N_A/N_D) \text{ for n-type} \end{aligned} \quad (12-6b)$$

In other words, we plot the final  $x$  and  $y$  on the  $x$ - $y$  plane and find easily  $A_o$  and  $D_o$ . From these, we get  $N_D/N_A$ . One can check the results from Equations 12-12 and 12-13 with those from Eq. 12-6b.

The test of the present scheme, using the same optical data which were used in the limiting method, has been carried out<sup>83</sup>, and the results from both methods are in excellent agreement with each other

## 12.4 Life Times and Mobilities of Electrons and Holes

The life times and mobilities of electrons and holes also can be deduced from the optical data. Considering the rate equations for  $n$  and  $p$ , and taking the steady state solutions, one may write  $n$  and  $p$  at low excitation regime as

$$n = \tau_e G$$

$$p = \tau_h G$$

where  $\tau_e$  and  $\tau_h$  are the total decay times of electrons and holes respectively. We assume that the generating rates of electrons and holes are equal in this regime. Then, taking the limiting values of the expressions for  $n$  and  $p$  in Equations 12-8 and 12-9, one obtains

$$\lim_{G \rightarrow 0} F_3/F_4 = \tau_h/\tau_e \approx (\mu_h/\mu_e)/y \quad , \quad (12-17)$$

where  $\mu_e$  and  $\mu_h$  are the mobilities of electrons and holes respectively.

To get the above, we approximated the ratio of the effective masses of electrons and holes by  $y = E_D/E_A = m_c^*/m_h^*$  appropriate for a direct band gap material. Thus, the ratios of life times and mobilities of carriers can be deduced from the values of excitation dependent  $I$ 's and  $y$ , without any other parameter. Furthermore, by measuring the absolute of  $G$ , one can get the values of the life times and mobilities of carriers.

Note that, in practice, it is perhaps better to use the limiting values of

$$\lim_{G \rightarrow 0} \partial F_3 / \partial F_4$$

instead of Eq 12-17, since near zero excitation level, the numbers of thermally excited carriers may be appreciable and may yield different values in the two cases.

## 12.5 Determination of Effect Temperatures of Electrons and Holes

When an optical excitation is introduced in a semi-conductor, the distribution functions of electrons and holes are not easily determined. However, one may argue that the systems of electron, hole, and lattice are in separate equilibrium with different temperatures. In other words, one may use the usual

distribution functional forms for carriers by introducing the effective temperatures ( $T_e$ ,  $T_h$ ) and quasi-Fermi energies ( $E_F^e$ ,  $E_F^h$ ) of electron and hole, respectively. Then we may write  $n$ ,  $p$ ,  $n_D$ , and  $n_A$  as

$$n = \int dE \rho_C(E) \bar{F}_C \left( \frac{E - E_F^e}{T_e} \right) , \quad (12-18)$$

$$n_D = \int dE \rho_D(E) \bar{F}_D \left( \frac{E - E_F^e}{T_e} \right) , \quad (12-19)$$

$$p = \int dE \rho_V(E) \bar{F}_V \left( \frac{E - E_F^h}{T_h} \right) , \quad (12-20)$$

$$n_A = \int dE \rho_A(E) \bar{F}_A \left( \frac{E - E_F^h}{T_h} \right) , \quad (12-21)$$

where the  $\rho$ 's and the  $\bar{F}$ 's are the densities of states and distribution functions corresponding to energy bands and impurity levels. Setting the expressions for  $n$ ,  $p$ ,  $n_D$  and  $n_A$  from Equations 12-8 and 12-9 equal to those of Equations 12-18 to 12-21, one can easily obtain  $T_e$ ,  $T_h$ ,  $E_F^e$ , and  $E_F^h$  as functions of the optical excitation level.

Assuming parabolic conduction and valence bands and using the optical data from Ref. 15, the numerical calculations of  $T_e$ ,  $T_h$ ,  $E_F^e$ , and  $E_F^h$  have been carried out and given in Fig.12-1. For completeness, in Fig.12-2 the behaviours of  $n_D$  and  $n_A$  with the excitation level are given. One of the interesting results is that the effective temperature of the hole turns out to be slightly higher than that of the electron. This is attributed to the difference in the characteristic scattering times of electrons and holes.

## 12.6 Remarks

The optical scheme developed yields results in excellent agreement with theoretical predictions. One can easily extend this scheme to a semiconductor with radiative deep centers with appropriate  $f$ 's and  $m$ , provided that the integrated emission intensities corresponding to the states can be written in the forms of Equations 12-2 to 12-4, or in such forms that one can handle the  $n$ 's properly.

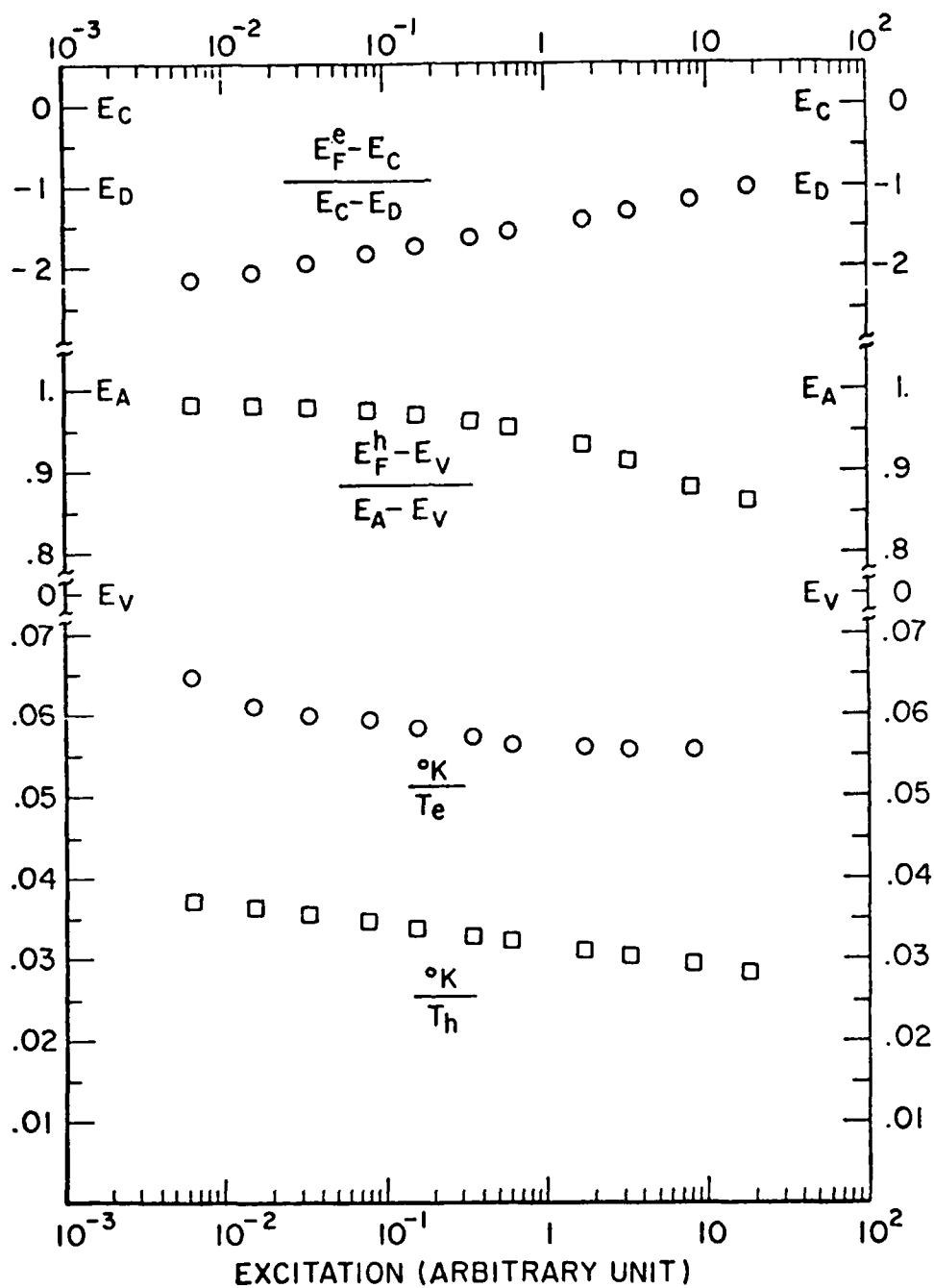


Fig. 12-1. Effective temperatures and quasi-Fermi energies for electrons and holes in GaAs as functions of excitation intensity.

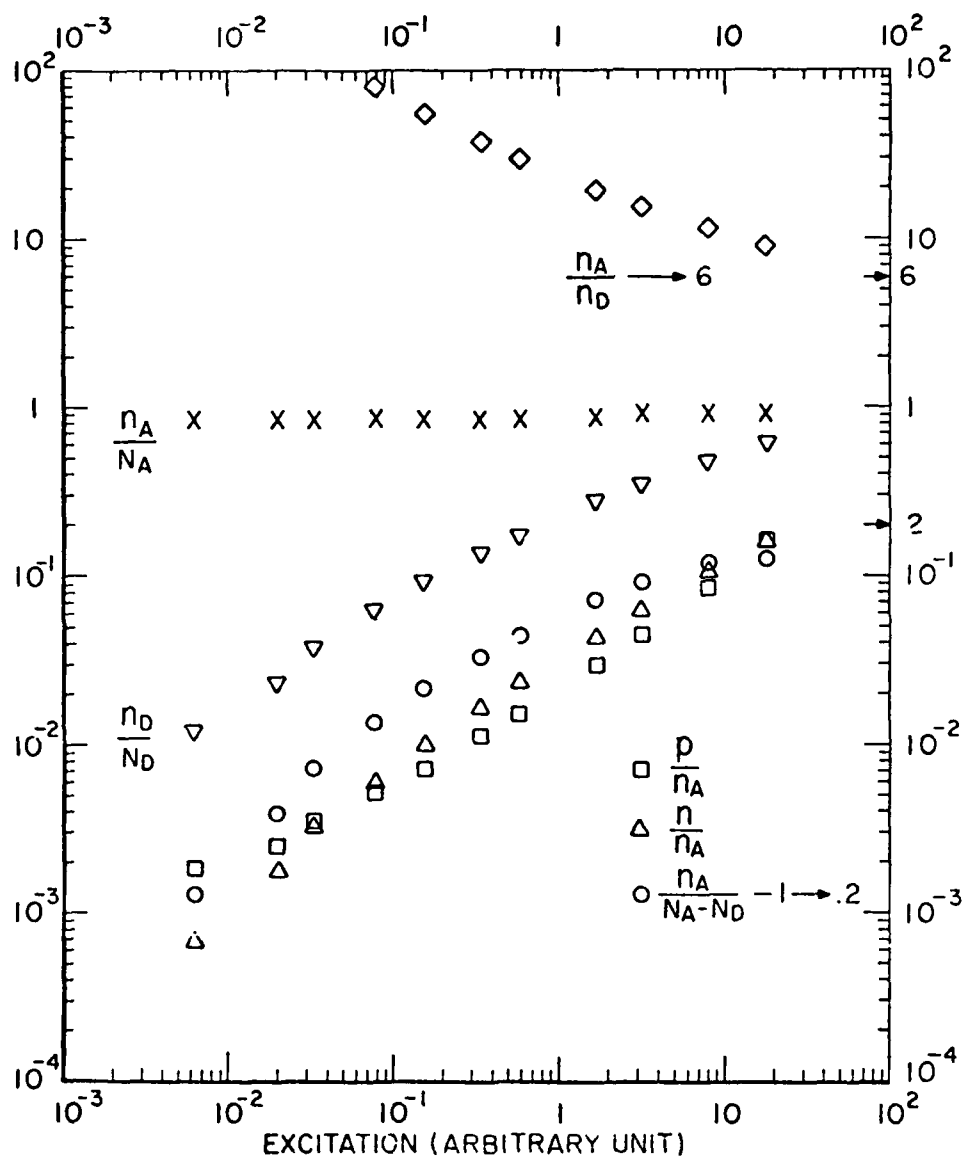


Fig. 12-2. Neutral donor and acceptor concentrations in GaAs as functions of excitation intensity.

Conversely, obtaining  $N_D$  and  $N_A$  by other means, say, electrical methods, one can get the matrix element involved.

For comparison, the values of  $N_D$  and  $N_A$  obtained via this optical scheme in GaAs are in excellent agreement with those obtained via resistivity and Hall effect measurements in the low concentration regime<sup>84</sup>. In the high concentration regime, we expect that the impurity correlation effect plays an important role, in particular, for the calculation of  $f_{DA}$ , which we neglected here. Perhaps the former is a complement to the latter.

It is desirable to explore further the various cases via the optical method.

### 13.0 ENERGIES OF LINES DUE TO DONOR-ACCEPTOR TYPE COMPLEXES IN GaAs

Defects and impurity complexes in a semiconductor, such as, GaAs, play major roles in its electrical properties. To understand these, studies of photoluminescence in GaAs at low temperature have been carried out in various laboratories. The photoluminescence lines below the band gap energy have been understood in terms of optical transitions associated with the exciton related complexes<sup>85-87</sup>.

However, several lines have been observed which evidently are not associated with exciton related complexes in GaAs<sup>88,89</sup>. The actual values of energies observed are given in the comment column of the Tables 13-1 and 13-2.

The common feature of the observed lines C, D, E, and F is no splitting in a strain field. This suggests that the complexes involved are not associated with the usual shallow hole, since the valence band splits under stress. In other words, the complexes must be associated with a deep hole. On the other hand, the magnetic field splittings suggest that they result from transitions between  $J = 3/2$  and  $J = 1/2$  states.

The models of complexes which yield such states can be constructed without difficulty. They may be complexes of

- (a) double donor - single acceptor,
- (b) double acceptor - single donor,
- (c) exciton bound to triplet donor,
- (d) exciton bound to triplet acceptor,
- (e) single donor between two single acceptors,
- (f) single acceptor between two single donors,
- (g) double donor between two single acceptors,
- (h) double acceptor between two single donors, and others.

Table 13-1. Energies of lines calculated using a model of the double acceptor-single donor type complex. The weight is calculated by the number of equivalent sites, N, times the overlapping integral of the wave functions of the components involved, which decays with the distance, R, between them, and it is in arbitrary units.

Same Atomic Sites

N (weight)	$R \times 10^{-8}$ cm	Energy (eV)	Comment
96 (0.46)	22.19	1.51597	
96 (0.45)	22.89	1.51437	E (1.51454)
120 (0.53)	24.24	1.51157	C (1.51165)
120 (0.50)	26.13	1.50813	A (1.50832)
120 (0.49)	26.73	1.50714	
96 (0.37)	27.32	1.50621	
108 (0.43)	27.89	1.50424	

Different Atomic Sites

60 (0.29)	22.32	1.51565	
72 (0.32)	24.36	1.51133	C (1.51165)
72 (0.28)	28.00	1.50518	
84 (0.32)	28.84	1.50400	
72 (0.26)	30.18	1.50221	



Table 13-2. Energies of lines calculated using a model of the double donor-single acceptor type complex. The weight is calculated by the number of equivalent sites, N, times the overlapping integral of the wave functions of the components involved, which decays with the distance, R, between them, and it is in arbitrary units.

Same Atomic Sites

N (weight)	$R \times 10^{-8}$ cm	Energy (eV)	Comment
192 (0.62)	34.04	1.51540	
120 (0.38)	34.51	1.51492	E (1.51454)
108 (0.33)	35.86	1.51366	F (1.51385)
120 (0.36)	36.30	1.51332	D (1.51346)
144 (0.42)	36.74	1.51290	
144 (0.42)	37.17	1.51254	
144 (0.41)	38.01	1.51184	
144 (0.40)	38.43	1.51152	C (1.51165)
240 (0.65)	39.24	1.51089	
240 (0.62)	40.44	1.51003	B (1.51010)
240 (0.58)	42.72	1.50850	A (1.50832)
216 (0.51)	43.10	1.50827	
192 (0.43)	44.90	1.50719	
240 (0.52)	45.95	1.50661	
240 (0.46)	49.29	1.50491	

Different Atomic Sites

60 (0.19)	33.90	1.51552	
60 (0.18)	36.16	1.51339	F (1.51385)
84 (0.24)	38.09	1.51189	C (1.51165)
72 (0.19)	39.92	1.51040	
72 (0.19)	40.32	1.51011	B (1.51010)
72 (0.18)	42.24	1.50881	A (1.50832)
96 (0.22)	43.90	1.50778	
72 (0.16)	44.44	1.50746	
72 (0.15)	46.53	1.50638	
96 (0.19)	48.37	1.50535	
84 (0.16)	49.98	1.50374	
120 (0.21)	52.31	1.50356	

In this report, we give a plausible calculation for the types (a) and (b). The exact calculation of the energies of the various models is extremely difficult, and it is beyond the scope of this report.

We start with a simple minded picture of spectrum for complexes. The energy of a photon resulting from models (a) and (b) can be written as

$$E = E_g - a_A E_A - a_D E_D + e^2/\epsilon R, \quad (13-1)$$

where  $E_g$ ,  $E_A$ , and  $E_D$  are the band gap, acceptor, and donor binding energies,  $\epsilon$  the static dielectric constant,  $R$  the distance between components involved, and  $a_A$  and  $a_D$  are parameters depending upon the specific model of the complex. For type (a), assuming a double donor having a helium configuration, we get

$$a_D = 1.8 \quad \text{and} \quad a_A = 1,$$

respectively. Similarly, for type (b), we get

$$a_D = 1 \quad \text{and} \quad a_A = 1.8.$$

We have calculated the energies for the various distances between the same and different atomic sites of the zinc-blende structure appropriate for GaAs.

The parameters used are

$$E_A = 0.0277 \text{ eV},$$

$$E_D = 0.0057 \text{ eV},$$

$$E_g = 1.5195 \text{ eV},$$

$$\epsilon = 12.5$$

and the lattice constant  $a = 5.635 \times 10^{-8} \text{ cm}$ . In Tables 13-1 and 13-2, we have given the energies for the distances where many equivalent sites can be found.

The weight is calculated by the number of equivalent sites times the overlapping integral of the wave functions of the components involved, which decreases with the distance,  $R$ , between them.

For comparison, the observed energies of the lines are given in the comment column. Even though there are several lines whose energies are close to the calculated energy values, we are not able to make a definite conclusion about the transitions involved, at present. It is noted that the R involved is of the order of the size of an acceptor. Perhaps, this may be a reflection of the fact that the models considered are of the donor-acceptor types.

To understand these effects, it is desirable to carry out further study along these lines.

# REFERENCES

1. C.R. Cronin and R.W. Haisty, J. Electrochem. Soc. 111, 874 (1964).
2. N. Yokoyama, A. Shibatomi, S. Ohkawa, M. Fukuta, and H. Ishikawa, in Proceedings of the Conference on GaAs and Related Compounds (St. Louis), 1976, ed. by Lester F. Eastman (Inst. of Physics, London, 1977) p. 201.
3. J. Barrera, in Proceedings of the Fifth Biennial Cornell Electrical Engineering Conference (Cornell U.P., Ithaca, 1975) p. 135.
4. D.C. Look, J. Phys. Chem. Solids 36, 1311 (1975).
5. D.C. Look, J. Electron. Mat. 7, 147 (1978).
6. D.C. Look, Phys. Rev. B16, 5460 (1977).
7. D.C. Look, J. Appl. Phys. 48, 5141 (1977).
8. P.W. Yu, Sol. State Commun. 32, 1111 (1979)
9. P.W. Yu and Y.S. Park, J. Appl. Phys. 50, 1079 (1979).
10. M.M. Kreitman, S.P. Faile, C.W. Litton, and D.C. Reynolds, in Optical Properties of Highly Transparent Solids, ed. by S.S. Mitra and B. Bendow (Plenum, New York, 1976) p. 179.
11. M.M. Kreitman, D.H. Must, K.K. Bajaj, and C.W. Litton, Bull. Amer. Phys. Soc. 22, 1242 (1977).
12. M.M. Kreitman, J.W. Farmer, K.K. Bajaj, and C.W. Litton, Sol. State Commun. 32, 553 (1979).
13. D.C. Look, Sol. State Commun. 24, 825 (1977).
14. J.W. Farmer and D.C. Look, J. Appl. Phys. 50, 2970 (1979).
15. S.B. Nam, D.W. Langer, D.L. Kingston, and M.J. Luciano, Appl. Phys. Lett. 31, 652 (1977).
16. P.W. Yu, Sol. State Commun. 27, 1421 (1978).
17. J.W. Farmer and D.C. Look, Phys. Rev. B21, 3389 (1980).
18. D.V. Lang and L.C. Kimerling, in Lattice Defects in Semiconductors, 1974 (Institute of Physics, London, 1975) p.581.
19. D.J. Ashen, P.J. Dean, D.T.J. Hurle, J.B. Mullin, and A.M. White, J. Phys. Chem. Sol. 36, 1041 (1975).
20. P.W. Yu, J. Appl. Phys. 48, 5043 (1977).

21. W.H. Koschel, S.G. Bishop, and B.D. McCombe, in Proceedings of the Thirteenth International Conference on the Physics of Semiconductors, Rome (1976), ed. by F.G. Fumi (Tipografia-Marves, Rome, 1977) p. 1065
22. R.D. Fairman, M. Omori, and F.B. Fank, Ref. 2, p 45.
23. D.C. Look, Phys. Rev. B20, 4160 (1979).
24. P.W. Yu, Sol. State Commun. 34, 183 (1980).
25. P.W. Yu, in Semi-insulating III-V Materials, ed. by G.J. Rees (Shiva, Kent, England, 1980) p. 167.
26. D.C. Look, Sol. State Commun. 33, 237 (1980).
27. G. W. Iseler, in GaAs and Related Compounds, 1978, ed. by C.M. Wolfe (Inst. of Physics, London, 1979) p.144.
28. P. Blood and J. W. Orton, Rep. Prog. Phys. 41, 157 (1978).
29. D.C. Look and J.W. Farmer, J. Phys. E: Sci. Instr. (to be published, 1981).
30. D.C. Look, J.W. Farmer, and R.N. Ely, Rev. Sci. Instr. 51, 968 (1980).
31. D.C. Look, Ref. 25, p. 183.
32. See, e.g., R.N. Thomas, H.M. Hobgood, G.W. Eldridge, D.L. Barrett, and T.T. Braggins, Sol. State Electronics (to be published, 1980).
33. A. M. Huber, N.T. Linh, M. Valladon, J.L. Debrun, G.M. Martin, A. Mitonneau, and A. Mircea, J. Appl. Phys. 50, 4022 (1979).
34. D.C. Look, J. Appl. Phys. 49, 3543 (1980).
35. See, e.g., E. H. Putley, The Hall Effect and Semiconductor Physics (Dover, New York, 1968) p. 124.
36. R. Calawa, unpublished (private communication from C.W. Litton).
37. D.C. Look, Sol. State Commun. 33, 237 (1980).
38. O. Mizuno and H. Watanabe, Electron. Lett. 11, 118 (1975).
39. G.K. Ippolitova, E.M. Omelyanovski, N.M. Pavlov, A. Ya Nashelski, and S.V. Yakobson, Sov. Phys. Semicond. 11, 773 (1977).
40. W. H. Koschel, U. Kaufman, and S. G. Bishop, Sol. State Commun. 21, 1069 (1977).
41. B. Turk and G.A. Adegboyega, J. Phys. D12, 1895 (1979).
42. H.J. Stocker, and S. M. Schmidt, J. Appl. Phys. 47, 2450 (1976).
43. M. Jeong, J. Shirafuji, and Y. Inuishi, Jpn. J. Appl. Phys. 12, 1096 (1973).

44. L.L. Chang, L. Esaki, and R. Tsui, Appl. Phys. Lett. 19, 143 (1971).
45. W.Y. Lum, H.H. Wieder, W.H. Koschel, S.G. Bishop, and B.D. McCombe, Appl. Phys. Lett. 30, 1 (1977).
46. A.Y. Cho and I. Hayashi, Solid State Electron. 14, 125 (1971).
47. M. Ilegems, R. Dingle, and L.W. Rupp, Jr., J. Appl. Phys. 46, 3059 (1975).
48. J. Hallais, A. Mircea-Roussel, J.P. Farges, and G. Poiblend, Proceedings of the Sixth International Symposium on Gallium Arsenide and Related Compounds, Inst. Phys. Conf. Ser. 336 (Institute of Physics, London, 1976), p. 220.
49. W. Shairer and M. Schmidt, Phys. Rev. B10, 2501 (1974).
50. T.N. Morgan, Phys. Rev. 139, A343 (1965).
51. D. Redfield, J.P. Wittke, and J.I. Pankove, Phys. Rev. B2, 1830 (1970).
52. P.W. Yu, J. Appl. Phys. 50, 7165 (1979).
53. W.H. Koschel, S.G. Bishop, and B.D. McCombe, Solid State Commun. 19, 521 (1976).
54. E.C. Lightowers and C.M. Petchina, J. Phys. C11, L405 (1978).
55. T. Instone and L. Eaves, J. Phys. C11, L771 (1978).
56. K. Kocot and G.L. Pearson, Solid State Commun. 25, 113 (1978).
57. A.M. White, Solid State Commun. 32, 205 (1979).
58. W.J. Turner, G.D. Pettit, and N.G. Ainslie, J. Appl Phys. 34, 3274 (1963).
59. B. Deveaud and P.N. Favennec, Solid State Commun. 24, 473 (1977).
60. D.V. Lang and R.A. Logan, J. Elect. Mat. 4, 1053 (1975).
61. J.B. Mullin, A. Royles, B.W. Stranghan, P.J. Tufon, and E.W. Williams, J. Cryst. Growth 13/14, 640 (1972).
62. O. Roder, U. Heim and M.H. Pilkuhn, J. Phys. Chem. Solids 31, 2625 (1970).
63. S. Fung, R.J. Nicholas, and R.A. Stradling, J. Phys. C: Solid State Phys. 12, 5145 (1979).
64. D.V. Lang, R.A. Logan, and L.C. Kimerling, Phys. Rev. B15 4874 (1977).
65. D. Pons, A. Mircea, and J. Bourgoin, J. Appl. Phys. 51, 4150 (1980).
66. E.T. Rodine, J.W. Farmer, and D.W. Langer, J. Appl. Phys. 50, 5527 (1979).
67. J.W. Farmer and D.R. Locker (submitted for publication).
68. H.J. Queisser and D.E. Theodorou, Phys. Rev. Lett. 43, 401 (1979).
69. M.M. Kreitman, K. . Bajaj, and C.W. Litton, Bull. Am. Phys. Soc. 22, 1039 (1977).

70. O.G. Lorimor and W.G. Spitzer, J. Appl. Phys. 37, 3687 (1966).
71. W.G. Spitzer and W. Allred, J. Appl. Phys. 39, 4999 (1968).
72. P.C. Leung, J. Fredrickson, and W.G. Spitzer, J. Appl. Phys. 45, 1009 (1974).
73. M.M. Kreitman, K.K. Bajaj, and C.W. Litton, Bull. Am. Phys. Soc. 23, 225 (1978).
74. R.C. Newman, F. Thompson, M. Hyliands, and R.F. Peart, Solid State Commun. 10, 505 (1972).
75. M.M. Kreitman, J.W. Farmer, K.K. Bajaj, and C.W. Litton, Bull. Am. Phys. Soc. 24, 402 (1979).
76. M.M. Kreitman, J.W. Farmer, W.M. Theis, C.W. Litton, and K.K. Bajaj, Bull. Am. Phys. Soc. 25, 202 (1980).
77. D.L. Rode, Semiconductors and Semimetals, ed. by R.K. Willardson and A. C. Beer (Academic Press, New York, 1975) Vol. 10, p1.
78. C.M. Wolfe and G.E. Stillman, *ibid* 10, p.175.
79. T. Kamiya and E. Wagner, J. Appl. Phys. 48, 1428 (1977).
80. C. Kittel, Quantum Theory of Solids (John Wiley and Sons, Inc., New York, 1963) p.283.
81. J. Bardeen, F.J. Blatt, and L.H. Hall, Photoconductivity Conference ed. by R. G. Breckenridge, B.R. Russell, and E. E. Hahn (John Wiley and Sons, Inc., New York, 1956) p.146.
82. L.I. Schiff, Quantum Mechanics (McGraw Hill, New York, 1955, 3rd Ed.) Chapt. 10.
83. D.G. Shankland and S.B. Nam, Bull. Am. Phys. Soc. 23, 971 (1978).
84. M. Ozeki, J. Komeno, A. Shibatomi, and S. Ohkawa, Inst. Phys. Conf. Ser. No. 45, 220 (1979).
85. D.D. Sell, S.E. Stokowski, R. Dingle, and J.V. DiLorenzo, Phys. Rev. B7, 4568 (1973).
86. A.M. White, P. J. Dean, and B. Day, J. Phys. C7, 1400 (1974).
87. S.B. Nam, D.C. Reynolds, C.W. Litton, R.J. Almassy, T.C. Collins, and C.M. Wolfe, Phys. Rev. B13, 761 (1976).
88. D.C. Reynolds, R.J. Almassy, C.W. Litton, S.B. Nam, and G.L. McCoy, J. Appl. Phys. 49, 5336 (1978).
89. D.C. Reynolds, C.W. Litton, R.J. Almassy, G.L. McCoy, and S.B. Nam, J. Appl. Phys. 51, 4842 (1980).

# PUBLICATIONS

1. D.C. Look, "The Electrical Characterization of Semi-Insulating GaAs: a Correlation With Mass Spectrographic Analysis", J. Appl. Phys. 48, 5141 (1977).
2. D.C. Look, "On the Interpretation of Photoconductivity and Photo-Hall Spectra in Semi-Insulating GaAs:Cr", Sol. State Comm. 24, 825 (1977).
3. D.C. Look, "Impurity Photomagnetoelectric Effect: Application to Semi-Insulating GaAs", Phys. Rev. B 16, 5460 (1977).
4. Phil Won Yu and Y.S. Park, "Photoluminescence from Mg-implanted GaAs", Appl. Phys. Lett. 30, 14 (1977).
5. Phil Won Yu, J.T. Grant, Y.S. Park and T.W. Haas, "Zn-ion-implantation Profiles in CuInSe<sub>2</sub> by Auger Electron Spectroscopy", J. Appl. Phys. 48, 67 (1977).
6. Phil Won Yu and Y.S. Park, "Temperature Dependence of Photoluminescence from Mg-implanted GaAs", J. Appl. Phys. 48, 2434 (1977).
7. Phil Won Yu, "Excitation Dependent Emissions in Mg, Be, Cd and Zn Implanted GaAs", J. Appl. Phys. 48, 5043 (1977).
8. D.C. Reynolds, R.J. Almassy, C.W. Litton, S.B. Nam, and G.L. McCoy, "Sharp-Line Transitions Due to Donor-Acceptor Recombinations in High Quality GaAs Epilayers", in GaAs and Related Compounds (British Inst. of Physics, London, 1977) p.219.
9. S.B. Nam, D.W. Langer, D.L. Kingston, and M.J. Luciano, "Determination of Concentrations of Donors and Acceptors in GaAs by an Optical Method", Appl. Phys. Lett. 31, 652 (1977).
10. D.C. Look, "On the Characterization of Semi-Insulating GaAs by Hall, Photo-Hall, Photoconductivity and Photomagnetoelectric Measurements", J. Electronic Mat. 7, 147 (1978).
11. R. J. Almassy, D.C. Reynolds, C.W. Litton, K.K. Bajaj, and D.C. Look, "Sharp Line Emission Spectra from GaAs FET-Like Structures", J. Electronic Mat. 7, 263 (1978).
12. D.C. Look, "Infrared Spectral Detectivity of Cr-doped GaAs", J. Appl. Phys. 49, 3543 (1978).
13. Phil Won Yu, "Comparison of Compensation Ratios Determined by Photoluminescence and Electrical Methods in Epitaxial GaAs", Solid State Commun. 27, 1421 (1978).
14. D.C. Reynolds, R.J. Almassy, C.W. Litton, S.B. Nam, and G.L. McCoy, "Donor-Acceptor-type Complex in GaAs", J. Appl. Phys. 49, 5336 (1978).
15. J.W. Farmer and D.C. Look, "Type Conversion in Electron-Irradiated GaAs", J. Appl. Phys. 50, 2970 (1979).



16. D.C. Look, "Model for  $\text{Fe}^{2+}$  Intracenter-Induced Photoconductivity in  $\text{InP:Fe}$ ", Phys. Rev. B 20, 4160 (1979).
17. Phil Won Yu and Y.S. Park, "Photoluminescence in Mn-implanted GaAs-An Explanation on the 1.40-eV Emission", J. Appl. Phys. 50, 1079 (1979).
18. Y.K. Yeo, Y.S. Park and Phil Won Yu, "Electrical Measurements and Optical Activation Studies in Mg-implanted GaAs", J. Appl. Phys. 50, 3274 (1979).
19. Phil Won Yu, "Deep Emission Centers in Ge-implanted GaAs", J. Appl. Phys. 50, 7165 (1979).
20. Phil Won Yu, "Effect of Oxygen in Photoluminescence from Chromium-doped Semi-insulating GaAs", Solid State Commun. 32, 1111 (1979).
21. J.W. Farmer and D.C. Look, "Type Conversion in Electron-Irradiated GaAs", J. Appl. Phys. 50, 2970 (1979).
22. M.M. Kreitman, J.W. Farmer, K.K. Bajaj and C.W. Litton, "Observation of Localized Vibrational Mode Adsorption of Carbon-Implanted GaAs and Effects of Annealing Temperature," Solid St. Comm. 32, 553 (1979).
23. E.T. Rodine, J.W. Farmer and D.W. Langer, "Defect Studies in Multilayer Epitaxial GaAs by Transient Capacitance," J. Appl. Phys. 50, 5526 (1979).
24. J.W. Farmer and D.C. Look, "Electron Irradiation Defects in n-type GaAs", Phys. Rev. B21, 3389 (1980).
25. D.C. Look, "Resonance Photoconductivity in Fe-doped InP", Solid State Commun. 33, 237 (1980).
26. D.C. Look, J.W. Farmer, and R.N. Ely, "Automation of a Popular Monochromator", Rev. Sci. Instr. 51, 968 (1980).
27. Phil Won Yu, "A Model for the 1.10-eV Emission Band in InP", Solid State Commun. 34, 183 (1980).
28. D.C. Look, "True Mobilities in O- and Cr-doped GaAs", in Semi-insulating III-V Materials, ed. by G.J. Rees (Shiva, Kent, England, 1980) p.183.
29. Phil Won Yu, "Photoluminescence and Photoconductivity Study of the 1.10-eV Energy Level in Fe-doped InP", in Semi-insulating III-V Materials, ed. by G.J. Rees (Shiva, Kent, England, 1980) p.167.
30. D.C. Reynolds, C.W. Litton, R.J. Almassy, G.L. McCoy, and S.B. Nam, "Complexes Due to Donor-Acceptor Type Transitions in GaAs", J. Appl. Phys. 51, 4842 (1980).
31. D.C. Look and J.W. Farmer, "Automated, High-Resistivity Hall-Effect and Photoelectronic Apparatus", J. Phys. E: Sci. Instr. (to be published, 1981).
32. Phil Won Yu, "Iron in Heat-treated GaAs", J. Appl. Phys. (to be published, 1981).

**DATE**  
**ILME**